Measurement of QCD Jet Broadening in $p\bar{p}$ Collisions at $\sqrt{s} = 1.8$ TeV

by Brenna Lynn Flaugher

A dissertation submitted to the

Graduate School— New Brunswick

Rutgers, The State University of New Jersey

in partial fulfillment of the requirements

for the degree of

Doctor of Philosophy

Graduate Program in Physics

Written under the direction of

Thomas J. Devlin

and approved by

[redacted]

New Brunswick, New Jersey

October, 1989

ABSTRACT OF THE DISSERTATION

Measurement of QCD Jet Broadening in $p\bar{p}$ Collisions at $\sqrt{s} = 1.8$ TeV

by Brenna Lynn Flaugher, Ph.D.

Dissertation Director: Thomas J. Devlin

A measurement of the QCD Jet Broadening parameter, $< Q_t >$, is described for high E_t jet data in the central CDF calorimeter. Most analyses of $p\bar{p}$ jet data compare to QCD predictions by identifying clusters of energy in a detector. As an alternate approach, the method employed here involves the use of a global event parameter which is free from the ambiguities associated with the definition and separation of individual clusters. The parameter, Q_t, is defined as the scalar sum of the transverse momentum perpendicular to the transverse thrust axis. At the parton level, Q_t is zero for the $2 \Rightarrow 2$ QCD process and thus, to first order, comes from the $2 \Rightarrow 3$ process. Q_t is defined such that it cancels the divergences in the $2 \Rightarrow 3$ matrix elements, and thus it can be evaluated without imposing separation and minimum P_t cuts on the $2 \Rightarrow 3$ partons. QCD predictions made for $< Q_t >$ are the result of a $2 \Rightarrow 3$ calculation divided by a $2 \Rightarrow 2$ calculation and show some dependence of the strong coupling constant α_s. Comparisons are made to first-order QCD parton level calculations as well as to fully evolved and hadronized leading log predictions. The data is well described by the QCD predictions.

Acknowledgements

First, I would like to acknowledge my colleagues in CDF who are listed in Fig. D.1 and Fig. D.2 in Appendix D. This work was supported in part by Rutgers University and The National Science Foundation through Grant NSP-PHY-85-14193.

In particular I would like to thank: my advisor, Tom Devlin, for giving me the opportunity to work on CDF, and without whose support and encouragement this thesis would not have been possible; G.P Yeh whose enthusiasm for CDF convinced me to join this experiment; John Huth for suggesting the topic of this analysis and helping push it to completion; Steve Behrends for innumerable discussions, guidance in the analysis and infinite help in preparing this document; Michelangelo Mangano for patient and clear explanations of the theoretical issues; and the other members of the QCD-Jet group who have contributed in different ways to this analysis.

Next, I wish to acknowledge the contributions of the Level 3 group, in particular J.T. Carroll whose knowledge and foresight made the Level 3 trigger a reality; and Ping Hu and Priscilla Auchincloss for taking over the day-to-day responsibilities for the Level 3 trigger which allowed me to concentrate on this analysis.

Last, but not least, I would like to thank my husband, Tom Diehl, for his constant encouragement and excitement; and my parents for their support and encouragement throughout the years.

Table of Contents

List of Tables

List of Figures

Chapter 1
Introduction

With the increasing ability of particle accelerators to reach higher energy and higher luminosity, experimentalists have been given the opportunity to explore new kinematic regions of the strong force gauge theory, Quantum Chromodynamics (QCD). Historically, the highest energy accelerators directed a beam of charged particles onto a fixed target. In the fixed target arrangement, $E_{cm} \approx \sqrt{2E_B M}$, where E_{cm} is the energy of the collision in the center-of-mass frame, E_B is the energy of the beam, and M is the mass of the target. To reach higher energies, collider technology was viewed as more efficient and cost effective since $E_{cm} = 2E_B$. During the 1970's, electron-positron collider experiments began to produce measurements which tested QCD predictions in the E_{cm} region of $\approx$ 1-20 GeV. Improvements over the years have been made such that e^+e^- collider experiments have now gathered a significant amount of data at center-of-mass energies up to roughly 50 GeV[1, 2] .

For a fixed-radius circular accelerator, the energy lost to synchrotron radiation is proportional to $(\frac{E_B}{M})^4$. Protons and antiprotons can be accelerated to higher energies on a circular path than electrons and positrons because the radiated energy is much smaller. As a result, protons and antiprotons have been used to produce the highest energy particle collisions. In 1971 the Intersecting Storage Rings (ISR) at CERN produced pp collisions (and later $p\bar{p}$) at an E_{cm} of 63 GeV. By 1981 the CERN Super Proton Synchrotron (SPS) had achieved $p\bar{p}$ collisions at E_{cm} of 540 GeV. In 1985, a short engineering run demonstrated that the Fermilab Tevatron could produce $p\bar{p}$ collisions at the highest energy yet available in an accelerator, E_{cm} = 1.8 TeV. In January 1987, the Collider Detector at Fermilab (CDF) began an extended run and recorded what would turn out to be roughly 25 nb^{-1} of data at $E_{cm} = 1.8$ TeV. Analysis of this data is the subject of this thesis.

The dominant process in $p\bar{p}$ interactions is a soft scattering in which the proton and antiproton collide with large impact parameter, and do not significantly interact. By contrast, a hard scattering is pictured as a collision in which the proton and antiproton come so close together that their constituent quarks (q) and gluons (g) interact. (This type of event is the QCD equivalent of Rutherford scattering.) The experimental signature for hard scattering is the emergence of particles carrying large amounts of energy at wide angles to the incident beam direction. While soft collisions are governed by the dynamics of the hadrons, which are composite structures and are difficult to describe theoretically, the theory of perturbative Quantum Chromodynamics makes predictions for hard scattering processes.

Although partons are involved in the collisions, the particles that reach a detector are primarily hadrons. The process by which a parton is transformed into hadrons is known as fragmentation or hadronization. The principal concept of fragmentation is that the color force of QCD causes colored quarks and gluons to regroup into colorless hadrons by combining with quark-antiquark pairs which are produced from the vacuum by strong force color fields. Most of the momentum of the resulting hadrons is along the direction of the original parton momentum. This cluster of hadrons is referred to as a jet. Jets are identified experimentally by the deposition of a large amount of energy in a localized area of a detector. The existence of QCD-jetlike structures in the CDF data was immediately obvious from event displays. A jet event in the CDF calorimeter is shown in Fig. 1.1. Well-defined clusters of energy are visible, as well as some low energy depositions away from the clusters.

As discussed in the following chapters, 'lowest order' perturbative QCD predictions are based on the idea of two partons in the initial state (before the collision) and two partons in the final state (after the collision). This corresponds to the case where a gluon or quark is exchanged between the incoming partons, and thus the theoretical calculations carry two powers of α_s , the strong coupling constant. The two final state

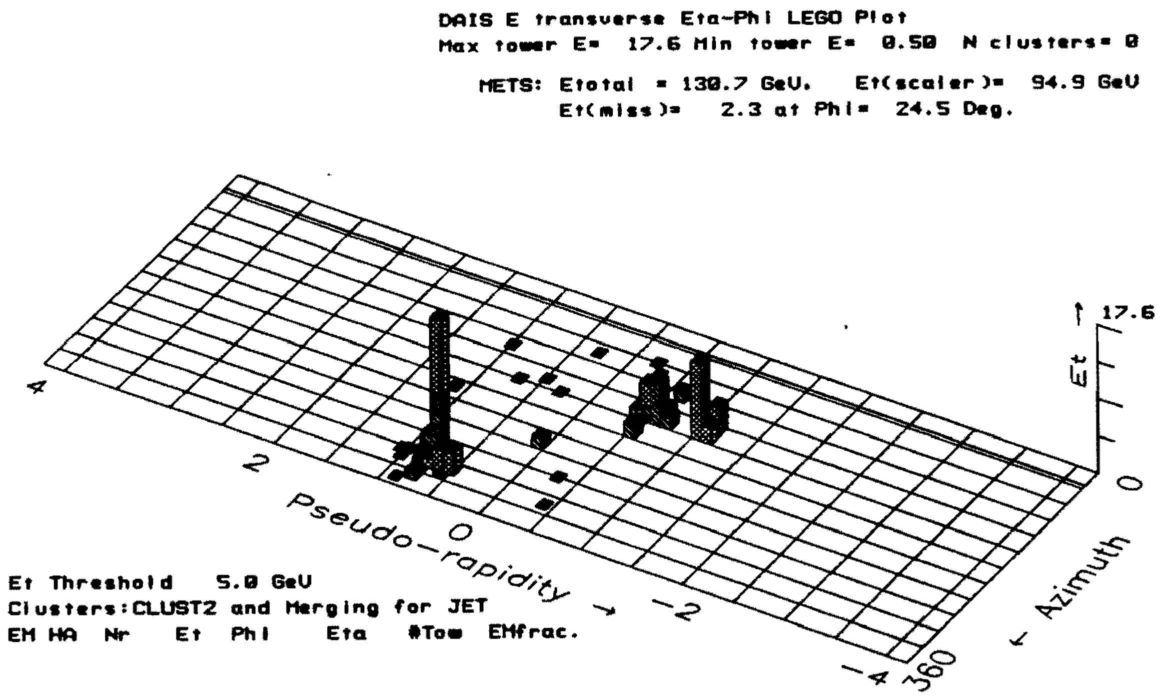

Figure 1.1: A CDF Jet event. The cylindrical calorimeter has been 'unrolled' such that the axes of the grid represent the azimuthal angle around the beamline, and the pseudo-rapidity, defined as $-ln(tan(\theta/2))$, where θ is the polar angle with respect to the beamline. The height of each cell is proportional to its energy.

partons fragment into hadrons and form a 'two-jet' event. QCD predictions which have three orders of α_s represent the case where one of the partons has radiated one gluon (bremsstrahlung). These calculations are termed 'lowest order' in $O(\alpha_s^3)$ and can lead to three separate well-defined clusters. These so-called 'three-jet' events were first observed in e^+e^- annihilation during the late 70's, and provided the first direct evidence for the existence of gluons[3] . Higher order corrections to the both the $2 \Rightarrow 2$ and $2 \Rightarrow 3$ processes include the effects of more elaborate configurations of gluon radiation and are discussed in Chapter 2.

Early jet physics was studied at the ISR, at Fermilab fixed target experiments and at e^+e^- colliders. Compared to the Tevatron energies, these machines operated at low E_{cm} and thus the partons from the collisions had relatively low energy. The fragmentation products from these low energy partons were distributed over a wide angular region with respect to the original parton direction, making the identification and separation of individual clusters (jets) difficult.

As an alternative to a clustering type of analysis, these experiments developed techniques involving global event shape parameters to determine the 'jetiness' of their events and to make comparisons to QCD predictions. The favored parameters for precision tests of QCD were the Energy-Energy Correlation function (EEC) and the Asymmetric Energy-Energy Correlation function (AEEC or EECA). These parameters were determined from the angular distribution of energy in the events. The measurement of an asymmetric component was taken as an indication of $O(\alpha_s^3)$ QCD processes since two-jet events were expected to have only a symmetric component. These quantities have been studied in detail as a method of measuring α_s . (See [4], [5] or [6] for a summary of these techniques and results.) Unfortunately, the contribution of fragmentation to the theoretical prediction is apparently large and the different models result in different determinations of α_s . The problem stems from a fundamental theoretical uncertainty in deciding the relative contributions of gluon radiation and fragmentation to the formation of the jet of particles. Different fragmentation models account for different amounts of the angular distribution of the hadrons associated with the original parton and thus result in different estimations of the calcuable QCD component.

Data from higher energy electron and hadron colliders showed striking evidence of well-defined jetlike clusters, and as a result, the primary approach for comparing the data to theoretical predictions involved a clustering type of analysis instead of an event shape analysis. The clustering philosophy is based on locating clusters of energy in the detector, measuring the energy within the cluster cone, and from this determining the momentum of the original parton. Since the partons produced in these higher energy collisions are more energetic, their fragmentation products are more tightly constrained to the direction of the original parton. This suggests that a direct comparison to perturbative QCD parton level predictions should be possible, without a heavy reliance on the fragmentation model. Recent analysis of CDF data taken during the 1987 run has been based on clustering techniques, and has demonstrated that the inclusive differential jet cross-section[7] and angular distributions of two-jet events[8] are in good agreement with lowest order QCD predictions.

The study of events with more than two partons in the final state provides valuable checks of the higher order ($O(\alpha_s^3)$ and above) QCD predictions. Experimentally, if a clustering type of analysis is used, sensitivity to $O(\alpha_s^3)$ terms is limited to the case in which a radiated gluon can be identified as an independent cluster. This imposes both energy and angular restrictions on the emitted gluon and reduces the sensitivity to low energy wide angle gluon emission[1]. If gluons are radiated at angles less than the cluster radius they will be included with the original parton. If they are radiated at wide angles to the original parton they must be above the cluster energy threshold to be counted as an additional jet. For example, the event shown in Fig. 1.1 could be designated as either a two-jet or three-jet event, depending on the cluster definition parameters. As discussed below, by using a global event parameter instead of imposing cluster selection criteria on the data, this type of ambiguity is avoided. Since clustering analysis is limited to the case where energetic gluons are radiated at wide angles to

[1] Typical clustering algorithms have a cone radius of ≈ 0.7 radians and a minimum cluster energy cut that corresponds to roughly a 20 GeV parton.

the original partons, comparisons to theoretical predictions were also limited to this kinematic region.

Although both e^+e^- and $p\bar{p}$ collider experiments study the formation of jets and make comparisons to QCD predictions, until recently they have been sensitive to different regions of the QCD calculations: $p\bar{p}$ jet analysis, with a clustering approach, is insensitive to low energy wide angle gluon emission but is able to make comparisons to the predictions for hard gluon emission, while e^+e^- jet analysis, with measurements of the overall event shape, is sensitive to low energy gluon emission and fragmentation effects.

A merging of these techniques has recently become possible. Results from the e^+e^- data of the AMY Collaboration[2] at an E_{cm} of 50 - 57 GeV are based on clustering analysis in which the number of two-jet events are compared to the number of three-jet events. By combining results from different e^+e^- experiments which were performed at different E_{cm} they show a decrease in the strong coupling parameter as expected from QCD predictions. This technique is very similar to the the analysis performed by the UA1 collaboration[9] on $p\bar{p}$ data from the SPS collider where the ratio of the number of three-jet events to the number of two jet events was used to measure α_s .

While both e^+e^- and $p\bar{p}$ collider experiments were able to derive results based on clustering analysis, QCD predictions for global event parameters in $p\bar{p}$ data were essentially nonexistent. In 1986, Ellis and Webber introduced a global event parameter called Q_t which they applied to $p\bar{p}$ collisions[10]. Q_t is defined as the scalar sum of the momentum perpendicular to the thrust axis in the plane transverse to the beam. This parameter is similar to the e^+e^- global parameters in that it is sensitive to gluon emission without a requirement of angular and energy restrictions in either the experimental determination or the theoretical calculation. As discussed in Chapter 2, Q_t has the property of canceling the infra-red and collinear divergences in the three jet matrix elements and thus the theoretical evaluation of Q_t can be performed over the full range of three jet configurations, without imposing angular separation or energy cuts on the emitted gluon. In addition, Q_t is, in principal, insensitive to soft hadronization and fragmentation effects. The behavior of Q_t with increasing energy is termed Jet Broadening as an indication of its sensitivity to the increasing multiparton nature of a jet as the energy of the jet increases. As discussed in Chapter 2, the behavior of Q_t over the energy range spanned by the CDF data could be sensitive to the evolution of the strong coupling parameter. Analogous quantities have been measured for E_{cm} ranging from 9.4 to 31.6 Gev in e^+e^- collisions by the Pluto Collaboration[11]. They saw evidence of Jet Broadening which required that radiative corrections be included in the QCD predictions, although fragmentation effects made it impossible to make a precision determination of α_s . Comparison of QCD predictions for Q_t to its measurement in the CDF jet data is discussed in the following chapters, and provides a new test of QCD: high energy collisions with sensitivity to low energy wide angle gluon emission.

This thesis will concentrate on the theoretical calculation of Q_t and on the measurement of Q_t from CDF data. In Chapter 2, the theoretical definitions and calculations of Q_t will be discussed. Chapter 3 describes the elements of the detector and trigger system that are important for this analysis, and Chapter 4 describes the data sample and analysis. A summary and conclusions are presented in Chapter 5.

Chapter 2

Theoretical Calculations

2.1 Quantum-Chromodynamics

Current theoretical interpretation of the strong force describes all hadrons as being made up of combinations of spin 1/2 fermions (quarks) and the spin 1 gauge bosons of QCD (gluons). Quarks are believed to come in six distinct flavors: up, down, strange, charm, bottom and top. Evidence for the top quark has not yet been observed. There are two types of hadrons: baryons, which consist of three so-called 'valence' quarks, and mesons, which consist of a quark-antiquark pair of valence quarks. The properties of the valence quarks determine the normal quantum numbers of hadrons such as charge, hypercharge, isospin and baryon number. Protons and antiprotons are baryons; pions and kaons are mesons. In addition to the valence quarks, a 'sea' or cloud of virtual gluons and quark-antiquark pairs are believed to exist in hadrons.

To explain the strong force, which causes the quarks and gluons to combine and form particles, each quark is given one of three possible QCD charges, or 'colors', which we refer to as red, blue or green, and antiquarks are said to have anti-color, i.e. anti-red, anti-blue or anti-green. Gluons carry two color charges, one color and one anti-color, and color is conserved in interactions between quarks and gluons. For example, a green quark can turn into an blue quark by emitting a green-anti-blue gluon. Only quarks and gluons transmit the strong force, and only colored objects (both quarks and gluons) can emit a gluon. All hadrons consist of colorless combinations of quarks and gluons. The theory of the strong force, which describes the interactions between the colored quarks and gluons, is called Quantum Chromodynamics, (QCD).

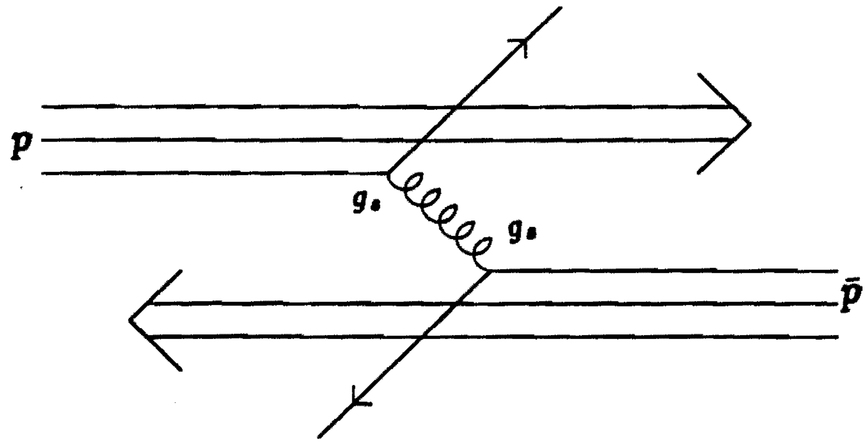

Figure 2.1: Schematic Representation of a $p\bar{p}$ Collision.

The nature of the strong force can be probed through the use of high energy particle collisions. A schematic diagram of a proton-antiproton hard collision is shown in Figure 2.1. As shown, a typical hard scattering involves a parton from each hadron in the collision. The remaining partons continue along the beam direction and eventually fragment into hadrons; if the scattered partons have gained sufficient momentum transverse to the original beam direction, their fragmentation products can be measured in a detector. Quantum Chromodynamics makes predictions for, among other things, the number of partons, angular distributions of partons, and the energy spectrum of partons that are produced in high energy hadron collisions. Comparison of the predictions to experimental data provides a test of the validity of Quantum Chromodynamics.

For strong interactions at Tevatron energies, the coupling parameter between the quarks and gluons is moderately small, about 0.15 as discussed below, and the theoretical calculations are separated into orders of the coupling. The lowest order case, shown in Fig. 2.1, involves two incoming partons which collide and produce two outgoing partons. Each vertex gives one factor of the coupling parameter g_s which is defined such that $\alpha_s = g_s^2/4\pi$. Higher order terms in the perturbative expansion incorporate the effects of allowing one or more of the partons to radiate gluons. The theoretical

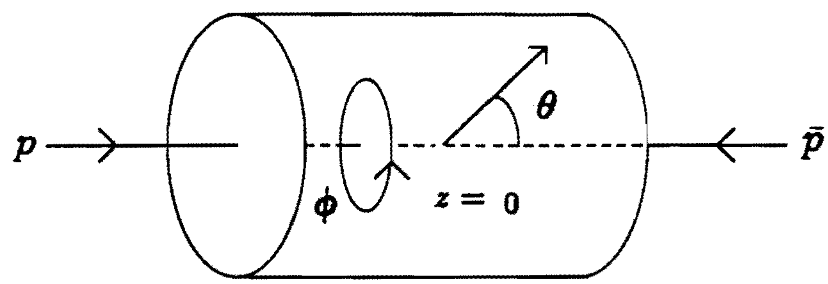

Figure 2.2: Orientation of the CDF Detector Coordinate System.

calculations for Jet Broadening involves both the lowest order terms ($2 \Rightarrow 2$) plus the case where one gluon is radiated ($2 \Rightarrow 3$). The fundamentals of these calculations will be discussed below and then the specific Jet Broadening calculations will be presented.

2.1.1 Natural Variables for $p\bar{p}$ Events

Before discussing QCD in greater detail, it is useful to define a few terms which are the natural variables for describing the experimentally measured quantities in $p\bar{p}$ interactions. The orientation of the CDF coordinate system is shown in Fig. 2.2. The proton beam travels in the $+\vec{z}$ direction and the antiprotons travel in $-\vec{z}$. For an event to be well measured, the $p\bar{p}$ collision must occur within about 100 cm of $z = 0$, the center of the detector. The transverse energy of a parton is defined as:

$$E_t^i = E^i sin\theta^i,$$

where θ^i is the angle between the beam line and the momentum direction of parton i, and E^i is the energy of the parton. The total transverse energy of the event is then:

$$E_t = \sum_{i=1}^{n} E_t^i,$$

where the sum runs over all the partons in the event.

Compared to the parton collision energies (typically greater than 30 GeV), the parton masses are taken to be zero[1]. In this limit the pseudorapidity:

$$\eta^i = -ln(tan\frac{\theta^i}{2}),$$

and rapidity:

$$y^i = \frac{1}{2}ln\frac{E^i + p_z^i}{E^i - p_z^i},$$

of parton i are equal; E^i and p_z^i represent the energy and longitudinal momentum of parton i, respectively. These parameters describe the location of partons in the detector and the longitudinal boost of the parton collision frame.

The angle ϕ^i represents the azimuthal angle around the beam such that

$$E_x^i = E_t^i cos\phi^i,$$

and

$$E_y^i = E_t^i sin\phi^i.$$

Since the parton masses are taken to be zero, the components of the parton momentum are written as 'energy vectors' E_x, E_y, and E_z, instead of momentum vectors.

2.1.2 Order $O(\alpha_s^2)$ Predictions for QCD Jet Events

As mentioned earlier, the $O(\alpha_s^2)$ QCD predictions describe the type of event shown in Fig. 2.1. Interactions between the different constituent quarks and gluons are treated as separate subprocesses. Feynman diagrams and the corresponding matrix elements are used to evaluate the contribution of each subprocess to the total cross section for $p\bar{p}$ hard collisions. The cross section for the subprocess in which partons 1 and 2 collide and produce partons a and b can be written in the form

$$d\hat{\sigma}/d\hat{t}\ (1 + 2 \Rightarrow a + b) = |M|^2/(16\pi\hat{s}^2),$$

[1]The valence quarks that make up protons and antiprotons have masses less than 1.0 GeV.

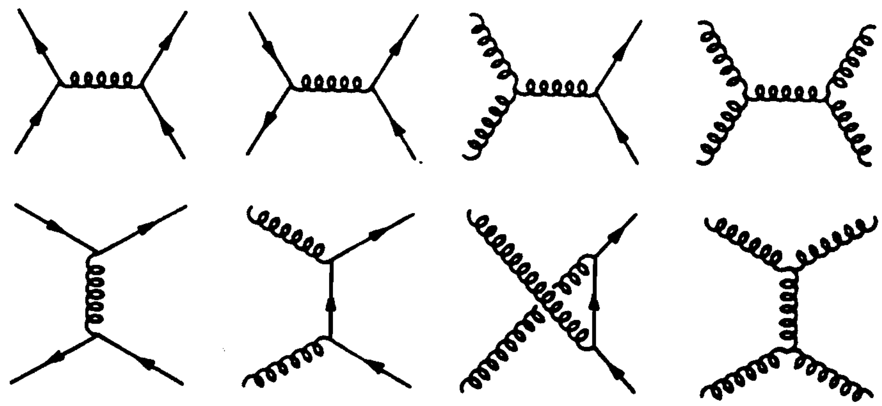

Figure 2.3: Feynman Diagrams for 2⇒2 subprocesses.

where $\hat{s} = (P_1 + P_2)^2$, $\hat{t} = (P_1 - P_a)^2$ and $\hat{u} = (P_1 - P_b)^2$. Figure 2.3 shows the Feynman diagrams for the $2 \Rightarrow 2$ subprocesses and Table 2.1 contains the squared matrix elements for each subprocess[12].

More complicated processes also contribute to the simple $2 \Rightarrow 2$ process. For example, possible loop diagrams are shown in Fig. 2.4. Integration over these loops diverge when the gluon momentum is allowed to go to zero. The diagrams in Fig. 2.4 are shown in terms of their contributions to the loop integrations as discussed in detail in Ref. [13]. The leading log approximation (LLA) parameterizes the coupling constant such that the contributions of the leading terms from the loop integrations are included. In addition to the one-loop diagrams shown in the Figure, more loops are possible and can be included in the coupling as discussed in Ref. [14]. For this analysis, the one-loop LLA parameterization of the coupling constant is sufficient and has the form:

$$\alpha_s(Q) = 1/(Bln(Q^2/\Lambda^2)),$$

where $B = (33 - 2f)/12\pi$ and f is the number of quark flavors (see Appendix A). The energy parameter Λ, is seen as the boundary between having quasi-free quarks and gluons, and having quarks and gluons in the tightly bound clusters which form hadrons.

Table 2.1: Squared Matrix Elements for 2⇒2 Process; q and q' indicate distinct quark flavors.

Subprocess	$\|M\|^2/g_s^4$
$qq' \Rightarrow qq'$, $q\bar{q}' \Rightarrow q\bar{q}'$	$4/9\ \dfrac{\hat{s}^2+\hat{u}^2}{\hat{t}^2}$
$qq \Rightarrow qq$	$4/9\left(\dfrac{\hat{s}^2+\hat{u}^2}{\hat{t}^2} + \dfrac{\hat{s}^2+\hat{t}^2}{\hat{u}^2}\right) - 8/27\ \dfrac{\hat{s}^2}{\hat{u}\hat{t}}$
$q\bar{q} \Rightarrow q'\bar{q}'$	$4/9\ \dfrac{\hat{t}^2+\hat{u}^2}{\hat{s}^2}$
$q\bar{q} \Rightarrow q\bar{q}$	$4/9\left(\dfrac{\hat{s}^2+\hat{u}^2}{\hat{t}^2} + \dfrac{\hat{u}^2+\hat{t}^2}{\hat{s}^2}\right) - 8/27\ \dfrac{\hat{u}^2}{\hat{s}\hat{t}}$
$q\bar{q} \Rightarrow gg$	$32/27\ \dfrac{\hat{u}^2+\hat{t}^2}{\hat{t}\hat{u}} - 8/3\ \dfrac{\hat{u}^2+\hat{t}^2}{\hat{s}^2}$
$gg \Rightarrow q\bar{q}$	$1/6\ \dfrac{\hat{u}^2+\hat{t}^2}{\hat{t}\hat{u}} - 3/8\ \dfrac{\hat{u}^2+\hat{t}^2}{\hat{s}^2}$
$qg \Rightarrow qg$	$\dfrac{\hat{s}^2+\hat{u}^2}{\hat{t}^2} - 4/9\ \dfrac{\hat{s}^2+\hat{u}^2}{\hat{s}\hat{u}}$
$gg \Rightarrow gg$	$9/4\left(\dfrac{\hat{s}^2+\hat{u}^2}{\hat{t}^2} + \dfrac{\hat{s}^2+\hat{t}^2}{\hat{u}^2} + \dfrac{\hat{u}^2+\hat{t}^2}{\hat{s}^2} + 3\right)$

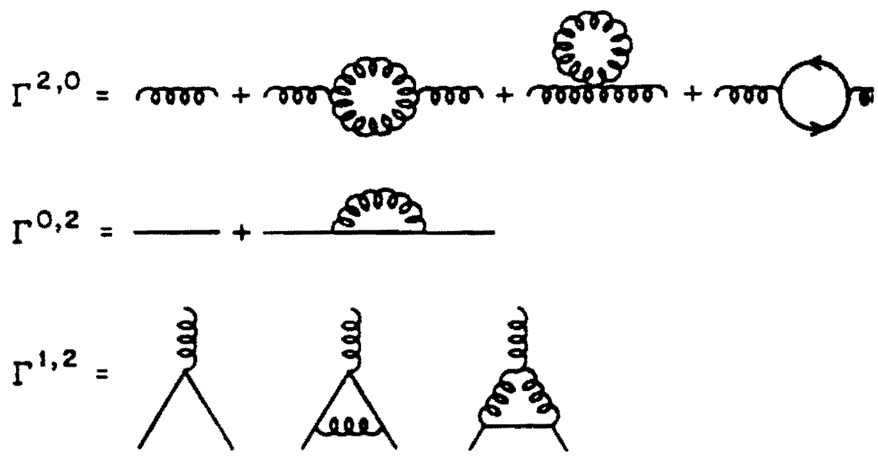

Figure 2.4: Loop diagrams for $2 \Rightarrow 2$ process.

It is introduced into the theoretical framework as a method of avoiding divergences in the loop integrations. The value of Λ is empirically determined from deep inelastic scattering experiments and typically ranges from 0.20 to 0.40 GeV. The scale of the event, Q, is chosen to reflect the the momentum transfer, or hardness, of the collision. In jet events, the choice of scale is somewhat ambiguous and thus predictions are made for a range of scales, typically $Q = E_t$ to $Q = E_t/4$. As long as Q is much larger than Λ, α_s will be relatively small and perturbative QCD can be applied.

As shown in Fig. 2.5, the value of α_s decreases with increasing Q. The property that $\alpha_s \rightarrow 0$ as $Q \rightarrow \infty$ is called 'asymptotic freedom' and is a result of color charge carried by the gluons. Unlike QED, the presence of color charge in the gluons allows the gluons to interact with each other. This is a manifestation of the non-Abelian nature of the QCD gauge group. A phenomenological explanation of the decrease in coupling with an increase in energy is based on the idea that in a hadron, the color charge of the constituent quarks is surrounded by a cloud of gluons and virtual $q\bar{q}$ pairs. Since the gluons themselves carry color, the net effect of this shielding is an increase in the color charge. With increasing collision energy, the cloud of gluons and $q\bar{q}$ pairs is penetrated further and a smaller color charge is observed. Thus, as the energy of the interaction

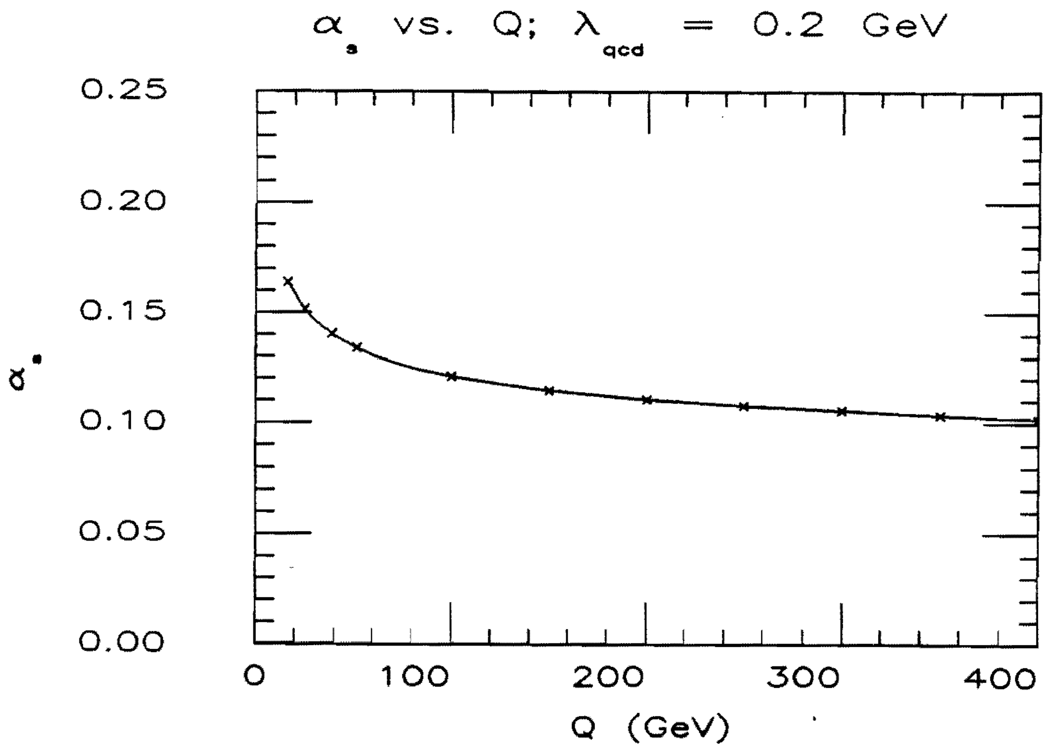

Figure 2.5: Running of α_s , leading log approximation, $\lambda = 0.2$ GeV.

increases, the value of coupling decreases. In QED, by contrast, the photons that make up the electric field around the charged particles do not carry charge; here effect of higher energy collisions is to expose more bare charge and thus increase the value of the coupling.

Now that the contribution of each parton subprocess has been evaluated, the distribution of parton momenta within the parent proton or antiproton must be considered. These distributions are called 'structure functions' and they predict the fraction of incoming hadron (proton or antiproton) momentum carried by each constituent parton. The structure function for parton 1 in hadron A is designated $f_A(x_1)$, where x_1 represents the fraction of the logitudinal momentum carried by the parton. Typically a parton carries less than 30% of the colliding proton energy, and thus the center of mass energy of the parton-parton collision is considerably lower than twice the beam energy. For the case in which partons 1 and 2 in hadrons A and B collide, the invariant mass

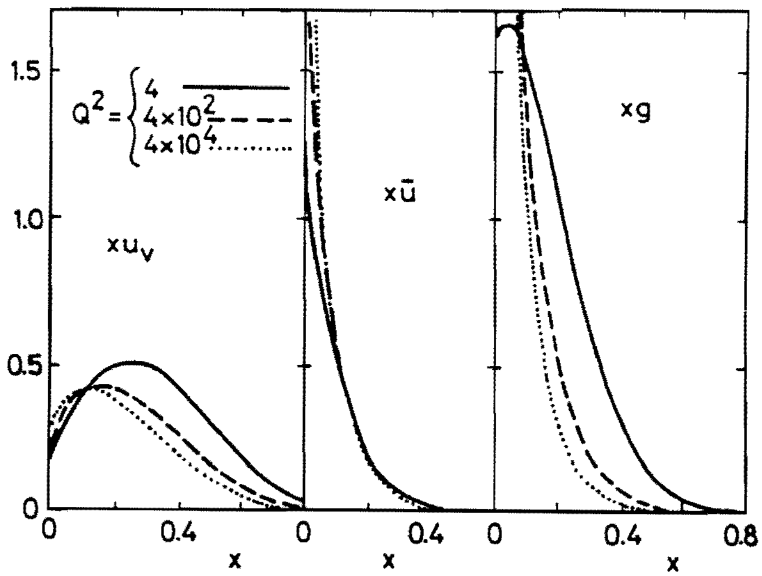

Figure 2.6: Q^2 (GeV/c^2) Evolution of Structure Functions for Duke and Owens 1.

of the of the 1-2 system, as before, is $\sqrt{\hat{s}}$, where $\hat{s} = x_1x_2s$, and s is the invariant mass of the A-B system.

Proton structure functions for quarks and antiquarks have been measured from deep inelastic scattering of electrons, muons and neutrinos on Hydrogen targets. By invoking the momentum sum rule, which states that the sum of the fractional momenta of all the partons in a proton should add up to one, constraints on the gluon distribution are imposed, and gluon structure functions are derived. The electron, muon and neutrino scattering experiments are performed at lower energy than the Tevatron energy, typically $Q^2 \leq 10\ GeV^2$. The energy dependence of the structure functions is included in the QCD predictions through the use of the Altarelli-Parisi equations (see, for example, Ref. [15]). Two common parameterizations for quark and gluon distributions are Eichten et al. (EHLQ) [16] and Duke and Ownes (DO) [17]. Figure 2.6 shows how one set of structure functions, DO1, evolves with Q^2. The low energy end of the CDF jet data corresponds to $Q^2 \approx 1000\ GeV^2$ and typical x of about 0.05.

Knowing the $2 \Rightarrow 2$ matrix elements and the proton and antiproton structure functions, the cross section for the process in which partons $1 + 2 \Rightarrow a + b$, can be written[10] as:

$$\frac{d\sigma}{dE_t} = \frac{E_t}{32\pi S^2} \int dy_a dy_b \frac{f_A(x_1)}{x_1} \frac{f_B(x_2)}{x_2} < |M^{12\to ab}|^2 >, \tag{2.1}$$

where the invariant mass of the colliding $p\bar{p}$ pair is $\sqrt{S}$, and y_i is the rapidity of outgoing parton i. The structure functions $f_A(x_1)$ and $f_B(x_2)$ correspond to parton 1 in proton A and parton 2 in antiproton B. Note that x_i can be expressed in terms of the rapidity of the outgoing partons [18]:

$$x_1 = (E_t/\sqrt{S})[e^{y_a} + e^{y_b}],$$

$$x_2 = (E_t/\sqrt{S})[e^{-y_a} + e^{-y_b}].$$

The $< |M^{12\to ab}|^2 >$ term represents the summation over all initial parton pairs (1,2) and over the subprocesses for 1 + 2 $\Rightarrow$ a + b, listed in Table 2.1 (these have been averaged over both spin and color). Figure 2.7 shows the results of evaluating equation 2.1 in a rapidity range which corresponds to the coverage of the CDF central detector, $-1.1 < y < 1.1$.

2.1.3 Order $O(\alpha_s^3)$ Calculations for QCD Jet Events

In addition to the $2 \Rightarrow 2$ process described above, there are more complicated processes to consider. The next order term in α_s includes processes such as $gg \Rightarrow q\bar{q}g$, $g\bar{q} \Rightarrow \bar{q}gg$, $q\bar{q} \Rightarrow q\bar{q}g$, or $gg \Rightarrow ggg$, where one of the incoming or outgoing partons radiates a gluon. These processes can result in events which have three well-separated jets in a detector. Examples of the diagrams for this process are shown in Fig. 2.8, a list of the subprocesses is shown in Table 2.2, and the squared matrix elements for each subprocess are given in Ref. [19].

To calculate the rates for three-jet events, the effects of gluon radiation must be included for both initial and final state partons. The probability that a particular parton will emit a gluon is represented in terms of the variable z (see Ref. [20]):

$$z = \frac{Q^2}{\hat{s} + Q^2}.$$

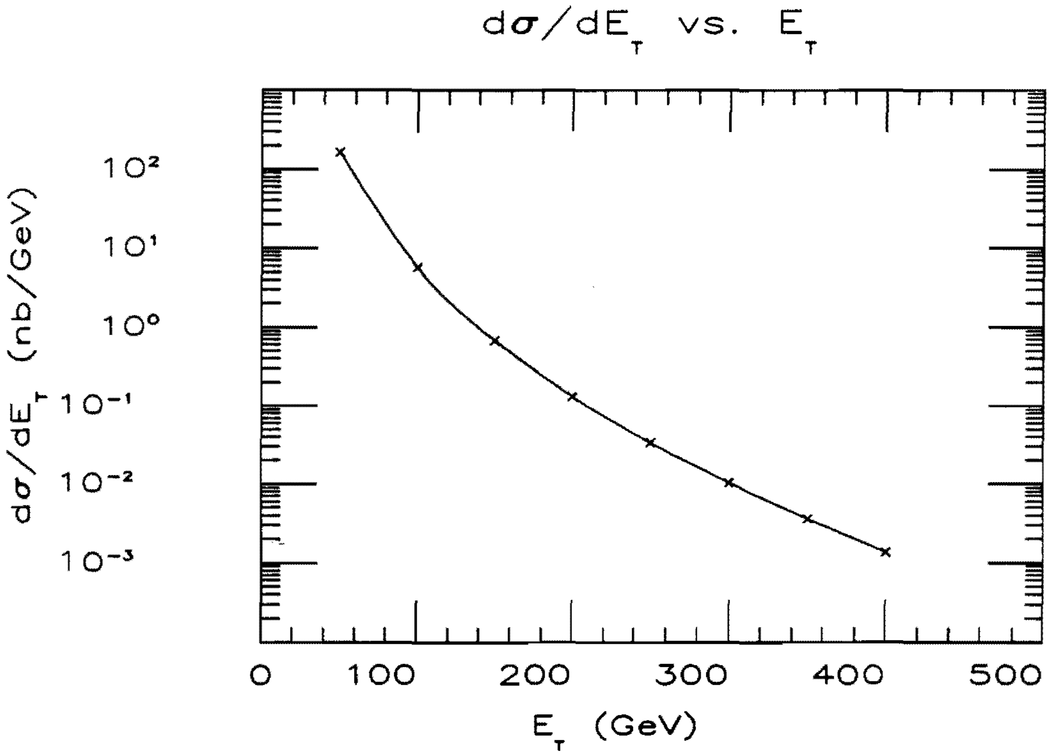

Figure 2.7: Cross section for 2⇒2 process $\lambda = 0.2$ GeV, Duke and Owens 1, all partons within $-1.1 < y < 1.1$.

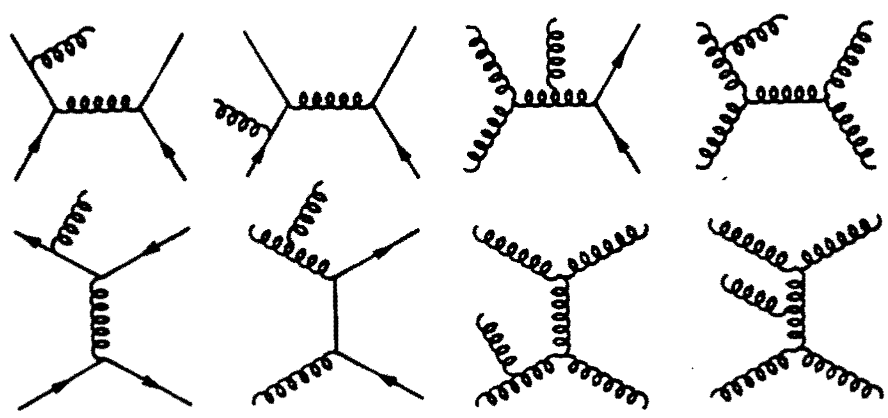

Figure 2.8: Examples of Feynman Diagrams for 2⇒3 subprocesses.

Table 2.2: 2⇒3 Subprocesses;q and q' represent distinct quark flavors.

2⇒3 Subprocess
$qq' \Rightarrow qq'g$
$qg \Rightarrow qq'\bar{q}'$
$q\bar{q}' \Rightarrow q\bar{q}'g$
$q\bar{q} \Rightarrow \bar{q}'q'g$
$qq \Rightarrow qqg$
$qg \Rightarrow qq\bar{q}$
$q\bar{q} \Rightarrow q\bar{q}g$
$q\bar{q} \Rightarrow ggg$
$qg \Rightarrow qgg$
$gg \Rightarrow q\bar{q}g$
$gg \Rightarrow ggg$

The probability that a quark emits a gluon is expressed by the *quark* → *quark* 'splitting function':

$$P_{qq}(z) = \frac{4}{3}\frac{(1+z^2)}{(1-z)}.$$

The splitting function diverges when the momentum of the emitted gluon is allowed to go to zero, i.e. $\hat{s} = 0$ and $z = 1$. This is referred to as 'infrared divergence', and is cancelled by the one loop vertex corrections mentioned above. For initial state radiation, incorporation of the splitting function into the structure functions is performed along with the energy dependent evolution of the structure functions via the Altarelli Parisi Equations[15]. For final state radiation, the infrared divergence is avoided by imposing a minimum P_t cut on the emitted gluon.

Another singularity arises in the evaluation of the 2 ⇒ 3 matrix elements. This so called 'collinear (or mass) singularity' corresponds to the case where the gluon is emitted collinear to the original parton. Conceptually, the problem is that there is no way to tell the difference between a single parton and a collinear parton-gluon pair. A theoretical prediction is said to be stable against collinear singularities if it does not change when the partons are split into collinear particles. In the evaluation of the three-jet matrix elements, the effects of the collinear singularity are treated by the introduction of a cut-off parameter for the angular separation between the original parton and the radiated gluon. Alternatively, as discussed below, it is possible to define an event-shape parameter which cancels the infrared divergence and is stable against the collinear singularities. The advantage of defining such a parameter is that it can be evaluated without the introduction of arbitrary angular separation and P_t cuts.

2.1.4 Underlying event

In addition to the hard scattering which has been described in the previous sections, the interaction of the spectator partons as they pass near each other produces low energy hadrons scattered over the detector; this referred to as the 'underlying event'. Since this hadronic debris will occur at wide angles to the original parton (jet) axis, as well as along the jet axis, the effect of the underlying event on experimental measurements must be accounted for before a direct comparison to theoretical predictions for hard parton-parton scattering is valid. The theoretical treatment of the underlying event is not well defined and thus further consideration of the effect of the underlying event will be postponed until Chapter 4 where the experimentally measured contribution of the underlying event will be described.

2.2 Jet Broadening

Having outlined the fundamental QCD framework for the treatment of the $2 \Rightarrow 2$ and $2 \Rightarrow 3$ processes, it is now possible to discuss the effect known as Jet Broadening. As the products of a hard parton scattering leave the interaction region they are likely to radiate energetic gluons in addition to being converted into hadrons; this combined process is referred to as fragmentation. Both hadronization and gluon emission will effect the angular distribution of the resulting cluster of particles. Typically, the size of a jet is characterized by the average opening angle, $< \theta >$, of the hadrons with respect to the original parton. If hadronization were the only process which contributed to the jet size, then the expected dependence on the energy of the original parton, E_p, would be roughly [21]

$$< \theta > \simeq \frac{0.3\ GeV}{E_p}.$$

The contribution of gluon emission to the angular distribution of fragmentation products can be visualized by considering the case in which a gluon is radiated at an angle with respect to the original parton. For small angles the hadronization products of the radiated gluon will be indistinguishable from the hadronization products of the original parton. For larger angles between the radiated gluon and original parton, the angular spread of the hadronization products will increase, leading to broader jets of particles incident on the detector. As shown in Fig. 2.6, the structure functions soften with increasing Q^2, and in a similar fashion, the momentum distribution of the fragmentation products is expected to soften with increasing Q^2. This effect arises because the probability of emitting a gluon of given energy increases as the energy of the parton increases, and thus, at higher energies, a jet is more likely to be the product of a qg, $\bar{q}g$ or gg state than of a single parton. This effect is known as 'Jet Broadening'. A detailed discussion of this effect is presented Ref. [22] and sketched in Ref. [21]. The result is that instead of becoming narrower linearly with the energy of the original parton, the jets become narrower roughly in proportion to the running of the coupling constant, i.e. logarithmically [21]. After the formalism for the Jet Broadening calculations have been developed, the effects of fragmentation and hadronization will be discussed.

2.2.1 Calculations and Predictions for Jet Broadening

To measure Jet Broadening, global event parameters are defined in the transverse plane. This is advantageous for $p\bar{p}$ collision data analysis because transverse parameters are independent of boosts in the longitudinal (along the beam) direction and thus they are insensitive to energy lost down the beampipe. The transverse thrust axis, $\vec{n_t}$, is defined as the axis in the transverse plane that has the maximum transverse energy flow:

$$T_t = MAX \sum_{i=1}^{n} \frac{|\vec{E_t^i} \bullet \vec{n_t}|}{E_t},$$

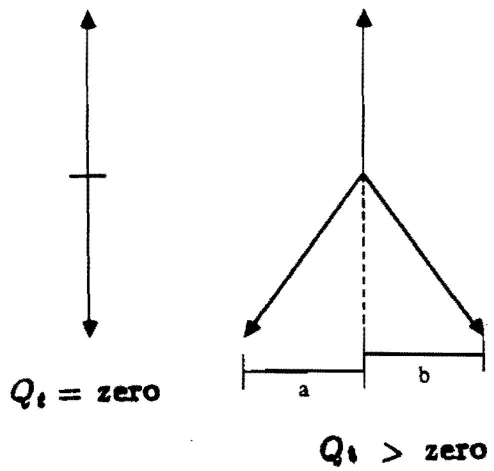

Figure 2.9: Q_t for Two and Three-Parton Events.

where T_t is the transverse thrust, and the transverse energy of the parton, $\vec{E}_t^i$ has the direction of the parton momentum vector in the transverse plane. The measure of Jet Broadening, Q_t, which will be the focus of the data analysis presented in the following Chapters, is the scalar sum of the momenta perpendicular to the transverse thrust axis:

$$Q_t = \sum_{i=1}^{n} |\vec{E}_t^i \wedge \vec{n_t}|.$$

As shown in Fig. 2.9, a 2⇒2 parton event has a Q_t which is identically zero. This feature means that Q_t is 'infrared safe', i.e. it goes to zero as the energy of an emitted gluon approaches zero. Note also that the value of Q_t does not change if one (or more) of the partons are split into collinear partons, i.e. Q_t is also stable against the collinear singularity.

The first nonzero term in perturbative QCD for Q_t is for the 2⇒3 parton configuration. The expression for Q_t in the process $1 + 2 \Rightarrow a + b + c$ has been written by Ellis and Webber[10] as:

$$Q_t \frac{d\sigma}{dE_t} = \frac{E_t^4}{512\pi^4 s^2} \int dy_a dy_b dy_c dz_a dz_b \frac{f_A(x_1)}{x_1} \frac{f_B(x_2)}{x_2} \frac{z_a z_b z_c}{Z_t} \sum < |M^{12\to abc}|^2 >, \quad (2.2)$$

where $z_i = E_t^i/(\frac{E_t}{2})$ and $Z_t = MAX(z_i)$. Since Q_t is infrared-safe and stable against the collinear singularity, it is possible to evaluate this expression without any restrictions on the minimum P_t of the partons or any requirement on the angular separation between the partons. The programs of Ellis and Webber were used to evaluate this expression and a plot of the results is shown in Figure 2.10. It should be noted that these programs are structured such that all three partons are restricted to a given rapidity range. The results shown in Fig. 2.10 have a rapidity range which corresponds to the coverage of the central CDF detector, $-1.1 \leq y_i \leq +1.1$. This calculation does not include the effects of events in which one or two of the partons are outside the central region. The contribution of this type of event to Q_t will be discussed below.

The predictions of Ellis and Webber are for the mean Q_t of all events with a given total E_t. The $< Q_t >$ at a given E_t is calculated by first summing the Q_t for all three-parton configurations for each bin of E_t , i.e. integrating equation 2.2 as shown in Fig. 2.10. Second, the lowest order estimate of the number of events in each bin of E_t is derived from the $2 \Rightarrow 2$ process. This is obtained by evaluating equation 2.1 as shown in Fig. 2.7. The mean Q_t is then calculated for each bin of E_t by dividing the sum Q_t in that bin by the number of events from the $2 \Rightarrow 2$ calculation. This gives the lowest order estimate of the mean Q_t in each bin of E_t . If there were no three-parton events, Q_t and $< Q_t >$ would be identically zero and thus a measurement of nonzero Q_t is an indication of order $O(\alpha_s^3)$ QCD processes. Figure. 2.11 shows the $< Q_t >$ which results from dividing the curve in Fig. 2.10 by the curve shown in Fig. 2.7. In these calculations the Q scale is chosen to be the E_t of the event, the structure functions are Duke and Owens 1, and LLA is used for the evolution of α_s (see Appendix A).

As shown in Fig. 2.11, the $< Q_t >$ rises as the E_t in the event increases. This Jet Broadening is in part due to the fact that Q_t, with units of GeV, is strongly correlated with the E_t in an event. For example, in a three-jet event with a given angular configuration, the Q_t rises as the E_t of the event increases. The quantity $< Q_t > /E_t$ is obtained by dividing by the $< Q_t >$ in a given bin by the E_t of that bin. This dimensionless quantity, $< Q_t > /E_t$, is a measure of the relative amount of Jet Broadening, and as the ratio of an order α_s^3 calculation to an order α_s^2 calculation, it should be roughly proportional to α_s. This quantity is similar to the ratio of the cross

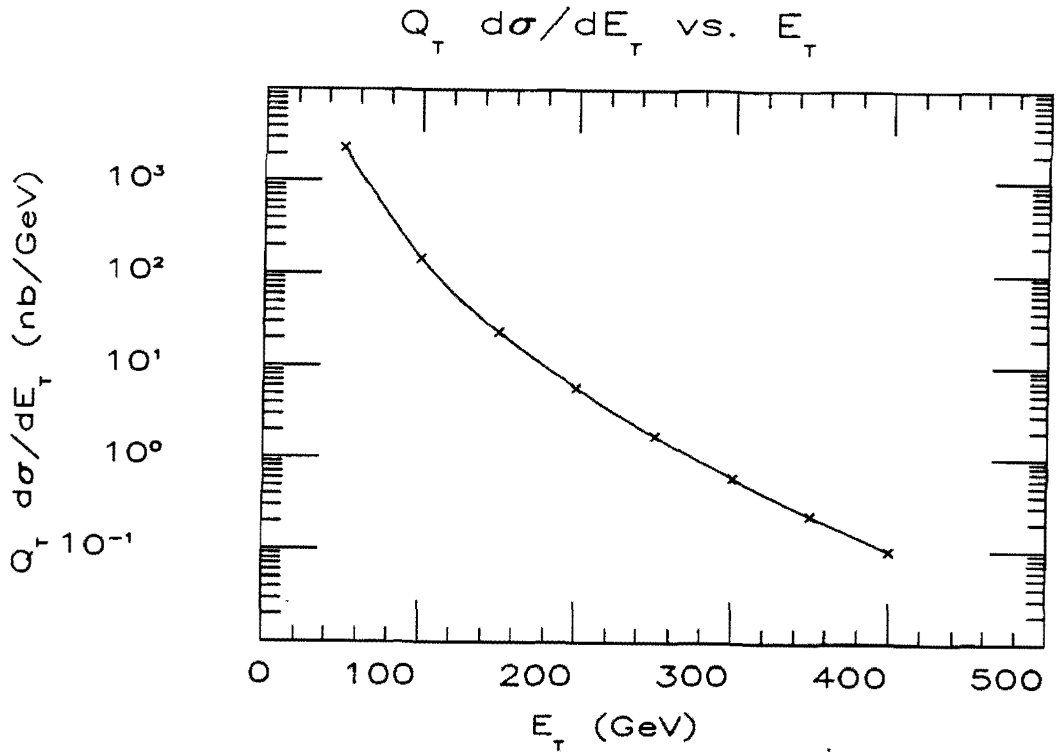

Figure 2.10: Sum Q_t for 3 parton events.

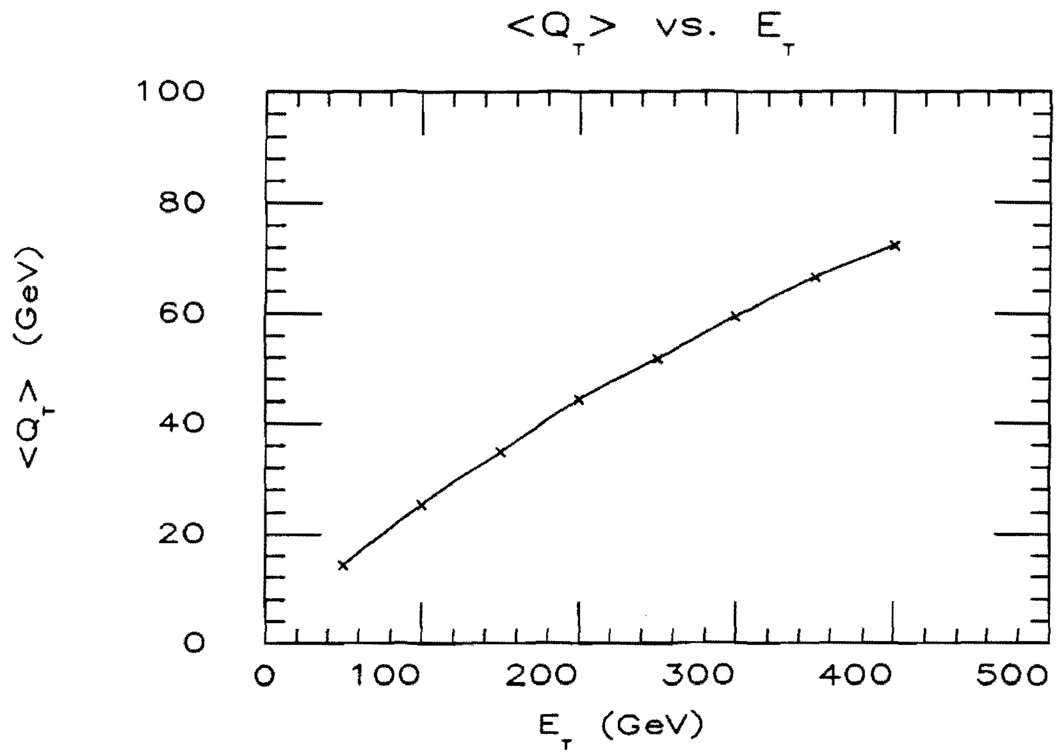

Figure 2.11: $< Q_t >$, Duke and Owens 1, Q = Et, $|\eta| \leq 1.1$.

sections of three-jet to two-jet events in terms of the uncertainty of the contributions of higher order terms, but it is free from the ambiguities (theoretical and experimental) associated with the definition and separation of three and two-jet events.

It is important to note that although there is a kinematic limit to the maximum value of Q_t for an event with a given E_t , this method of calculating $< Q_t >$ need not respect the limit since the sum Q_t is divided by the number of events from a separate calculation. For a three-parton final state, the kinematic limit on Q_t/E_t is 0.58, and for arbitrary final states it is 0.71[10]. As discussed in Ref. [10], the fact that the calculation respects the kinematic bounds is some indication of its validity in this region.

In the theoretical calculations, the value of α_s is dependent on both the choice of Q scale and on the value of Λ. Since the choice of scale is ambiguous there is spread in the predicted values of α_s, and also the Q_t/E_t ratio. Figure 2.12 shows the $< Q_t > /E_t$ curve for three choices of scale which span the typical range. The $< Q_t > /E_t$ curves all have the same shape, although the different scale introduces an overall shift in the level of $< Q_t > /E_t$. As discussed below, the shift in $< Q_t > /E_t$ is a result of a the shift in the value of α_s .

To investigate the dependence of this quantity on α_s , the same calculation was performed but the value of α_s was not allowed to evolve with E_t , i.e. the Q scale of the calculation of α_s was set at a fixed value. Figure 2.13 shows a comparison of the $< Q_t > /E_t$ curves with and without α_s running. The constant used for α_s was chosen at the lowest point on the curve, $E_t = 50$ GeV, $\alpha_s = 0.134$. The curve without α_s running shows much less energy dependence.

The structure functions also evolve with E_t (Q scale) and, in principle, could account for some of the E_t dependence in $< Q_t > /E_t$. Figure 2.14, shows the $< Q_t > /E_t$ curve for no structure function evolution compared to the fully evolved result from above. These curves display almost the same energy dependence and indicate that the behavior of the ratio $< Q_t > /E_t$ with E_t is related to the running of the coupling constant and is relatively insensitive to the behavior of the structure functions.

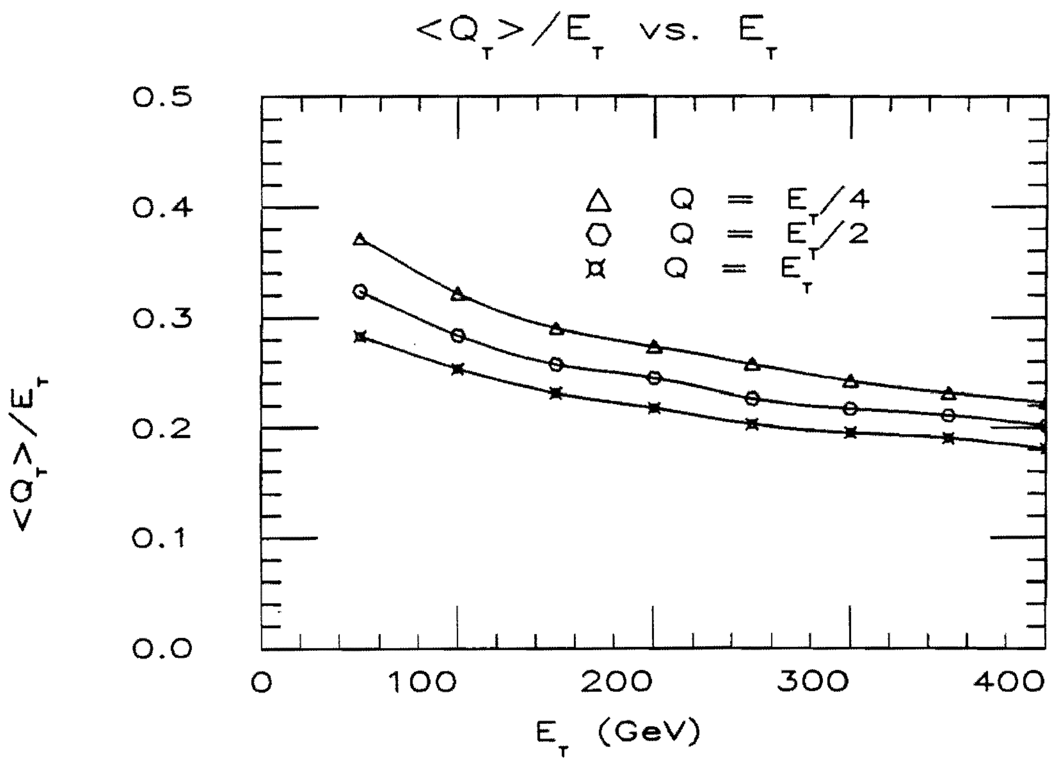

Figure 2.12: $< Q_t > /E_t$ Duke and Owens 1,$|\eta| \leq 1.1$,Q $= E_t$, E_t /2 and E_t /4.

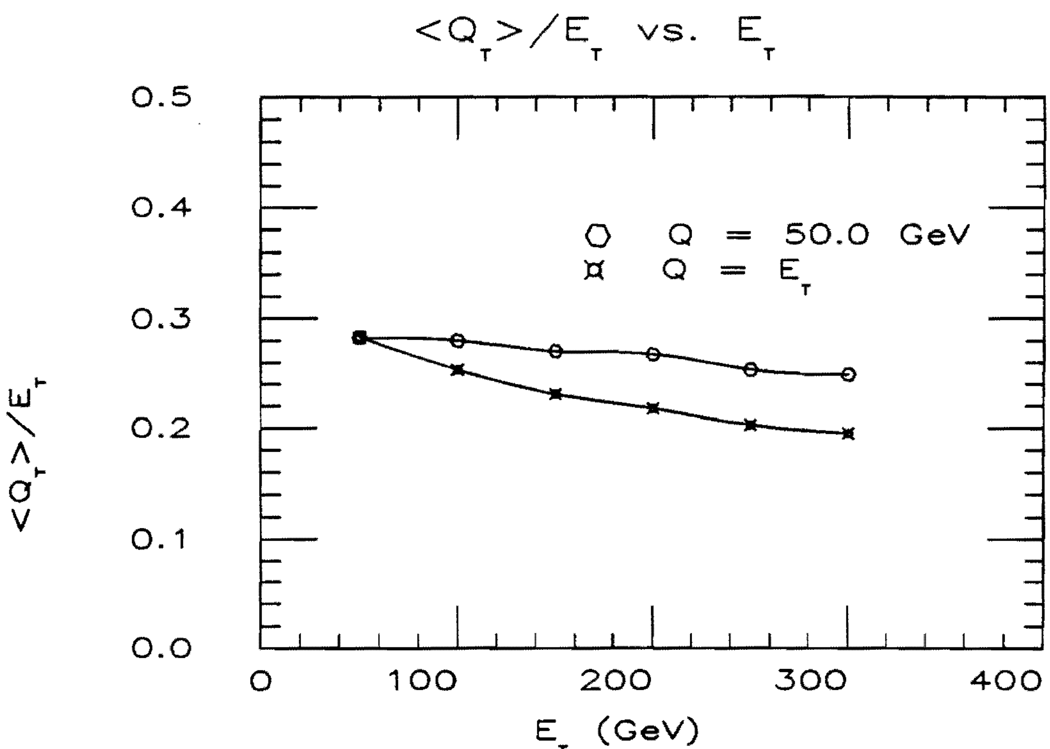

Figure 2.13: $< Q_t > /E_t$, α_s = constant and α_s running, Duke and Owens 1, Q = Et, $|\eta| \leq 1.1$.

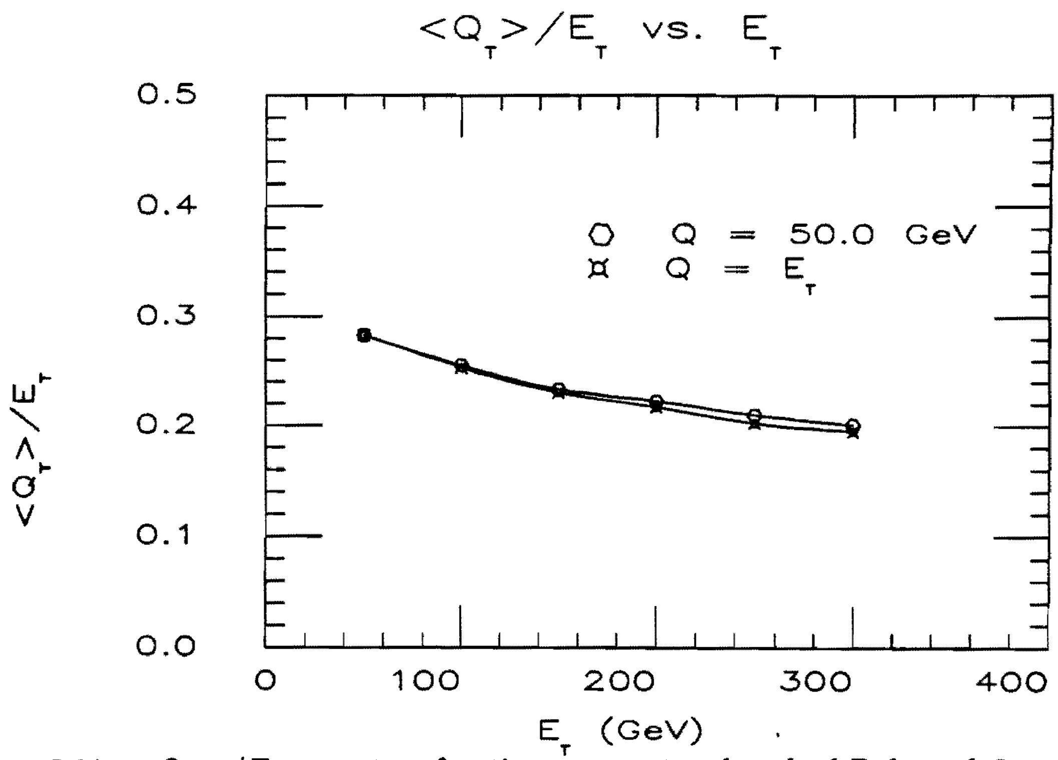

Figure 2.14: $<Q_t>/E_t$, structure functions constant and evolved Duke and Owens 1, Q = Et, $|\eta| \leq 1.1$.

The sensitivity to the choice of structure functions was investigated by using three different sets, DO1, DO2 and EHLQ1. The results of these calculations are shown in Fig. 2.15. As shown, these structure functions use different values of Λ, which results in different values of α_s, and thus they give different levels of $<Q_t>/E_t$. Since DO1 and DO2 use Λs that differ by a factor of 2, a change in the Q scale by a factor of 2 will give the same value of α_s. This is also shown in Fig. 2.15 and indicates that while the level of $<Q_t>/E_t$ is sensitive to the choice of scale, the shape of the $<Q_t>/E_t$ curve comes mainly from the running of the strong coupling constant and is not sensitive to the choice of structure functions.

2.2.2 Acceptance Issues for $<Q_t>/E_t$ Predictions

As mentioned earlier, the predictions of the Ellis and Webber programs require that all the partons be within a given rapidity range. This restriction applies to both the

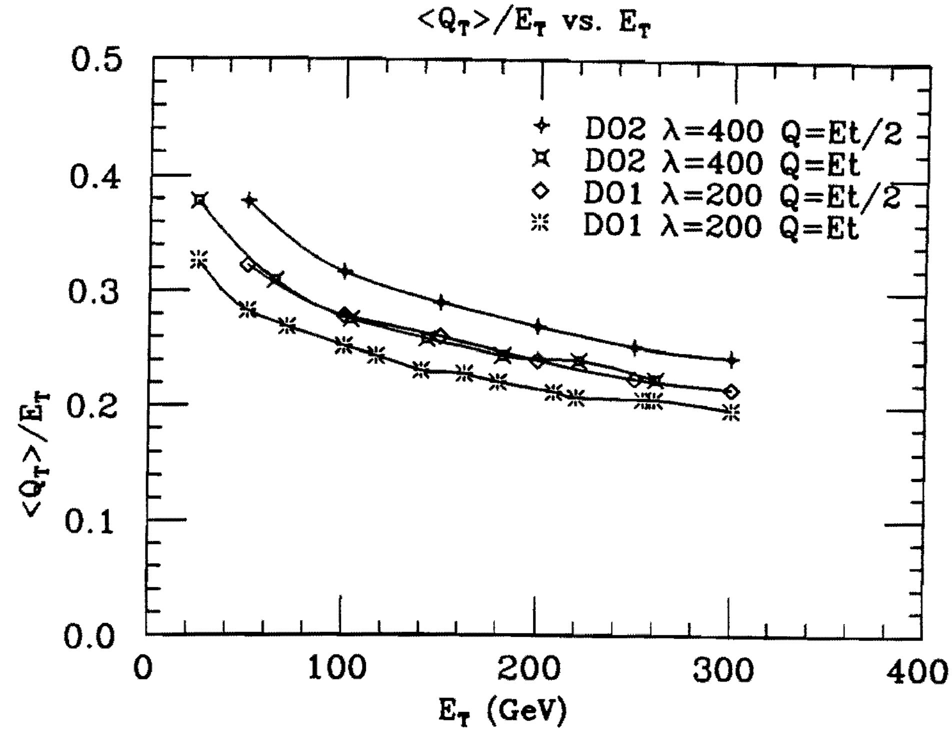

Figure 2.15: $< Q_t > / E_t$, for a variety of structure functions and Q scales, $|\eta| \leq 1.1$.

$2 \Rightarrow 2$ and $2 \Rightarrow 3$ integrations. For a more realistic comparison to the data, the effect of events with one or two of the partons outside the central region must be included. This was achieved through the use of the PAPAGENO [23], QCD Monte Carlo program. The PAPAGENO program produces individual events which are weighted by the fraction of the total cross section represented by that particular event configuration. It is then possible to apply selection criteria to these events which are different from the cuts used in the event generation, i.e. PAPAGENO can be setup to generate events with effectively no restrictions on the rapidity of the partons and then $< Q_t >$ and E_t can be calculated using only those partons which fall within the central region.

The PAPAGENO program is structured such that it evaluates one specific process at a time, i.e. it will perform either the exact $2 \Rightarrow 2$ or the exact $2 \Rightarrow 3$ calculations. When the PAPAGENO program evaluates the exact $2 \Rightarrow 3$ process, angular separation and minimum P_t cuts are typically imposed to avoid divergences in the three-jet matrix elements. To simulate the Ellis and Webber calculation of Q_t , these cuts must be

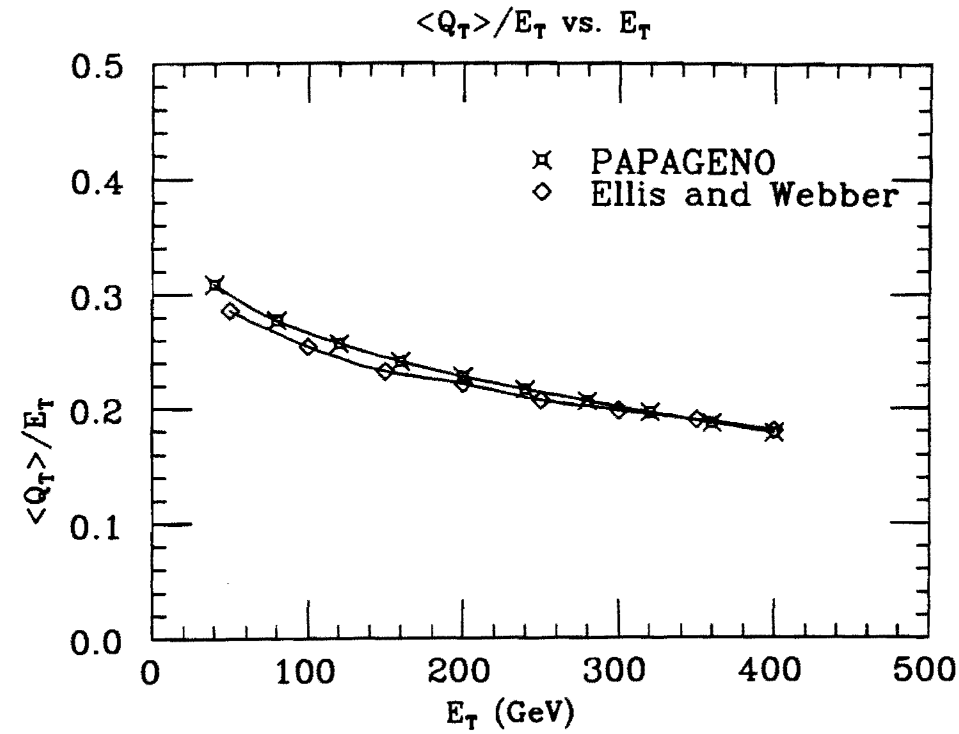

Figure 2.16: $< Q_t > /E_t$, PAPAGENO compared to the Ellis and Webber result; $|\eta| \leq 1.1$.

set to zero and thus a slight modification of the program was necessary[24]. In effect, the fact that $Q_t \to 0$ as the $2 \Rightarrow 3$ matrix element diverges was used to balance that region of the calculation.

Calculation of $< Q_t >$ and $< Q_t > /E_t$ with PAPAGENO involves running the program twice, once for the $2 \Rightarrow 2$ calculation to obtain the number of events in each bin of E_t , and once for the $2 \Rightarrow 3$ calculation of the sum Q_t in each bin. Figure 2.16 shows the $< Q_t > /E_t$ curve from PAPAGENO compared to the curve from Ellis and Webber where all the partons have been restricted to the central region. Considering the different methods of obtaining these results, the agreement is remarkably good and the difference is much smaller than the shifts associated with the choice of Q scale.

Now that is has been established that PAPAGENO can be used to reproduce the Ellis and Webber calculations, PAPAGENO can be used to study the effect of the detector acceptance. Figure 2.17 compares the central $< Q_t > /E_t$ curves (only partons falling

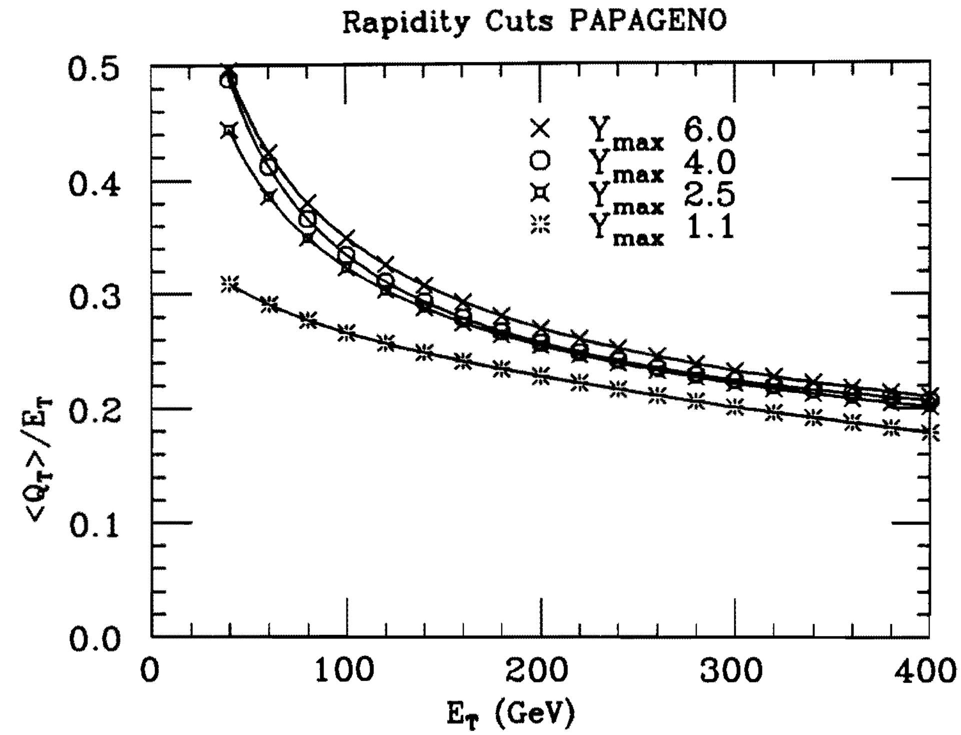

Figure 2.17: $< Q_t > /E_t$ vs. E_t calculated from partons which fall within the central ($|y| \leq 1.1$) region, for a variety of rapidity ranges used in the PAPAGENO event generation.

within $-1.1 \leq y \leq +1.1$ are included) when the partons are generated with different allowed rapidity ranges. A significant increase the in $< Q_t > /E_t$ is observed at the low E_t region. This is attributed to allowing another divergence (near the beamline) to contribute to the calculation[24]. Since this is part of QCD, it is necessary to include this effect in the calculation. As shown, most of the increase comes from the increase to $|y_{max}| = 2.5$. Beyond that, the result for the central $< Q_t > /E_t$ is essentially stable. To include the effect of the acceptance of the central CDF detector, the curve for $y_{max} = 4.0$ will be used to represent the lowest order QCD parton-level prediction for the $< Q_t > /E_t$.

The acceptance of the central detector is also affected by the z position of the event vertex since the detector will not provide symmetric coverage for off-vertex events. As discussed in Chapter 3, the distribution of verticies in the data was gaussian with σ = 35 cm. To account for the effects of this vertex smearing, a z vertex was generated randomly for every PAPAGENO event according to this distribution. The central y boundaries used in the calculation of Q_t and E_t were then shifted as if the vertex had occurred at the new vertex. While event by event this vertex smearing can change the Q_t and E_t observed in the central region, no effect was observed on the mean Q_t .

2.2.3 Fragmentation and Hadronization

Independent of the production method, whether bremsstrahlung or hard scattering, the quarks and gluons from a collision convert to hadrons before they reach the detector. The mechanism for this process is called fragmentation. As the collision partons separate, the color flux lines between them are stretched and break such that quark-antiquark pairs are created. The quark-antiquark pairs regroup to form colorless hadrons with small momentum perpendicular to the original parton direction. The result is a jet of hadrons travelling roughly in the direction of the original outgoing parton.

The predictions for $< Q_t > /E_t$ discussed thus far were based on parton level calculations without any attempt to include the effects of converting these partons into hadrons. Since hadrons, not partons, are measured in the data, some study of the effect of this process is necessary. The term 'hadronization' is used to refer specifically to the soft, low energy ($Q \approx \Lambda$) regime where quarks and antiquarks are clumped together into hadrons, while 'fragmentation' typically includes both the contributions of gluon bremsstrahlung, as well as the hadronization of the final partons. By evaluating the $2 \Rightarrow 3$ matrix element without imposing cuts on the parton energies and separation, the parton calculation for $< Q_t > /E_t$ is, in a sense, including a 'first-order' estimate of what is generally included in fragmentation. As shown by Ellis and Webber[10], the additional Q_t from hadronization is expected to be small compared to the Q_t from gluon bremsstrahlung. On the other hand, they do not consider events in which there is no gluon bremsstrahlung i.e. $2 \Rightarrow 2$ events, where hadronization would add Q_t to events which had zero Q_t at the parton level. To estimate the contribution of hadronization

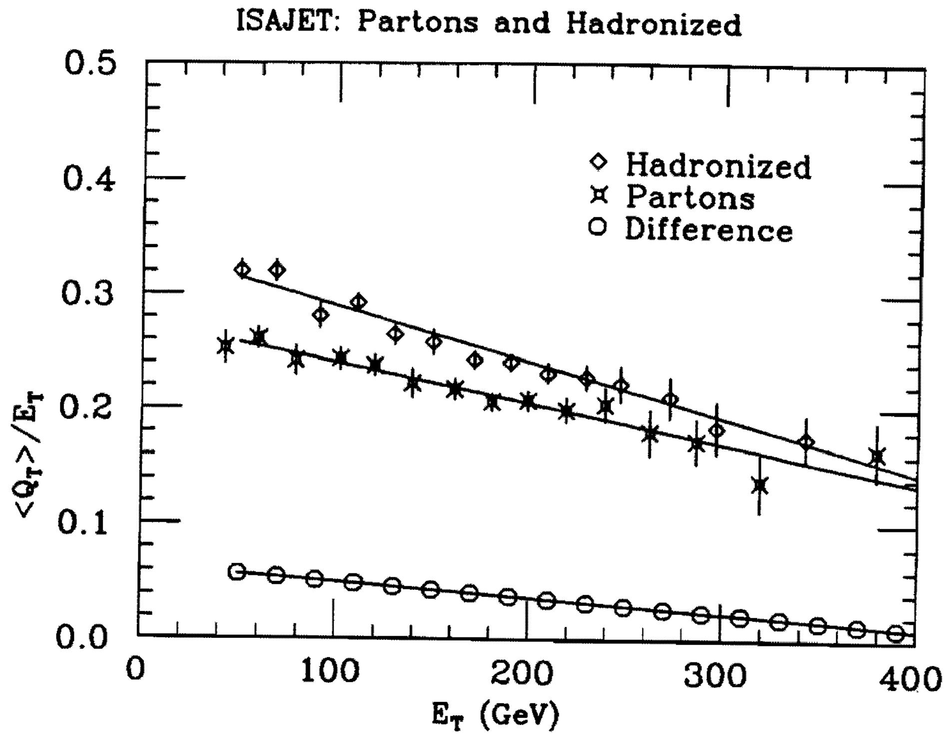

Figure 2.18: $< Q_t > /E_t$ vs. E_t , ISAJET: partons and hadronization products; solid lines are fits to the points, the difference in the fits is also plotted.

to $< Q_t > /E_t$ two approaches were used. The first employs full Monte Carlo simulation programs which perform parton-level calculations, gluon bremsstrahlung and hadronization. The second involves passing the output of an exact parton calculation (i.e. PAPAGENO) through an independent hadronization program; both of these methods are discussed below.

Traditionally, the effects of fragmentation are incorporated into leading log Monte Carlo event generation programs. Two such programs are HERWIG[25] and ISAJET[26]. Both begin with a $2 \Rightarrow 2$ scattering and then use gluon bremsstrahlung to generate multiparton events. After the bremsstrahlung has been completed, ISAJET employs the standard Feynman-Field fragmentation functions where each parton is hadronized independently. (Here 'fragmentation function' refers specifically to the hadronization of ISAJET partons.) A cut-off on the gluon mass of 6 GeV limits the contribution of bremsstrahlung and defines the separation between the parton-level QCD processes

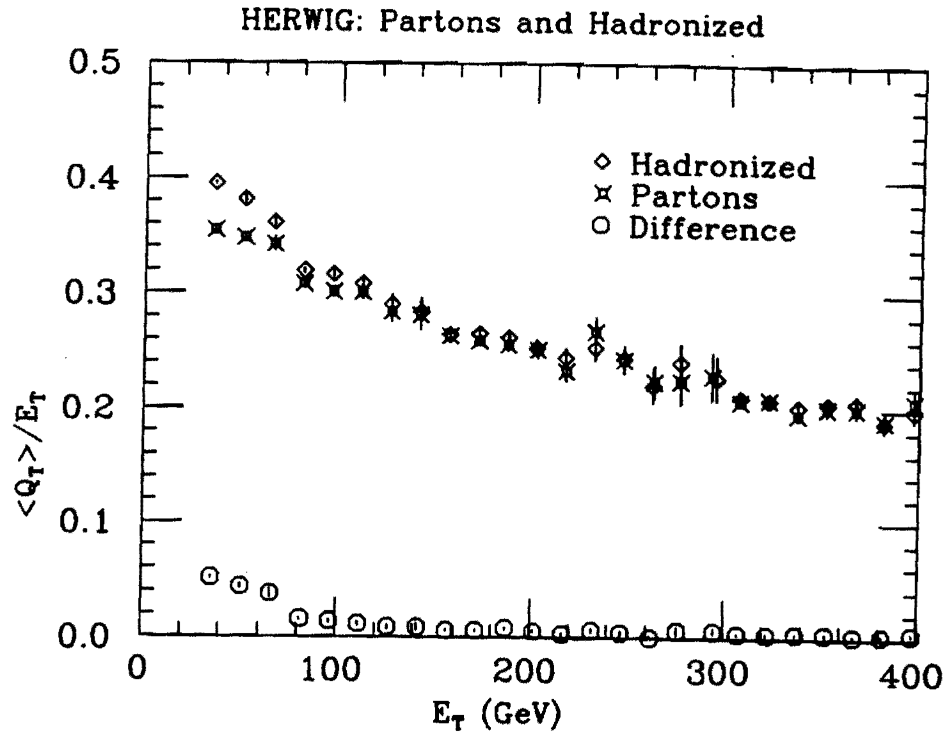

Figure 2.19: $< Q_t > /E_t$ vs. Et, HERWIG: partons and hadronization products.

and hadronization. Figure 2.18 shows the $< Q_t > /E_t$ curve for ISAJET for both partons and hadronization products. The parton calculation is performed on the 'evolved partons', i.e. the final quarks and gluons after bremsstrahlung has occurred. Note that this curve does not reflect the ISAJET prediction for $< Q_t > /E_t$ because ISAJET was modified to make the generation of events more efficient. The importance of this plot is to show the size of the effect of hadronization for one definition of the relative contributions of gluon bremsstrahlung and hadronization.

Unlike ISAJET, the HERWIG program takes into account the effects of gluon interference and coherence at the parton level. These considerations result in gluon branching angles that decrease as a shower progresses and in energy restrictions on the emitted gluons. Although HERWIG also must introduce an external cut-off on the emitted gluon mass, it is much lower (0.65 GeV) because the formalism is structured to deal correctly with low energy gluons. The HERWIG model is similar to the string fragmentation schemes and thus provides a very different estimate of the possible contribution

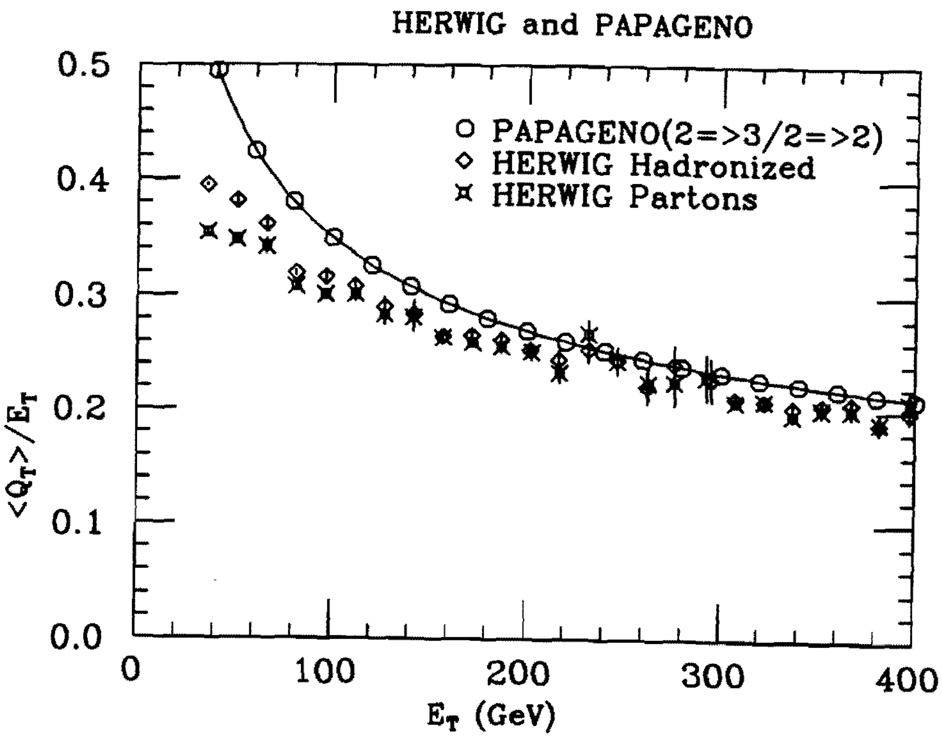

Figure 2.20: $< Q_t > /E_t$ vs. Et, parton-level calculation from PAPAGENO compared to HERWIG partons and hadronized partons. Events were generated with maximum rapidity of $\pm$ 4.0 and Q_t and E_t are calculated in the central region, $|y_{max}| \leq 1.1$.

to $< Q_t > /E_t$ from hadronization. Figure 2.19 shows separate $< Q_t > /E_t$ curves for the hadronization products and the partons from the HERWIG generator. As before, the parton level calculation of $< Q_t > /E_t$ uses the fully evolved quarks and gluons. The additional $< Q_t > /E_t$ which is attributed to hadronization is much smaller than in ISAJET as was expected from the lower cut-off on the gluon bremsstrahlung.

As mentioned earlier, the parton level QCD prediction of $< Q_t > /E_t$ from Ellis and Webber is a first order estimate of the $< Q_t > /E_t$ which would be observed in a fully fragmented and hadronized prediction. Figure 2.20 shows a comparison of the pure parton-level QCD calculation from PAPAGENO, to the HERWIG partons and the HERWIG hadronized result. In both cases the events were generated with a rapidity of $|y_{max}| = 4.0$ and the structure functions were DO1. These very different calculations show similar levels of $< Q_t > /E_t$ as well as similar E_t dependence.

Recently another approach has been developed in which the output of exact matrix element parton generators (i.e. PAPAGENO) can be hadronized. The program, called SETPRT, was based on the ISAJET routines which performed the Feynman-Field fragmentation. Since the parton level calculations (i.e. PAPAGENO) do not include additional gluon bremsstrahlung, the parameters of the fragmentation function had to be adjusted. As described in Ref. [27], PAPAGENO $2 \Rightarrow 2$ events where used as input and the fragmentation parameters were tuned to give agreement with di-jet data. This technique was used to minimize the contributions of multi-jet (multi-parton) events. To estimate the size of the contribution to $< Q_t > /E_t$ from this model of hadronization, PAPAGENO $2 \Rightarrow 2$ events were generated and hadronized without di-jet cuts, and $< Q_t > /E_t$ was calculated from the hadronization products. The results of this procedure are shown in Fig. 2.21. Although the shape of the curve is similar to the parton-level $2 \Rightarrow 3$ calculation, the overall level of $< Q_t > /E_t$ is much smaller. Without hadronization the $< Q_t > /E_t$ for the $2 \Rightarrow 2$ events is zero.

Naively one might attempt to apply this hadronization to the partons from the PAPAGENO $2 \Rightarrow 3$ calculation, but this is not possible. First, hadronization would add Q_t to events which previously had zero Q_t and thus the QCD divergence would no longer be cancelled. Second, by not imposing a cut-off on the radiated gluons, the original $< Q_t >$ calculation is, at some level, accounting for part of what is generally considered fragmentation and thus adding to this result would be 'double counting'.

Separation of the effects of hadronization from the gluon bremsstrahlung component in the measurement of $< Q_t > /E_t$ is a fundamental uncertainty and is treated differently in different models. As shown in Ref. [10], the $< Q_t >$ from the parton-level calculation should be insensitive to soft hadronization effects, while the ISAJET parameterization of the Feynman-Field fragmentation model shows a significant contribution from hadronization. The HERWIG model carries the gluon branching to a much lower gluon cut-off and thus the hadronization effects from HERWIG are small. Since the effect of hadronization is a fundamental uncertainty in the theory, the data will be corrected for everything except hadronization, and will then be compared to

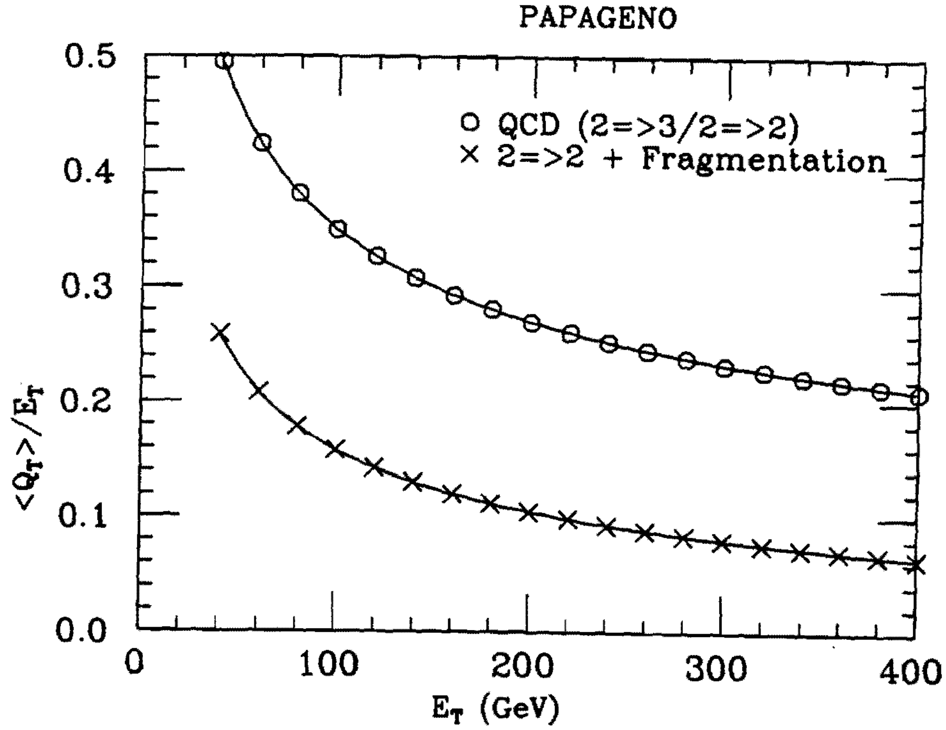

Figure 2.21: $< Q_t > / E_t$ vs. Et, parton-level PAPAGENO $2 \Rightarrow 2$ calculation plus SETPRT hadronization. Events were generated with maximum rapidity of $\pm$ 4.0 and Q_t and E_t are calculated in the central region, $|y_{max}| \leq 1.1$.

both the HERWIG and PAPAGENO results.

2.2.4 Phase Space: An Alternative Model?

Although QCD is generally accepted as the correct theory for describing the behavior of energetic, strongly interacting particles, it is useful to see how far QCD predictions differ from calculations based on phase space. For this study, the invariant mass of PAPAGENO $2 \Rightarrow 2$ events provided the input invariant mass and longitudinal boost for the 3-body phase space routine. This was done to take into account the effect of the structure functions in the initial state, since the goal of the study is to see how much 3-body phase space differs from 3-body QCD in the final state. Note that phase space does not diverge and thus it can be evaluated without angular separation and P_t cuts on the 'partons'. The $< Q_t >$ for 3-body phase space was evaluated by dividing the sum Q_t in a bin of E_t by the number of 3-body phase space events in that bin. Because phase

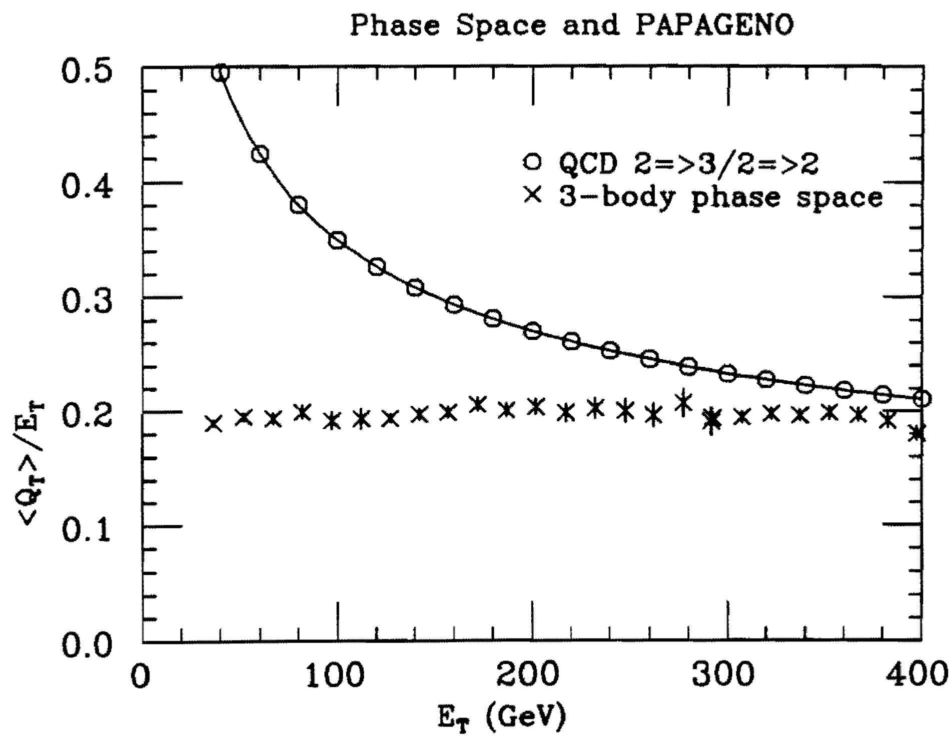

Figure 2.22: $< Q_t > /E_t$ vs. Et, parton-level QCD calculation from PAPAGENO compared to 3-Body phase space. Events were generated with maximum rapidity of $\pm$ 4.0 and Q_t and E_t are calculated in the central region, $|y_{max}| \leq 1.1$.

space does not diverge, it is not necessary to approximate the number of events with a $2 \Rightarrow 2$ calculation as must be done in the QCD prediction. The $< Q_t > /E_t$ curve from 3-body phase space partons is shown in Fig. 2.22 compared to the parton-level QCD calculation from PAPAGENO. Since $< Q_t > /E_t$ is a dimensionless quantity which is independent of the E_t in an event, the $< Q_t > /E_t$ curve is flat for 3-body phase space parton level calculation.

To come up with an alternative to the QCD predictions an attempt was made to combine the PAPAGENO $2 \Rightarrow 2$ + hadronization curve with 3-body phase space events. The fundamental assumption of this exercise is the fact that three-jet events, as well as two-jet events, are observed in the data. The PAPAGENO $2 \Rightarrow 2$ plus hadronization provides the two-jet piece of this calculation, while the three-jet events are provided by 3-body phase space + hadronization. To isolate the contribution of the three-jet events from the contribution of two-jet events, the phase space partons were required to be

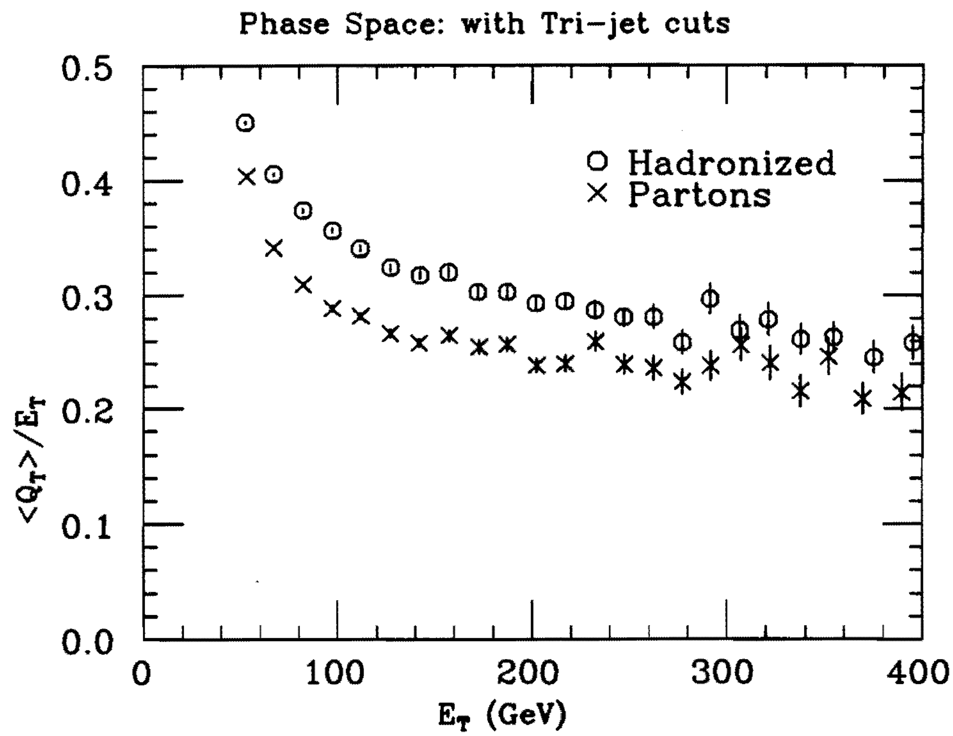

Figure 2.23: $< Q_t > /E_t$ vs. Et, separated 3-Body phase space at the parton-level and after SETPRT fragmentation has been applied. Events were generated with maximum rapidity of $\pm$ 4.0 and Q_t and E_t are calculated in the central region, $|y_{max}| \leq 1.1$.

well separated ($\geq$ 0.8 in $y - \phi$ space) and to have more than 15 GeV E_t . The events which passed the tri-jet cuts were then hadronized via SETPRT as in the di-jet case. The $< Q_t >$ for these isolated tri-jet events was calculated by dividing by the number of events which passed the cuts. This resulted in a pure $< Q_t > /E_t$ curve for three-jet events. Figure 2.23 shows the $< Q_t > /E_t$ curve for the phase space events which pass the tri-jet cuts.

Now that both a pure di-jet $< Q_t > /E_t$ curve and a pure tri-jet $< Q_t > /E_t$ curve exist, it is possible to combine them according to the number of two and three-jet events that are observed in data, i.e. roughly 20% three-jet events and 80% di-jet events. Figure 2.24 shows the result of combining the $2 \Rightarrow 2$ and 3-body phase space hadronized $< Q_t > /E_t$ curves with these relative proportions. Since the cuts are important in determining the ratio of di-jet and tri-jet events, the curve for another mixture (40-60) is also included. These two curves give an estimate of the range $< Q_t > /E_t$ which

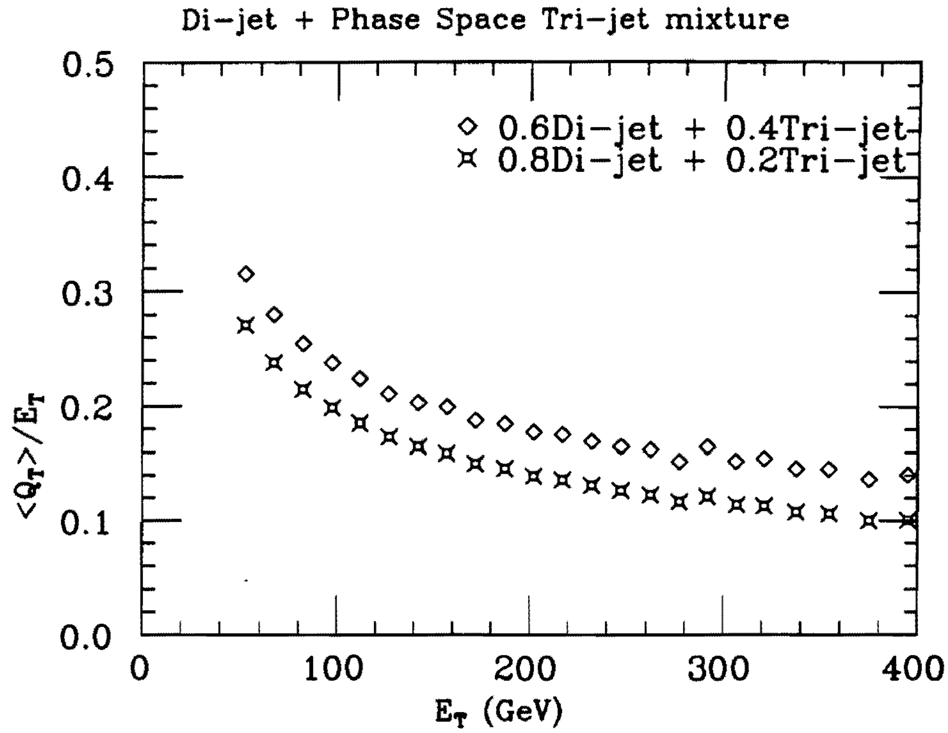

Figure 2.24: $< Q_t > /E_t$ vs. Et, combined hadronized separated 3-Body phase space with hadronized $2 \Rightarrow 2$ events. Events were generated with maximum rapidity of $\pm$ 4.0 and Q_t and E_t are calculated in the central region, $|y_{max}| \leq 1.1$.

could be obtained if there were only two-jet and well-defined three-jet events in the data.

In Chapter 5 the data will be compared to these mixed distributions, the phase space parton distribution, as well as the QCD curves discussed above.

Chapter 3

Apparatus

Theoretical predictions for the behavior of the quarks, antiquarks, and gluons can be tested by means of a high energy particle accelerator. In 1985 at the Fermi National Accelerator Laboratory (Fermilab) in Batavia, Illinois, the first proton-antiproton collisions at a center-of-mass energy of 1.8 TeV were achieved. In January, 1987, the first extended running of the Fermilab collider began and products of the $p\bar{p}$ collisions were recorded by the Collider Detector at Fermilab (CDF). As shown in Fig. 3.1, CDF was a multi-detector system with complete 2π azimuthal coverage as well as large coverage in pseudorapidity (maximum range of $-4.2 \leq \eta \leq 4.2$). The central detector consisted of charged particle tracking chambers located inside a solenoidal magnet surrounded by electromagnetic and hadronic calorimeters, muon detection chambers and a steel yoke. Symmetric forward and backward systems included electromagnetic and hadronic calorimeters, and muon chambers. Since this analysis was restricted to the central region, covering pseudorapidity $-1.1 \leq \eta \leq 1.1$, only the central detectors will be described. As all the components of the CDF detector have been discussed in detail elsewhere[28], descriptions of the detectors presented here will be brief.

A cross section of the central CDF detector is shown in Fig. 3.2. The systems used in this analysis were the Vertex Time Projection Chamber (VTPC), the Central Tracking Chamber (CTC), the central electromagnetic and hadronic calorimeters, and the end wall hadronic calorimeters. The tracking chambers were located within a uniform 1.5 Tesla magnetic field oriented along the z direction. The field was produced by a 3 m diameter, 5 m long superconducting coil[29]. In addition, the Beam-Beam Counters (BBC) were used in the trigger and as a monitor of the luminosity as discussed below.

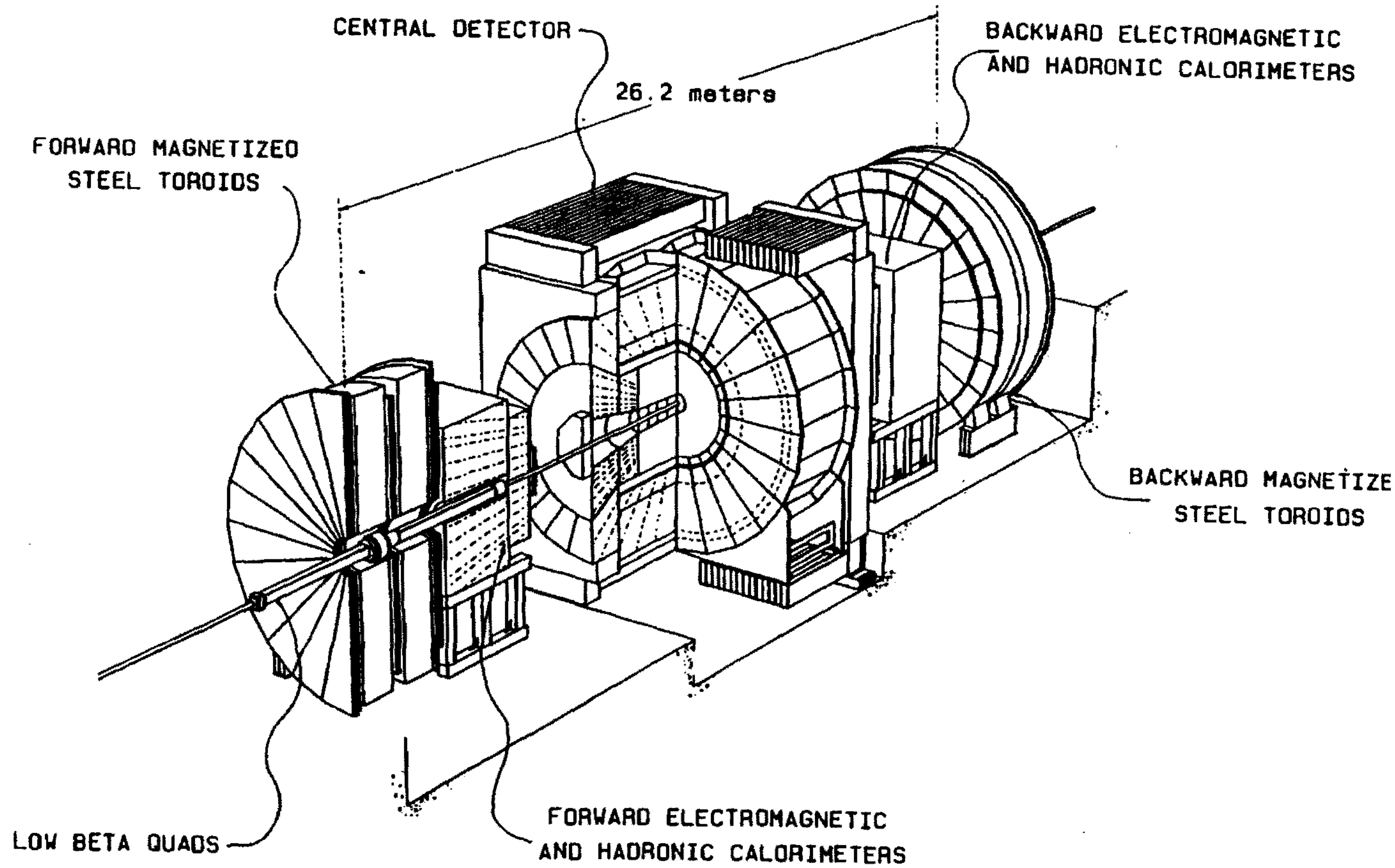

Figure 3.1: Perspective view of the components of the Collider Detector at Fermilab

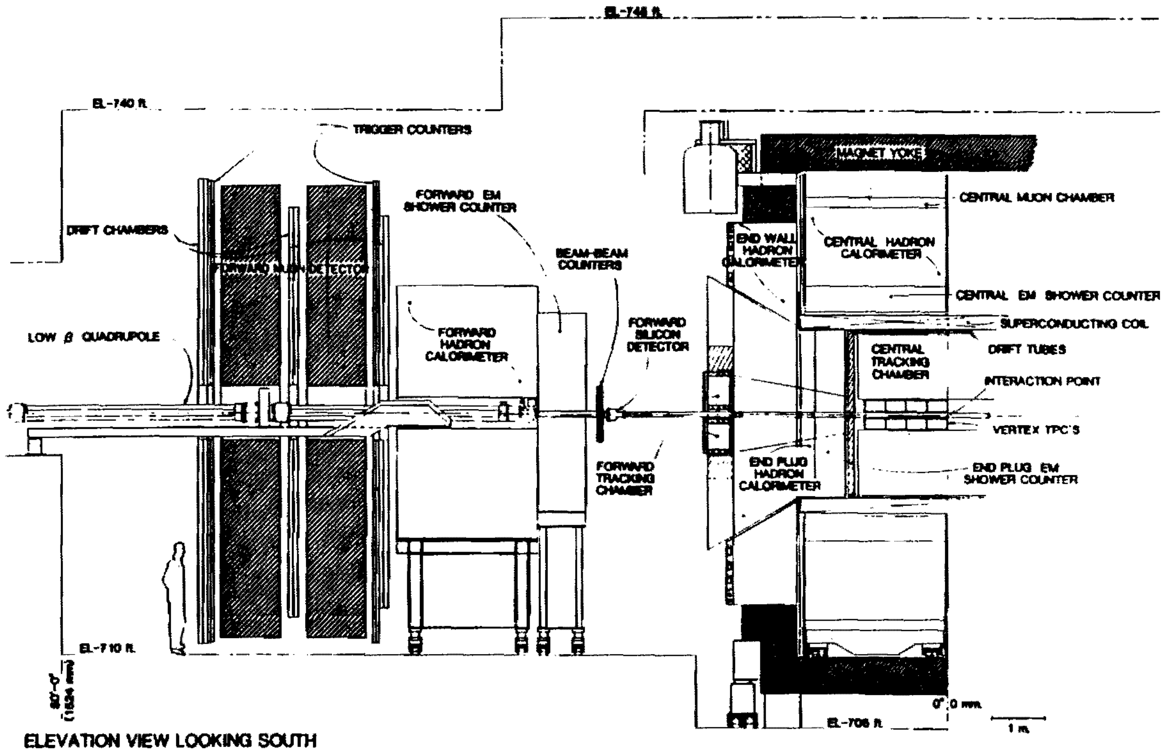

Figure 3.2: Schematic diagram of CDF detector systems.

3.1 The CDF and Accelerator Environments

Generation of the 1.8 TeV $p\bar{p}$ collisions began with negative Hydrogen ions, H^-, in a Cockcroft-Walton accelerator. A diagram of the Fermilab accelerator is shown in Fig. 3.3. After being stripped of their electrons, the protons were injected into the LINAC (Linear Accelerator), and then the Booster before they were transferred to the Main Ring (MR). The Main Ring and the Tevatron occupy the same 4 mile circumference tunnel with the Main Ring located directly above the Tevatron ring. The CDF detector was located at the B0 interaction region shown in Fig. 3.3. During normal data taking the the Tevatron beam pipe was located in the center of the CDF detector and the Main Ring beam pipe passed above it.

During Collider operation the Main Ring served two functions: 1) the production of antiprotons, and 2) to increase the energy of proton and antiproton bunches for injection into the Tevatron. Antiprotons were produced by directing the Main Ring proton beam onto a target in the $\bar{p}$ source area shown in Fig. 3.3. Antiprotons were selected from the collision products and then stored in the "accumulator". (This is the ring located in the $\bar{p}$ source area shown in Fig. 3.3.) When enough antiprotons had been collected they could be reinjected into the main ring (traveling in the opposite direction to the protons) and from there into the Tevatron.

During the 1987 run, the Fermilab accelerator delivered beam in the form of three proton bunches colliding with three antiproton bunches[30]. In this mode of collider operation, three $\bar{p}$ bunches were extracted one at a time from the accumulator, accelerated in the Main Ring and then injected into the Tevatron. Three proton bunches were then injected into the Main Ring, accelerated and injected into the Tevatron. After the six bunches were in the Tevatron, they were accelerated to 900 GeV. A series of quadrupole magnets around the B0 interaction region was then used to focus the p and $\bar{p}$ bunches to a small spot (transverse σ = 0.075 mm) near the center of the CDF detector, (Z=0 cm). With three p and three $\bar{p}$ bunches, there was 7 μsec between the bunch crossings. Once $p\bar{p}$ collisions were established in the Tevatron, the Main Ring

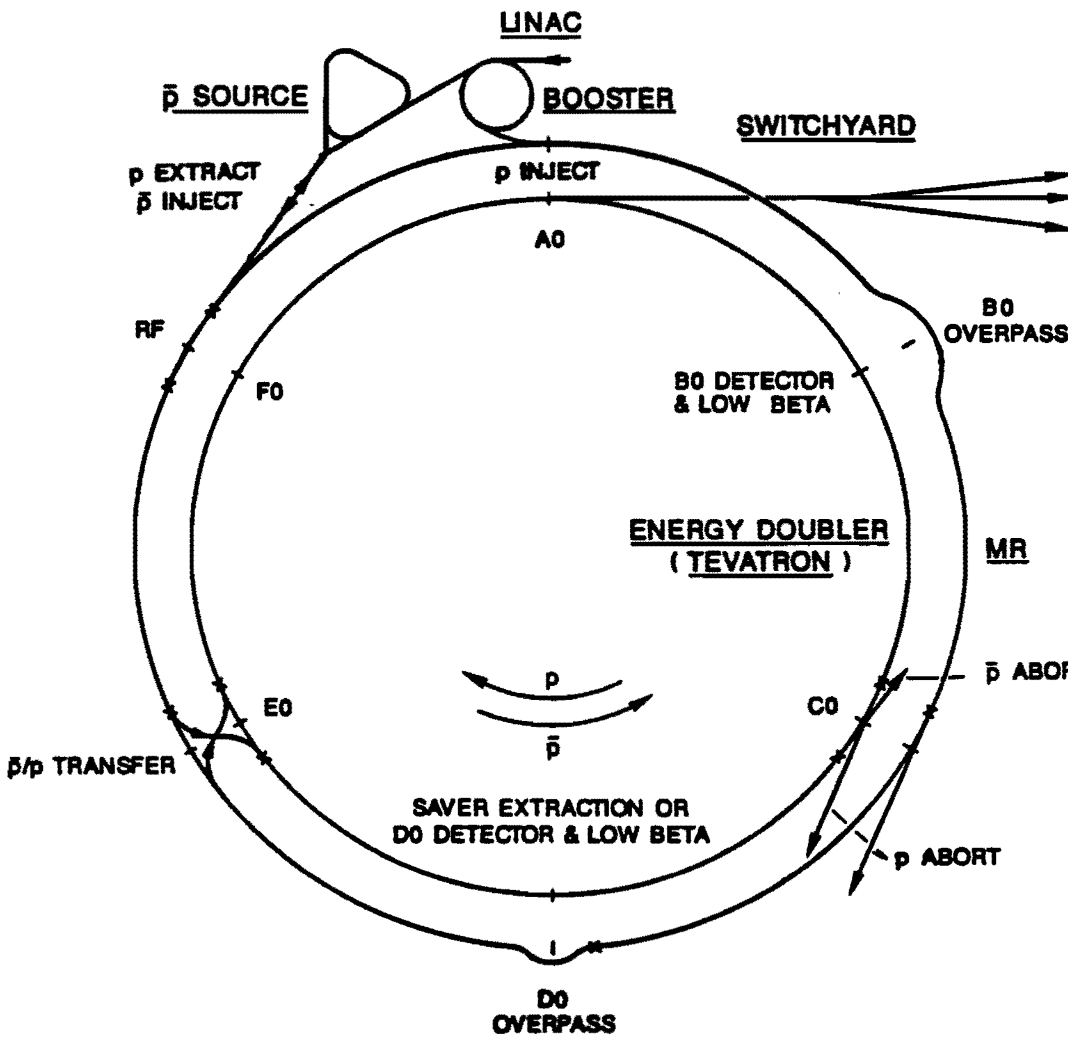

Figure 3.3: Schematic representation of the Fermilab accelerator operation in collider mode.

was used to the create additional antiprotons. The proximity of the Main Ring to the top of the CDF detector resulted in some background associated with the Main Ring proton bunches. Removal of these events is discussed in Chapter 4.

During the collider run, the instantaneous luminosity at the CDF interaction region varied over the range $0.1 \times 10^{29} \leq \mathcal{L} \leq 1.0 \times 10^{29}\, cm^{-2} sec^{-1}$. Towards the end of the run when the accelerator had stabilized, the typical instantaneous luminosity was about $\mathcal{L} = 0.5 \times 10^{29}\, cm^{-2} sec^{-1}$. This corresponded roughly to an average number of protons per bunch of 5 $\times 10^{10}$ and about 1 $\times 10^{10}$ antiprotons per bunch. The total integrated luminosity of the data recorded in the 1987 run was $\int \mathcal{L} dt = 33\, nb^{-1}$.

3.2 Tracking

3.2.1 Vertex Time Projection Chamber

Vertex Time Projection Chambers[31] were used to find the z vertex of the $p\bar{p}$ interaction for each event. Located directly outside the beam pipe, as shown in Fig. 3.2, the VTPC provided tracking for charged particles at angles between 3.5° and 176.5°. The VTPC system consisted of 8 independent modules, two of which are shown in Fig. 3.4. Each module had a high voltage central grid that divided it into two back-to-back 15.25 cm drift regions. Electrons drift away from the central grid toward the chamber endcaps which were divided into octants of sense wires and cathode pads. The R-Z coordinates of a charged particle track were determined from the drift times of the electrons. The drift times were designed to be less than the 3.5 μsec[1]. The z resolution varied with the angle of the track from 420 μm at $\theta = 90°$ to 11 μm at $\theta = 11°$. The VTPC front end electronics consisted of preamplifiers located on the chambers, amplifier-shaper-discriminator cards mounted in crates on the outside of the central detector, and FASTBUS Time to Digital Converters (TDCs).

With a 2.8 m total length, the VTPC provided good coverage of the long interaction

---

[1] This is the time between crossings when the accelerator contains six proton and six antiproton bunches.

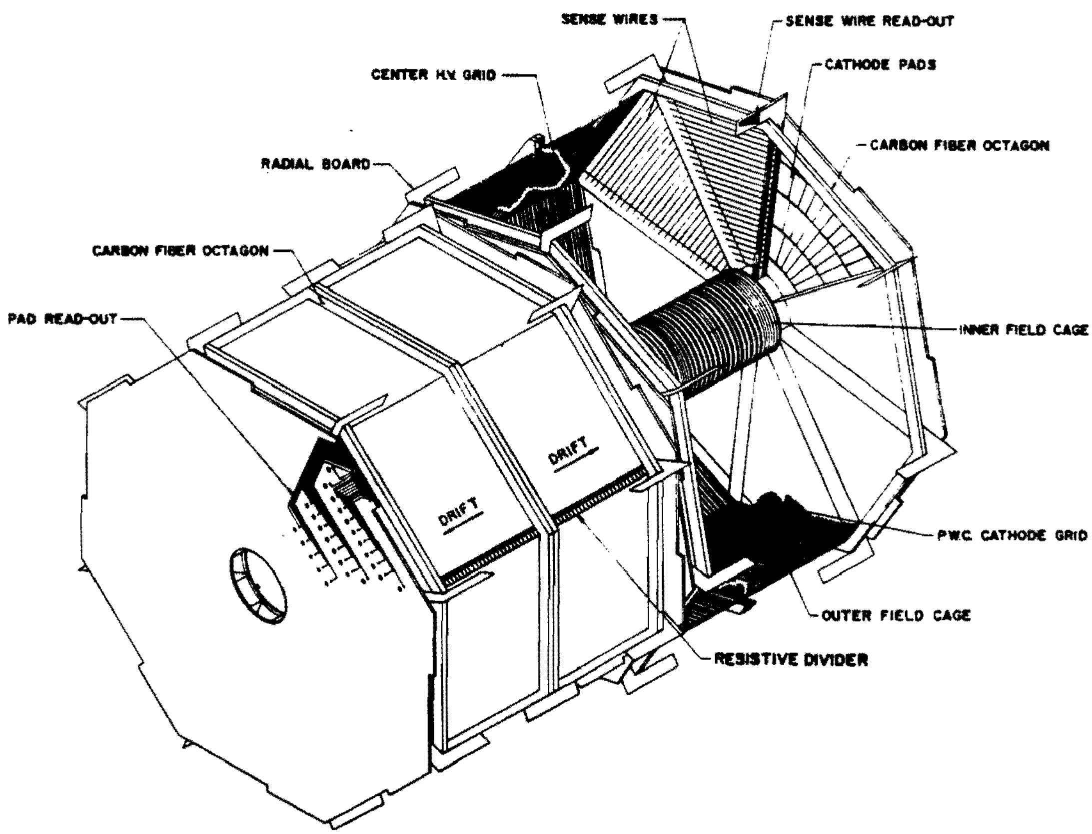

Figure 3.4: Two Vertex Time Projection Chambers;the individual modules are installed with a ϕ rotation of $11.3°$ between modules.

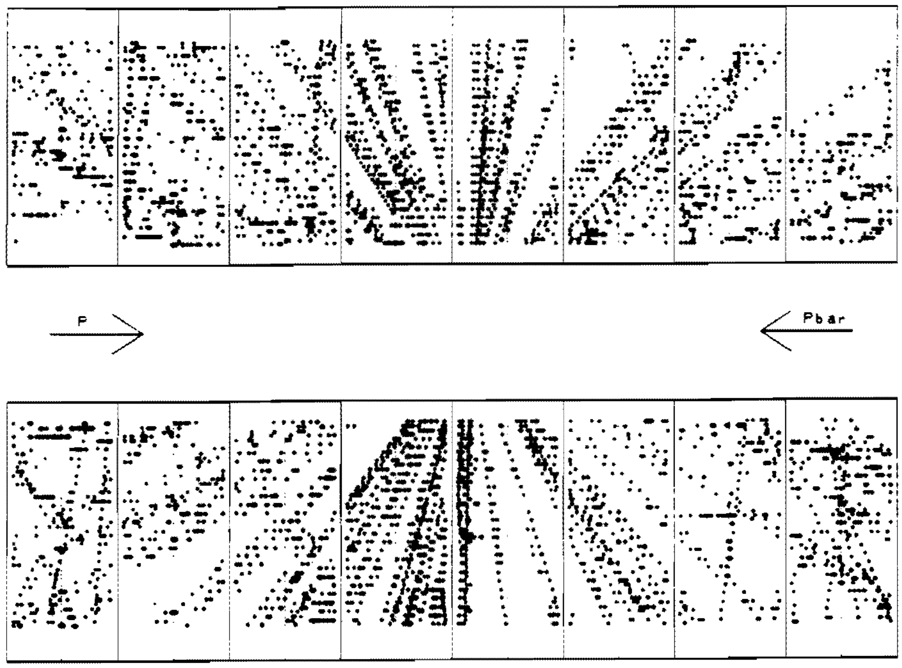

Figure 3.5: A high E_t jet event in the CDF Vertex Time Projection Chamber.

region (up to 100 cm) observed at CDF. Figure 3.5 shows a typical event as represented by the VTPC. The event vertex was reconstructed by searching for a common origin for the tracks. Figure 3.6 shows a typical vertex distribution of the high E_t data. In the coordinates defined in Fig. 2.2, the mean vertex for the high E_t data was at 4.5 cm with an r.m.s. deviation of about 35 cm.

3.2.2 Central Tracking Chamber

Surrounding the VTPC, but inside the solenoidal field, the CTC[32] provided high resolution momentum information about charged particles. The CTC was a cylindrical drift chamber 1.3 m in radius and 3.2 m long. It covered the angular region $40° \leq \theta \leq 140°$ and has track momentum resolution $\delta P_t / P_t^2 \leq 0.002 (Gev/c)^{-1}$.

The chamber was arranged in 84 layers of sense wires which were grouped into nine "superlayers". Of the nine superlayers, five were termed "axial" because their wires were oriented parallel to the beamline. The four other layers had wires at $\pm 3°$ with respect to the beam line and were called "stereo" layers. The axial superlayers were

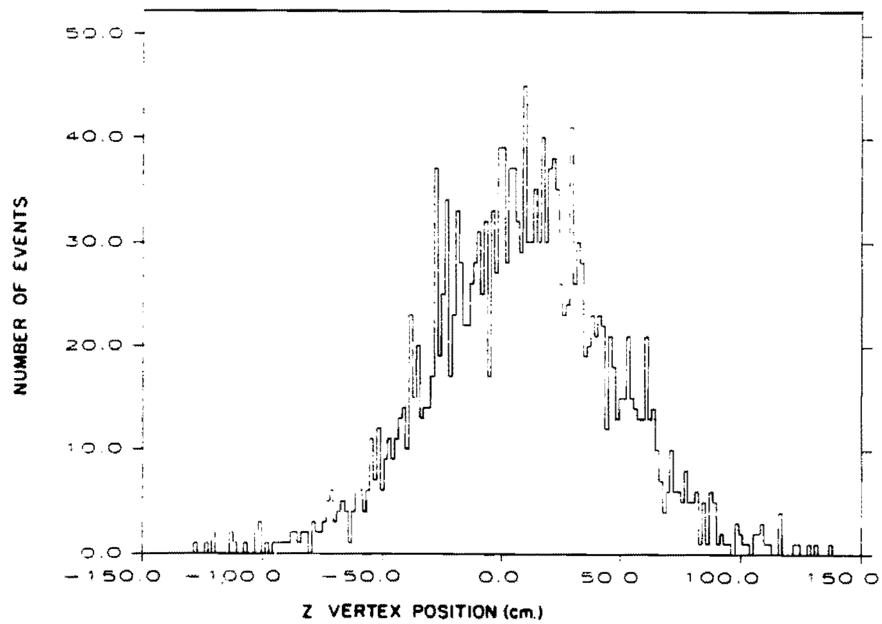

Figure 3.6: Z vertex distribution for the CDF data as reconstructed from the VTPC.

comprised of cells which contain twelve sense wires each; these layers were used for most of the pattern recognition. The stereo cells each contained six sense wires and provided additional information about the location of tracks in the $r - z$ plane. Figure 3.7 shows the endplate of the CTC. The superlayer and cell structure is clearly visible. Note that each cell of wires was rotated such that its electric field was at an angle of $\approx 45^\circ$ with respect to the radial direction. This orientation of the electric field, together with the axial magnetic field, produced a Lorentz angle which caused the drift direction of the electrons to be roughly azimuthal. The size of the cells was chosen such that the maximum drift distance in $r - \phi$ was about 35 mm.

One of the advantages of the large tilt angle for the electric field was that the drift chamber left-right ambiguity in high P_t tracks was more easily resolved since ghost tracks were rotated by a large angle ($\approx 70^\circ$) with respect to the true track direction. Figure 3.8 shows a typical jet event in the CTC; true hits and ghost hits are shown.

Each sense wire was connected to a preamplifier which was mounted on the endplate

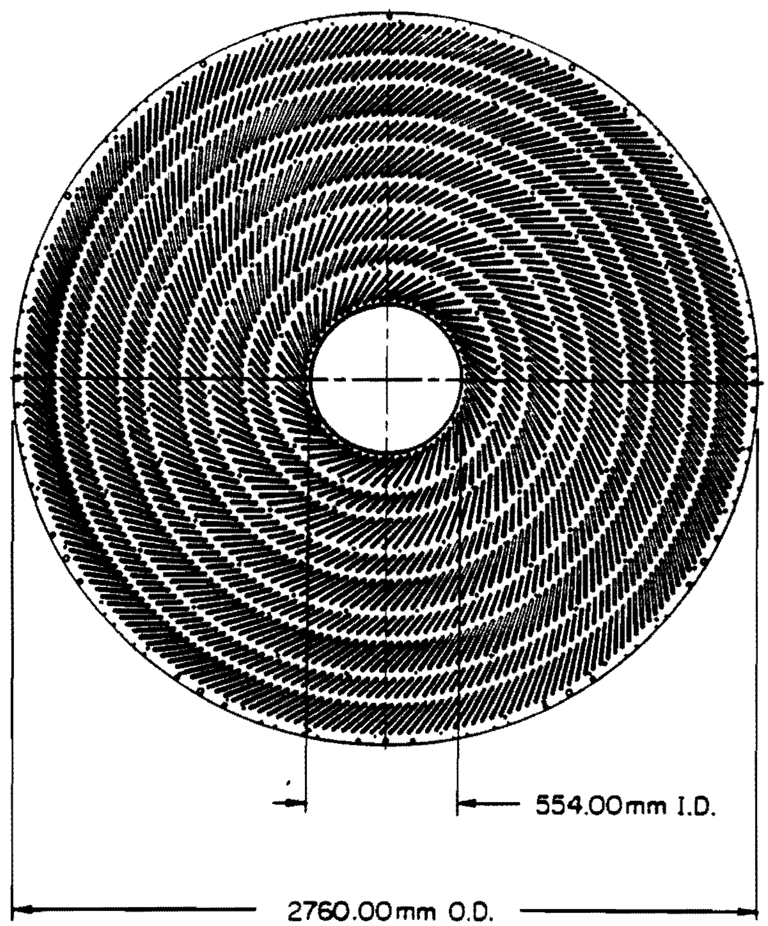

Figure 3.7: Endplate of the CDF Central Tracking Chamber; each of the tilted slots contains electrical and mechanical connections for the sense and field shaping wires. The nine superlayers are visible, as is the 45° rotation of the cells with respect to the radial direction.

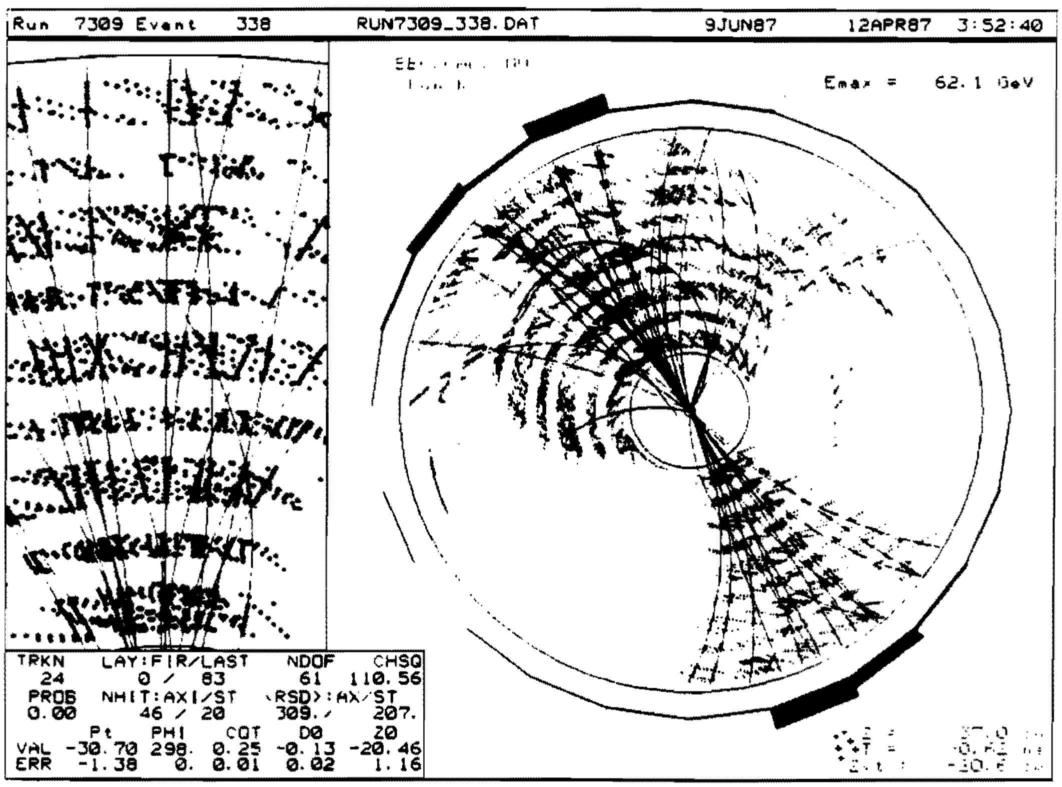

Figure 3.8: A high E_t jet event in the CDF Central Tracking Chamber. Left and right drift ambiguities are shown. A magnified view of the jet at the bottom of the figure is shown on the left.

of the chamber body. Pulse shaping and amplification were performed and a time-over-threshold logic signal was fed to FASTBUS Time to Digital Converters (TDCs) which were accessible to the rest of the data acquisition system when full detector readout was initiated.

3.3 Central Calorimeters

While the tracking chambers provided very accurate determination of the momentum of charged particles, the calorimeter provided information about the energy of both the charged and neutral particles in an event. The CDF central calorimeters were constructed in a projective tower geometry, as shown in Figure 3.9. Each "tower" covered 0.1 units of pseudorapidity and 15° in azimuthal angle ϕ ; this segmentation was small enough that a typical jet was spread over multiple towers. Each half of the central detector was divided into 24 wedge shaped modules that were arranged in a barrel around the solenoidal coil and provided nearly complete 2π azimuthal coverage. A calorimeter tower consisted of an electromagnetic shower detector[33] in front of a hadronic calorimeter[34].

The electromagnetic calorimeters were constructed of 31 layers of lead-scintillator sandwich with phototube readout and covered the angular region $39° \leq \theta \leq 141°$. The sandwich structure contained 5 mm thick sheets of SCSN-38 polystyrene scintillator interleaved with 3.175 mm lead. A schematic picture of a central wedge is shown in Fig. 3.10 with the light guides for the phototubes on the electromagnetic calorimeter. Each tower was readout by two phototubes which were located on opposite sides in ϕ and, from the balance of energy in the phototubes, the azimuthal location of the electromagnetic shower within each tower could be determined. The gaps between the individual wedges represent 4.8% of the total azimuthal angle.

The central electromagnetic calorimeter modules were calibrated in a test beam of 50 GeV/c electrons. Each module had a ^{137}Cs source attached to it and the response of the module to the source was measured. This provided a reference for calibration when

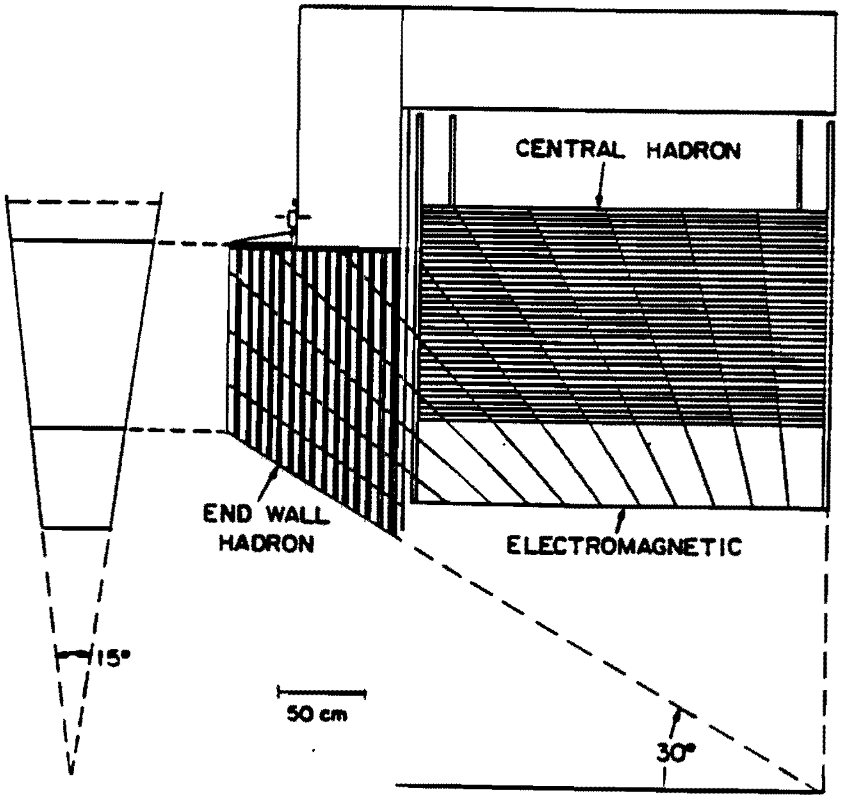

Figure 3.9: Projective tower structure of the CDF Central and End Wall Calorimeters.

the modules were installed on the central detector. Periodic "source runs" allowed the gain of each module to be monitored over long periods of time (months), while daily shifts in calibration were monitored with an LED system and a xenon flasher system. Reference [35] contains a detailed description of the calibration procedures and results. In summary, the tests showed that over the period of a month the response to 50 GeV/c electrons was reproducible within $\pm 0.4\%$ with an average energy resolution $\sigma(E)/E = 13.5\%/\sqrt{E \sin\,\theta}$.

The central and end wall hadronic calorimeters had the same tower segmentation as the electromagnetic calorimeters and covered the angular region from $30° \leq \theta \leq 150°$. The central hadronic calorimeters were comprised of 32 layers of steel-scintillator sandwich and covered $45° \leq \theta \leq 135°$. The end wall calorimeters consisted of 15 layers of steel-scintillator sandwich and covered angles $30° \leq \theta \leq 45°$ and $135° \leq \theta \leq 150°$. The central hadronic calorimeter layers consisted of 2.5 cm of steel and 1.0 cm of

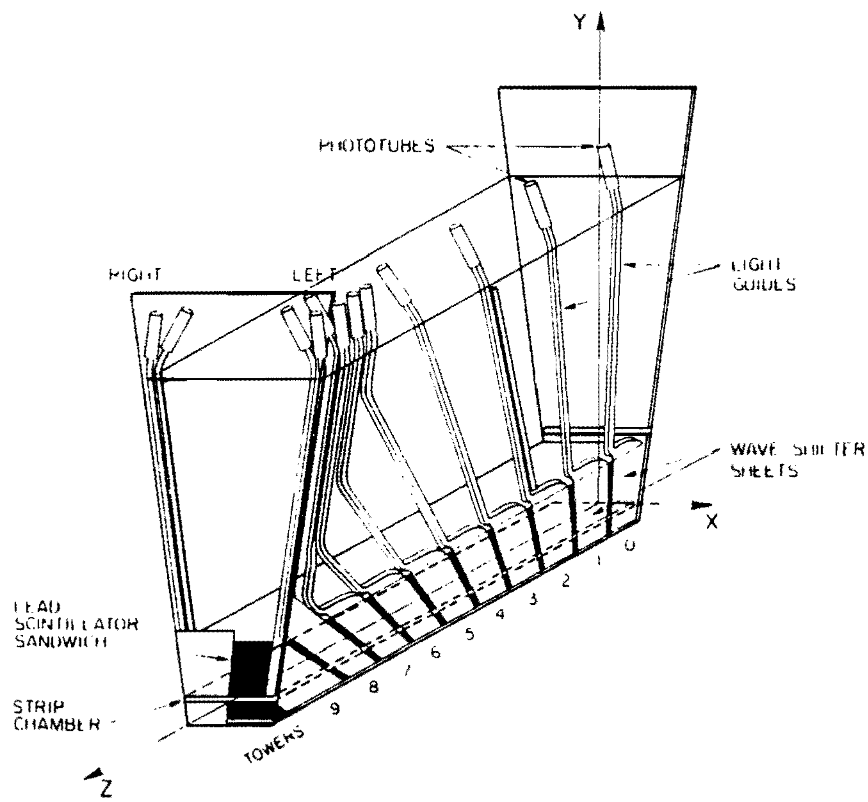

Figure 3.10: Schematic drawing of a wedge in the CDF Calorimeter showing tower structure in the hadronic and electromagnetic calorimeters, and the phototube layout for the electromagnetic calorimeters. When the wedge is in position on the detector, the Y axis represents the radial direction and X points in the azimuthal direction.

scintillator, while the end wall calorimeters were made up of 5.0 cm of steel and 1.0 cm of scintillator. The scintillating plastic sheets were shaped in the the tower geometry and waveshifters were located along the edges of the sheets. As in the electromagnetic calorimeters, light from each tower was collected by two phototubes on opposite sides in azimuth, and from the balance of signals in the two tubes, it was possible to determine the shower centroid.

Calibration of the central and endwall calorimeters was accomplished in a manner similar to the calibration of the electromagnetic calorimeters and is discussed in detail in Ref.[34]. Briefly, each hadronic calorimeter module was calibrated based on the response to test beam pions of 50 GeV/c. Before and after the test beam calibration, the response to the ^{137}Cs source on each module was also measured. As with the electromagnetic calorimeter, periodic checks of the response of the calorimeters to the sources maintained the calibration. Daily variation in response were measured with a laser pulse system. The resulting energy resolution of the central hadronic calorimeters was $\sigma(E)/E = 70\%/\sqrt{E}$ for pions up to 50 GeV[34] and at $11\%/\sqrt{E}$ for energies between 50 and 150 GeV[28]. The energy resolution of the end wall calorimeters was measured at 14% for pion energies of 50 GeV[28].

Both the electromagnetic and hadronic calorimeters used a RABBIT[36] front-end system and was interfaced to the FASTBUS Data Acquisition network. In addition, the hadron calorimeters were equipped with TDC's which were used to determine the arrival time of the signals. As discussed in Chapter 4, the hadron TDC timing information was used to reject backgrounds associated with cosmic rays and noise from the Main Ring.

3.4 Data Acquisition System

The full CDF detector consisted of roughly 75,000 electronic channels which were associated mainly with the calorimeters and tracking chambers. The front-end system, which was developed by CDF for the calorimeter readout, was called the Redundant Analog

Bus-Based Information Transfer (or RABBIT) system[36]. The calorimeters made up roughly 50,000 of the 75,000 total channels, and were serviced by 129 RABBIT crates mounted on the detector. The technique employed by the RABBIT system exploited the bunch format of the beam during collider operations. The output of each detector channel, effectively a capacitive current source, was tied to an integrating amplifier. Its output was sampled just before and immediately after a bunch crossing. The difference between the voltage levels was proportional to the signal charge. The RABBIT signals were digitized in each crate and were readout by intelligent scanners called MXs[36]. The MXs provided the interface between the RABBIT system and the FASTBUS Data Acquisition system.

The tracking chambers used commercially available FASTBUS TDC's which were readout by a FASTBUS based intelligent scanner called an SSP[37]. Together, approximately 60 MXs and 25 SSPs comprised the front end for the CDF detector. Data Acquisition was performed through a VAX cluster interfaced to FASTBUS. The entire CDF Data Acquisition FASTBUS network consisted of 53 crates, 16 cable segments, and 66 segment interconnect modules.

3.5 Trigger

The CDF trigger system was designed in a multi-level structure, as shown in Fig. 3.11, in which an event must pass the previous trigger level to be processed by the next level of the trigger. The Level 1 and 2 trigger decisions were made by custom designed FASTBUS boards based on fast analogue signals received directly from the RABBIT crates on the detector. If an event passed the Level 2 trigger, then full detector readout was initiated via the MX and SSP scanners, as indicated on the Figure. The Level 3 trigger consisted of a microprocessor farm which was developed by the Advanced Computer Program (ACP) at Fermilab and was adapted for online use by a combination of the Rutgers and Fermilab groups in the CDF collaboration. During the 1987 run only the Level 1 trigger was in actual operation although the Level 2 and Level 3 triggers

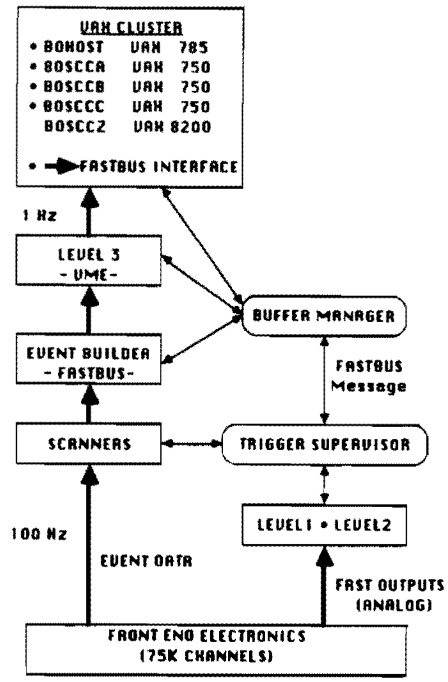

Figure 3.11: CDF Multilevel Trigger and Data Aquisition System.

were being tested in a passive mode. In this configuration, events were written directly to tape if they passed the Level 1 trigger. Details of the operation and development of the Level 3 trigger are included in Appendix B.

3.5.1 Calorimeter Trigger

While several Level 1 triggers were possible, the one of major importance to this analysis was the calorimeter sum E_t trigger. The hardware for the Level 1 calorimeter trigger consisted of ten FASTBUS crates which were connected directly to the RABBIT crates on the detector. These Level 1 FASTBUS crates were organized such that they had a one to one correspondence to the separate detector systems. Five crates were used for the electromagnetic calorimeters (Forward East, Plug East, Central, Plug West and Forward West) and similarly five crates were used for the hadronic calorimeters. The

FASTBUS boards in these crates received differential analogue signals from the RABBIT electronics via dedicated cables and performed the calculations which converted these signals into a measurement of E_t as discussed below.

The Level 1 trigger used "trigger towers" which covered 0.2 units of pseudorapidity by 15° in phi[2]. The transverse energy of a tower i was calculated in the trigger assuming an event vertex at $z = 0$,

$$E_t^i = E^i sin\theta^i,$$

where E^i represents the energy of the tower. For the 1987 data, the E_t^i summation included all towers in the central calorimeter that had more than 1 GeV transverse energy in either the electromagnetic, hadronic or in the sum of the electromagnetic and hadronic components of the tower. Due to noise problems in the plug and forward hadronic calorimeters, energy in these detectors was excluded from the sum.

3.5.2 Beam-Beam Counters

The other important part of the Level 1 trigger decision was based on the signals in the Beam-Beam Counters[38] . These counters consisted of two planes of scintillating plastic, one located on the central side of the forward calorimeter and one on the central side of the backward calorimeter as shown in Fig. 3.2. Each plane of counters covered the angular region $0.32° \leq \theta \leq 4.47°$. A coincidence of hits in both the forward and backward counters was used to define the "Minimum Bias" trigger. In general this requirement was used in conjunction with other trigger requirements since it reduced the contribution of beam gas collisions[3].

The Beam-Beam counters also provided a monitor of the luminosity. This was accomplished by recording a constant fraction of events which were only required to satisfy the Minimum Bias trigger. A Monte Carlo study indicated that the total cross section for events in the angular region covered by the Beam-Beam counters to be 43

---

[2] In the central region two detector towers ganged together in η comprise one "trigger tower".

[3] Typically beam gas collisions have all the particles moving either in the forward or backward direction, but not both.

Table 3.1: Hardware Trigger Thresholds and and Luminosity

E_t	Integrated Luminosity	Trigger Name
20 GeV	0.406 nb^{-1}	$SUM - ET - 20$
30 GeV	11.620 nb^{-1}	$SUM - ET - 30$
40 GeV	5.800 nb^{-1}	$SUM - ET - 40$
45 GeV	5.771 nb^{-1}	$SUM - ET - 45$

mb[39]. This combined with the number of events in the Minimum Bias data sample determined the absolute scale of the luminosity measurement.

3.5.3 Triggers for the 1987 Physics Run

For this analysis, the data sample was collected with the requirement of a "Minimum Bias" trigger in coincidence with calorimeter E_t above an adjustable threshold. Although the Level 1 decision was made within the 7 μsec between bunch crossings and thus caused no dead time in the system, only one event out of roughly 2500 per second could be written to tape. To keep the deadtime to a tolerable level over the wide range of luminosities, the E_t threshold on the Level 1 trigger was varied. The E_t thresholds and the corresponding integrated luminosity at each threshold are shown in Table 3.1. The numbers in the table represent the integrated luminosity used in this analysis and have a total $\int \mathcal{L} dt = 23.6\, nb^{-1}$.

Chapter 4
Offline Analysis

4.1 Calculation of Global Event Parameters from Data

Calculation of global event parameters from the raw data was accomplished by using the finely segmented calorimeter structure of the CDF detector. Conceptually, the energy of each tower was treated as if it were the energy of a particle. The location of the energy within the detector was used to determine the components of the 'particle' momentum vector in the coordinate system where the event vertex (from the VTPC) is at the origin. As described in Chapter 3, each calorimeter tower contains electromagnetic and hadronic compartments. The radii which correspond to shower maximum, determined in the test beam data ($R_{hadronic}$ = 275 cm and $R_{electromagnetic}$ = 200 cm), were used to calculate separately the transverse energy of the hadronic and electromagnetic components of a tower. The transverse energy of tower i, E_t^i, is the scalar sum of the transverse energy in the electromagnetic and hadronic components of that tower:

$$E_t^i = E_{em}^i sin\theta_{em}^i + E_{had}^i sin\theta_{had}^i.$$

The ϕ position of the energy within each tower was determined from the balance of energy in the tower's two phototubes[40] . Again, this was evaluated separately for the electromagnetic and hadronic components. A single ϕ position for the tower energy was then determined using the E_t weighted mean of the ϕ positions in the electromagnetic and hadronic components. The x and y components of the 'momentum' associated with tower i were calculated as:

$$E_x^i = E_t^i cos\phi^i$$

$$E_y^i = E_t^i sin\phi^i.$$

Note that towers were treated as zero mass particles and thus $E_t^i = P_t^i$. As the calorimeter measures energy, not momentum of particles, I have chosen to write E_t^i instead of P_t^i. The E_t of an event was defined as the scalar sum of all towers above threshold:

$$E_t = \sum_{i=1}^{n} E_t^i,$$

where n is the number of towers above threshold. The *missing* E_t of an event was opposite to the vector sum of the x and y components of the towers above threshold.

Once the E_t of each tower was calculated, it was possible to determine the transverse thrust axis from the energy flow in the events. The thrust calculator[41] uses an iterative algorithm beginning with the locations of the four highest energy particles (towers) in the event. Iterations continue until the convergence limit for the value of the thrust is reached in two successive iterations.

Figure 4.1 shows a typical event as viewed from the transverse plane with the thrust axis indicated by the line. Figure 4.2 shows the transverse energy flow with respect to the transverse thrust axis for a sample of events. (The specific event selection is discussed in the following sections and does not affect the overall features of this plot.) Here, each bin in the angle $\Delta\phi^i$ between the tower and the thrust axis, is weighted by the transverse energy of that tower. Each tower in each event is entered in this plot, and the plot represents the sum over many events. The spikes at 0° and 180° show the dominance of two jet activity in the events. There is an 180° ambiguity in the determination of the thrust axis and thus no differences between the spikes at 0° and 180° are observed.

The calculation of Q_t from the data was accomplished by using the angle $\Delta\phi^i$ between the energy in each tower and the thrust axis to determine the contribution Q_t^i of each tower above threshold:

$$Q_t^i = |E_t^i sin\Delta\phi^i|,$$

and

$$Q_t = \sum_{i}^{n} Q_t^i.$$

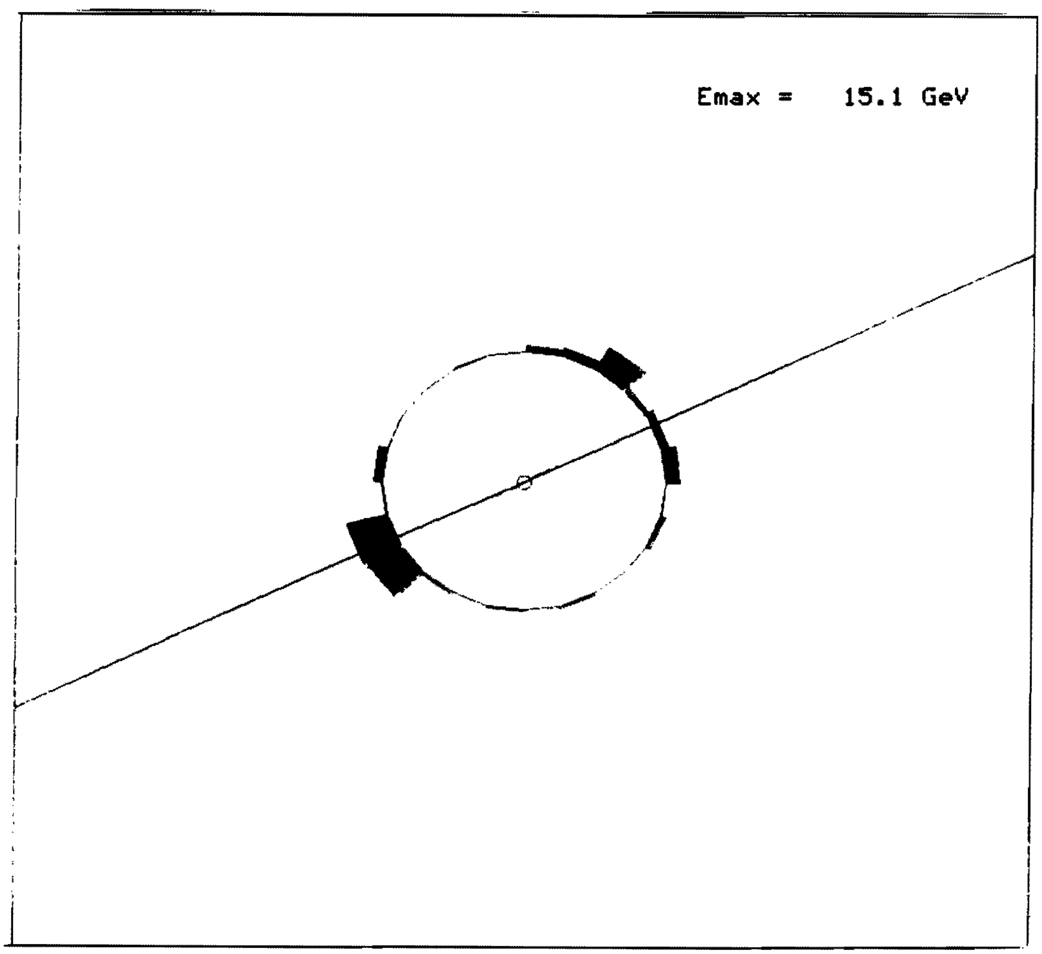

Figure 4.1: A typical event as viewed from the transverse plane. The height of each segment represents the sum (over the entire central rapidity range, -1.1 to 1.1) of the transverse energy in each ϕ slice of the detector. The line indicates the location of the transverse thrust axis.

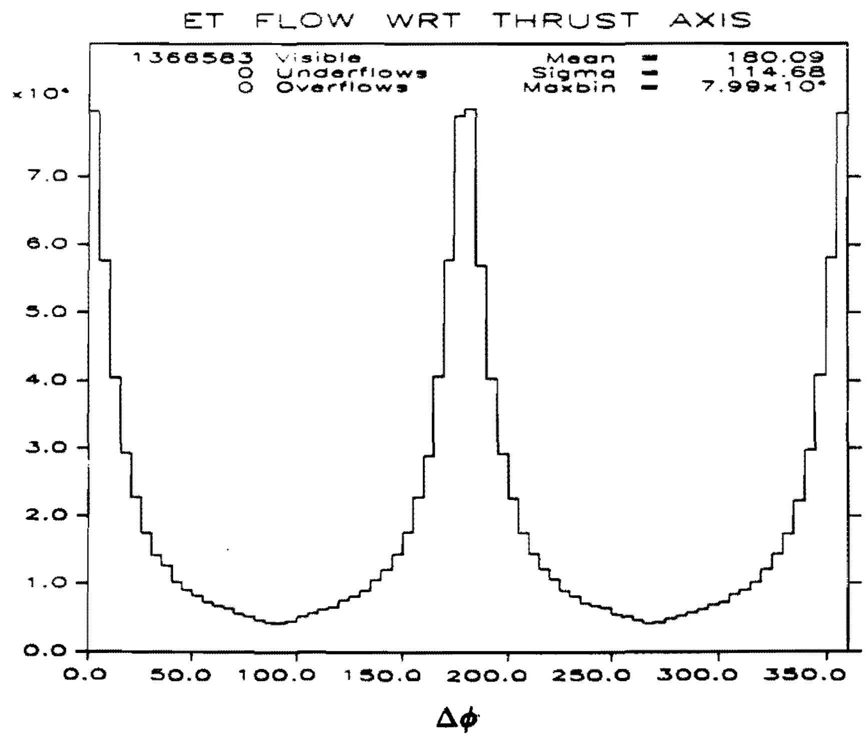

Figure 4.2: Transverse energy flow with respect to the transverse thrust axis.

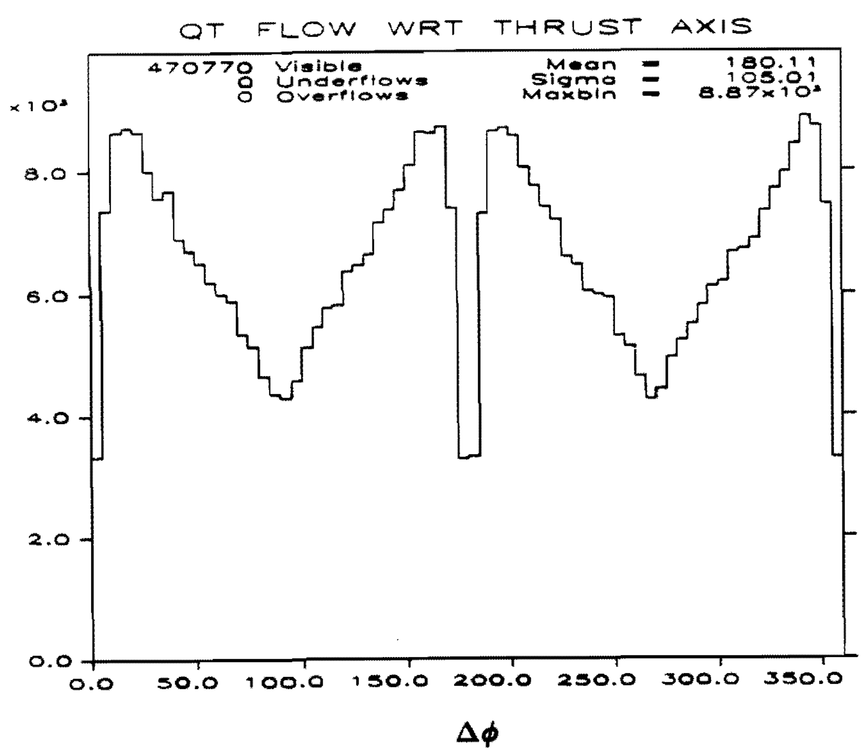

Figure 4.3: Q_t flow with respect to the transverse thrust axis.

Figure 4.3 shows the 'Q_t flow' in the same event sample, where the bins of angle $\Delta\phi^i$ between each tower and the thrust axis are now weighted by Q_t^i. This plot shows that even though the energy depositions at wide angles from the thrust axis are weighted more heavily ($sin\Delta\phi^i \approx 1$) than those along the thrust axis ($sin\Delta\phi^i \approx 0$), towers near the thrust axis make a significant contribution to Q_t .

4.2 Background removal

Before calculating the $< Q_t > / E_t$ curve from the raw data, the obvious backgrounds were removed. In some cases, energy within a given event could be identified as fake, i.e. not associated with the particles from the collision, and this energy could be suppressed. In other cases, entire events were rejected as background. The methods and algorithms developed for identifying fake energy, and for identifying background events are discussed below.

One of the most obtrusive sources of fake energy was random discharges from the central phototubes. Since the energy in each tower is independently measured by two phototubes, these discharges could be identified by checking the energy ratio between the two phototubes. The details of this procedure are described in Ref. [40], but broadly speaking, if the balance of energy between the tubes was outside reasonable limits, the high energy tube was assumed to be from a fake discharge and the measurement from the other tube was used to determine the energy. In this case, the ϕ location of the energy was taken as the center of the tower.

There were two sources of background events in the raw data: 'main ring splash' events and cosmic rays. The main ring is located directly above the CDF detector and during normal data taking it was used for the production of antiprotons. Losses associated with the main ring beam would sometimes deposit large amounts of energy in the top portion of the hadron calorimeters. This was termed 'main ring splash'. Removal of these events offline was accomplished by using information from the TDCs on the hadron calorimeter. An algorithm[42] was developed which summed the energy deposited outside a timing window around the beam crossing. The specific cuts rejected events with more than 8 GeV of energy outside the 35 ns timing window. These time-of-flight cuts were also efficient against cosmic ray muons that emit bremsstrahlung photons in the hadron calorimeters. The parameters of this algorithm were tuned such that the cuts eliminated roughly 90% of the background to high E_t jet data and rejected no events that could have come from real $p\bar{p}$ collisions[42] . Backgrounds that remain include cosmic rays that emit photons in electromagnetic calorimeters which do not have TDCs.

The tracking information from the Central Tracking Chamber was used in the detector corrections discussed below, and in light of this, events without tracks were rejected from the sample; this cut rejected less than 1% of the events. All of the roughly 100 events above E_t of 200 GeV were visually scanned and 2 cosmic ray background events were identified and removed.

The depositions of energy described above resulted in some events that passed the hardware trigger requirements (discussed in Chapter 3) only because of fake energy. Also, since the hardware trigger included the plug and forward electromagnetic calorimeters, the raw event sample contained events which passed the trigger threshold because of energy in those detectors. To create a sample with a uniform trigger, a software program which simulated the central hardware triggers was run on the data after the noise, hot tower and background removal were performed. Events which did not pass the hardware sum E_t cut using only the central and endwall calorimeters were rejected.

After this preliminary data cleanup, the raw $< Q_t > /E_t$ distribution was constructed as follows: a two-dimensional histogram of Q_t versus E_t was filled and $< Q_t >$ was calculated in 20 GeV slices of E_t [1]. The $< Q_t > /E_t$ is the mean Q_t divided by the mean E_t in the 20 Gev slice. Figure 4.4 shows the two-dimensional histogram of Q_t versus E_t

[1]The bin size in the 2-D histogram was 2 Gev in Q_t by 5 Gev in E_t . The center of each Q_t bin was used to calculate the mean Q_t in a given E_t bin. To calculate the mean E_t in a 20 GeV slice, the center of each 5 GeV E_t bin was weighted by the number of events in that bin.

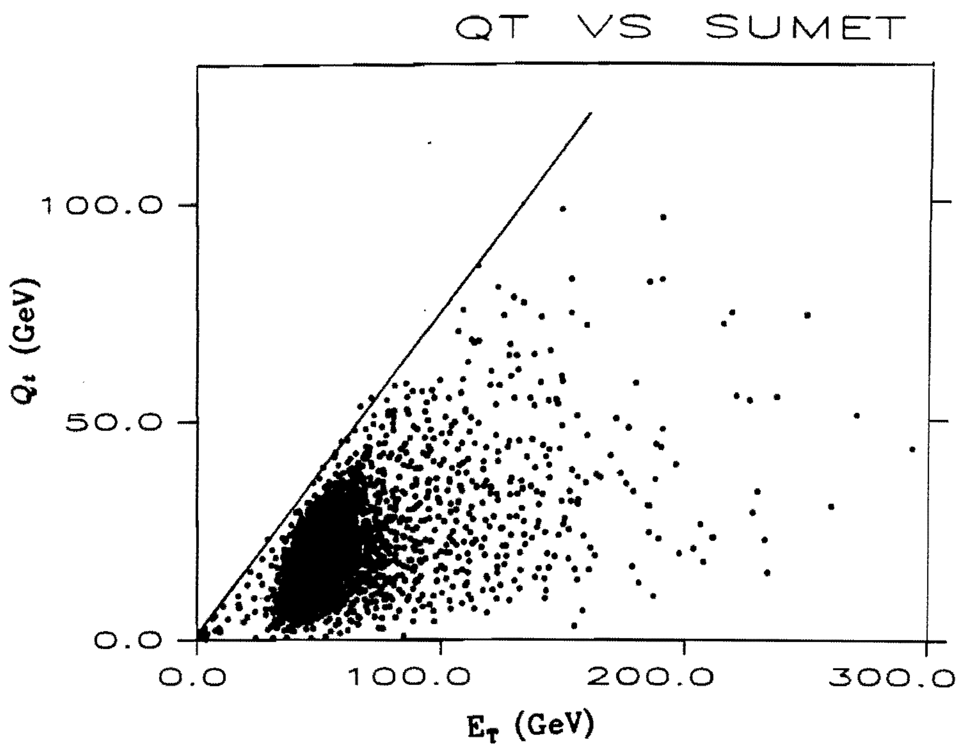

Figure 4.4: Q_t versus E_t for $SUM - ET - 30$ sample after preliminary cleanup. The line indicates the kinematic limit.

for the $SUM - ET - 30$ trigger sample of raw data. The kinematic limit is indicated by the line. Figure 4.5 shows the Q_t distributions in 20 GeV slices of E_t .

The mean and width of the Q_t distributions are observed to increase with increasing energy. Figure 4.6 shows $< Q_t >$ plotted versus E_t , and Fig. 4.7 shows the ratio $< Q_t > /E_t$ plotted as a function of E_t . While $< Q_t >$ rises with increasing E_t in Fig. 4.7, the ratio $< Q_t > /E_t$ decreases from a peak value of 0.36 to about 0.2 over the E_t range of 60 to 200 GeV. The rise and turnover in the $< Q_t > /E_t$ plot below 60 GeV E_t is associated with the turn-on of the trigger efficiency and will be discussed below.

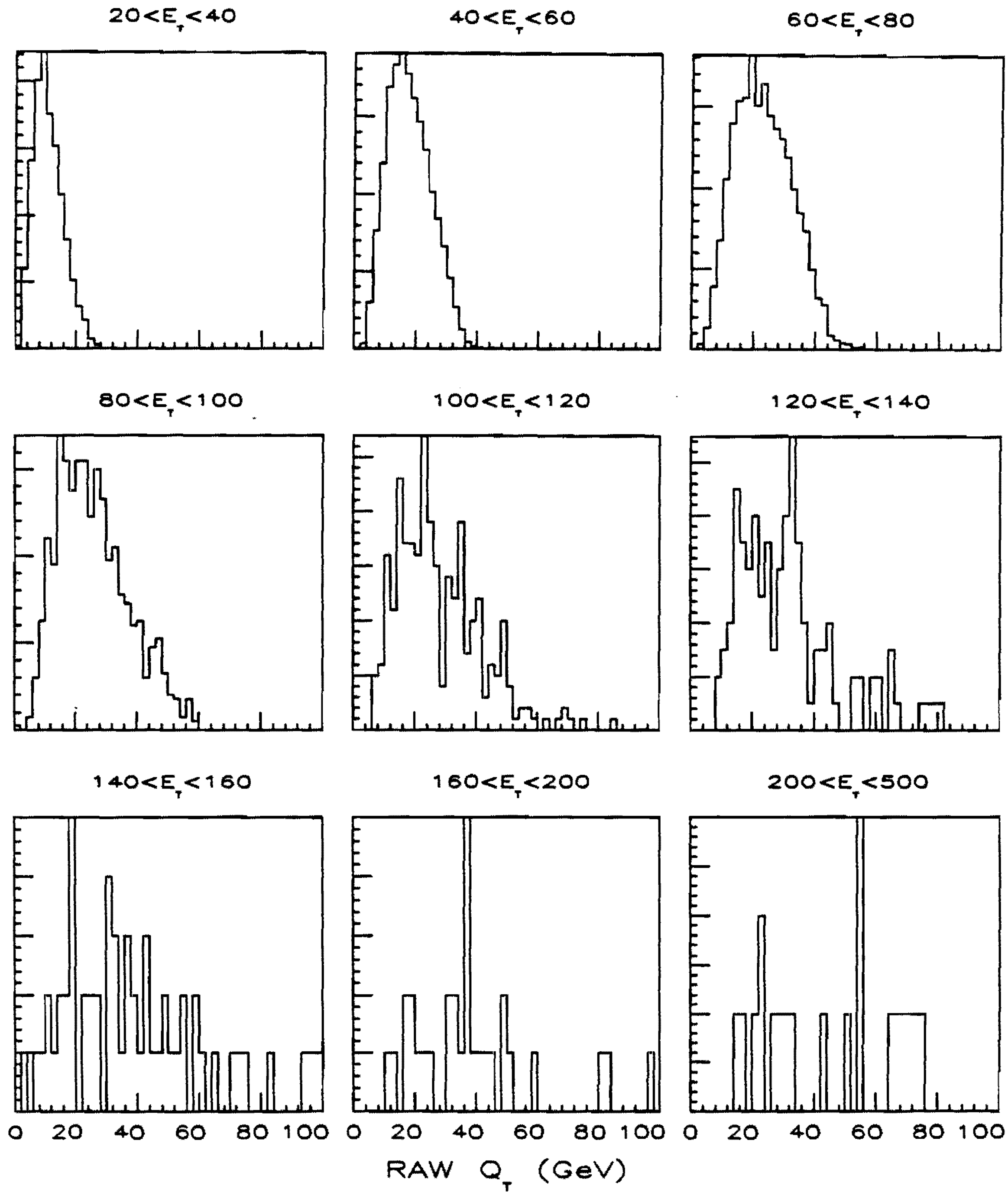

Figure 4.5: Q_t distributions in 20 GeV E_t slices of scatter plot. Verticle scales are normalized to the peak bin in order to emphasize the change in shape with E_t .

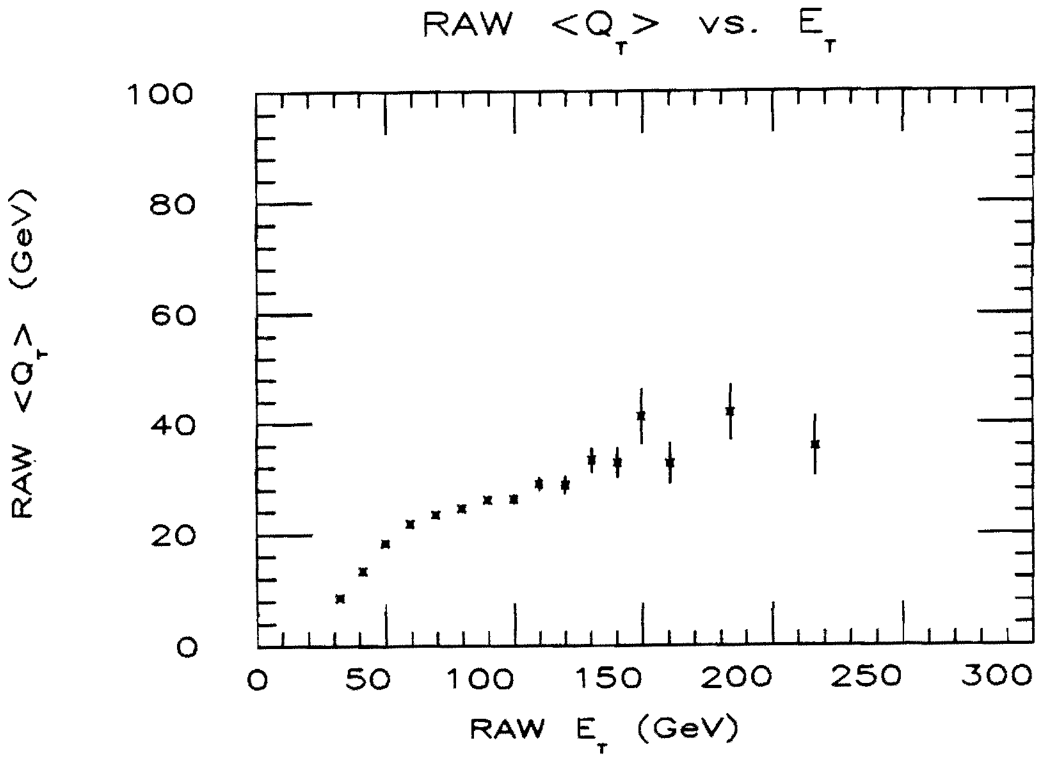

Figure 4.6: $SUM - ET - 30$ **data,** $< Q_t >$ **plotted versus** E_t .

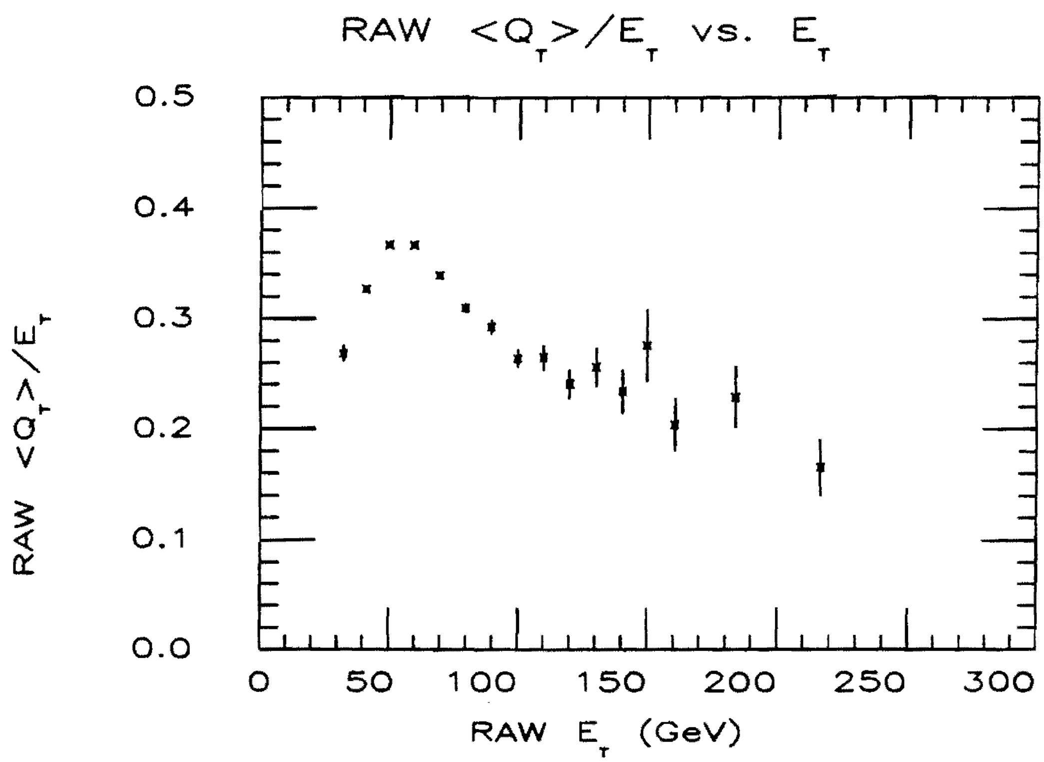

Figure 4.7: $SUM - ET - 30$ **data,** $< Q_t > / E_t$ **versus** E_t .

4.3 Trigger bias and single tower threshold

As described in Chapter 3, four trigger thresholds were used for data collection. These separate samples were combined, as discussed below, in order to maximize the range of E_t over which Q_t was measured. Figure 4.8 shows the number of events for the different trigger samples scaled by their integrated luminosity. Each sample shows a turn-on in the trigger efficiency above the hardware threshold which will be discussed below.

In determining the total E_t of an event, a crucial variable is the tower threshold E^i_{tmin}. When the central E_t was calculated by the trigger hardware, an E^i_{tmin} of 1.0 GeV was applied to each 'trigger tower'[2] as described in Chapter 3. It is important to note that the single tower threshold affects the mixture of soft broad (high Q_t) events and hard collimated (low Q_t) events at a given E_t . The original mixture in the data was determined by the trigger, and thus when a lower single tower threshold is applied to detector towers, the soft events pick up more additional E_t (and Q_t) than the highly collimated 2-jetlike events. The rise in the $< Q_t > /E_t$ curve in Fig. 4.7 is a result of using a single tower threshold of 0.2 GeV which is lower than was used in the trigger. The broad, high Q_t events have gained more E_t from the lower E^i_{tmin} than the collimated, low Q_t events, and thus at the trigger threshold a depletion of high Q_t events is observed.

To minimize corrections based on the Monte Carlo modeling of the low energy single particle spectra, a low single tower of E^i_{tmin} of 0.2 GeV was chosen for the offline analysis. Figure 4.9 shows the $< Q_t > /E_t$ distributions for the separate trigger samples as calculated from detector towers with an E^i_{tmin} of 0.2 GeV. Based on the overlap of the separate trigger samples in these plots, the cuts on raw E_t shown in Table 4.1 result in a sample which is free from the bias associated with the hardware trigger. No overlap was possible for the $SUM-ET-20$ sample however, so a conservative cut above the turn-over of the curve was made.

---

[2] A trigger tower consists of two detector towers ganged together in y.

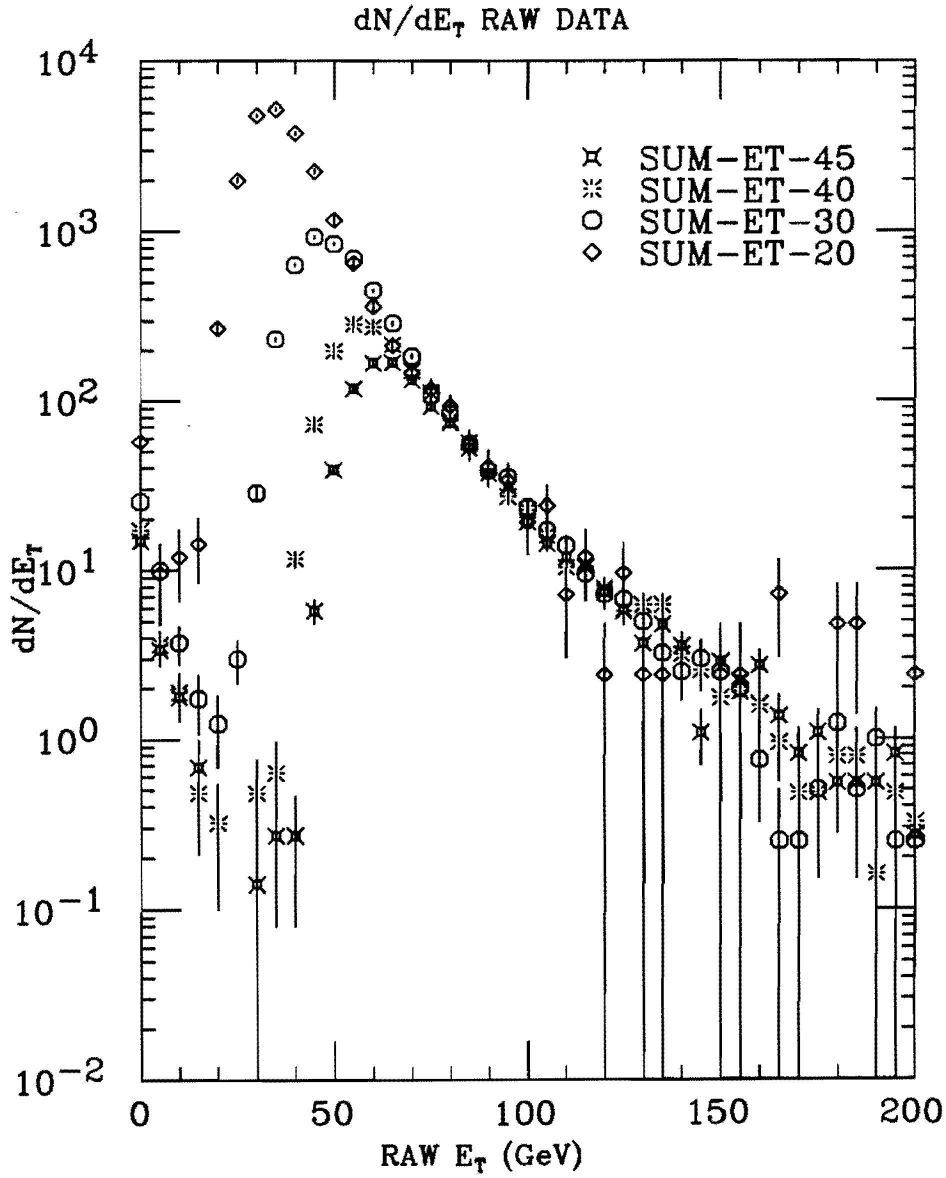

Figure 4.8: Number of events in separate trigger samples scaled by integrated luminosity.

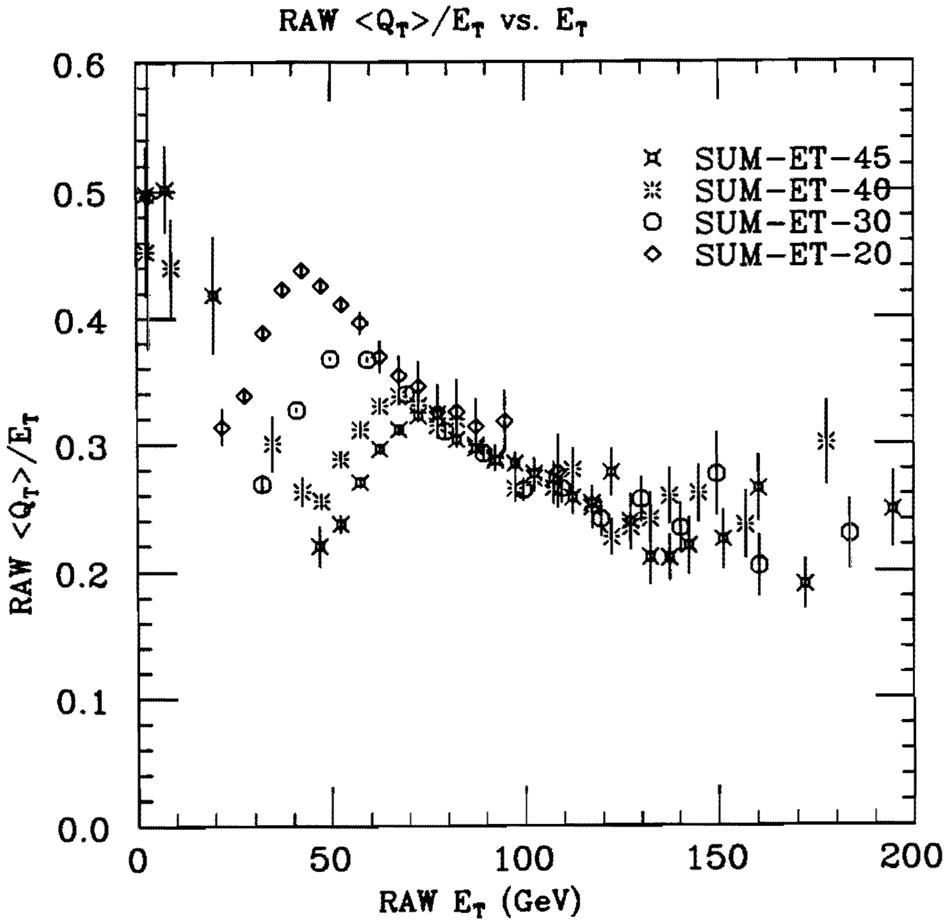

Figure 4.9: $< Q_t > / E_t$ distributions for the separate trigger samples after preliminary data cleanup; $E^i_{tmin} = 0.2$ GeV.

Table 4.1: E_t Cuts on Raw Data

$E_t$cut	Number of Events	Trigger Name
45 GeV	2186	$SUM - ET - 20$
60 GeV	16935	$SUM - ET - 30$
70 GeV	3272	$SUM - ET - 40$
80 GeV	2087	$SUM - ET - 45$

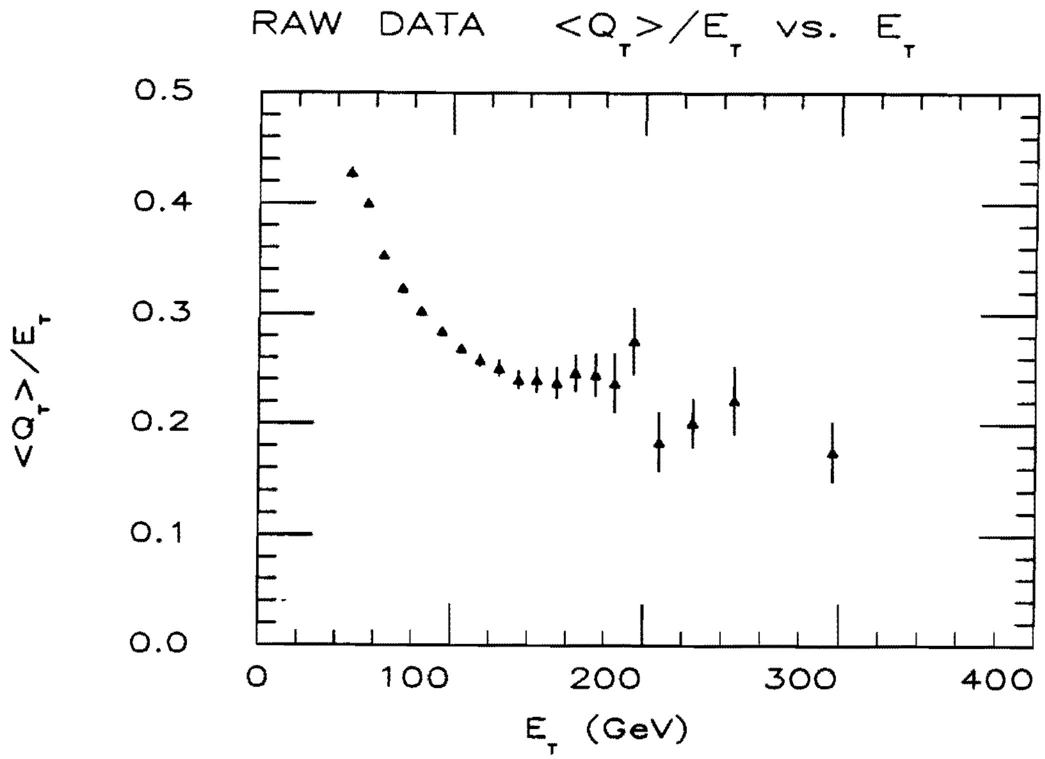

Figure 4.10: $< Q_t > / E_t$ vs E_t for merged trigger samples after preliminary data cleanup.

The distribution of raw $< Q_t > / E_t$ vs E_t for the merged trigger samples is shown in Fig. 4.10 and tabulated in Table 4.2. It shows a decrease in the value of $< Q_t > / E_t$ with increasing E_t . The errors, σ in the Table, represent the statistical uncertainty in determining the mean Q_t in each E_t bin. Although the trigger bias has been removed and the initial cleanup performed, corrections for the effects of the detector properties have not yet been applied. These are discussed below.

4.4 Corrections to the raw distributions

To make comparisons to theoretical predictions it was necessary to determine corrections to the raw data which are associated with the CDF detector, and also for the effects of the underlying event. The detector corrections take into account the ability of the detector to measure accurately the particles produced in each event. A fully-detector-corrected $< Q_t > / E_t$ versus E_t curve would represent what would have been

Table 4.2: Raw Data: $< Q_t > / E_t$ vs. E_t

E_t $[GeV]$	$< Q_t > / E_t$	σ
47.412	0.427	0.0046
56.023	0.400	0.0017
64.436	0.353	0.0017
74.597	0.323	0.0021
84.615	0.302	0.0024
94.754	0.284	0.0034
104.660	0.268	0.0041
114.785	0.257	0.0054
124.666	0.250	0.0071
134.776	0.240	0.0078
144.389	0.240	0.0108
154.826	0.237	0.0138
164.558	0.246	0.0160
175.214	0.245	0.0188
185.227	0.237	0.0264
194.791	0.275	0.0298
207.934	0.184	0.0265
225.108	0.201	0.0217
246.250	0.221	0.0302
296.250	0.174	0.0258

measured if the detector were perfect and could detect the correct energy and position of all particles in the collision.

The approach taken for deriving the detector corrections was to use all the available information from the data, and then to rely on the Monte Carlo simulation for residual corrections. For example, the charged tracking information was used to correct for the nonlinear response of hadron calorimeters; the residual detector corrections include effects such as energy losses in cracks and energy lost to particles that curl completely in the magnetic field, never reaching the calorimeter (see below). This approach was adopted to minimize dependence of the detector corrections on the Monte Carlo model of the events and hadronization. For any choice of single tower threshold, the residual detector corrections will be affected by how much energy is lost below the single tower threshold and how much is lost to particles that curl in the magnetic field. The use of the charged tracking information and the low single tower threshold minimize the reliance on the Monte Carlo single particle P_t spectrum by maximizing the use of the charged particle P_t spectrum in the data.

4.4.1 Calorimeter Nonlinearity Corrections

The major detector oriented correction comes from the nonlinear response of the central calorimeters to low energy hadrons. One consequence of the nonlinearity was that the hard part of the event (typically the energy along the jet axis) is measured more accurately than the soft, wide angle emissions. No calorimeter test beam data was avaliable for particles below 10 GeV, but by using the central tracking information in the Minimum Bias Data sample, Behrends et al.[43] measured the average response of the central calorimeter, electromagnetic + hadronic, for isolated low momentum tracks. Their measurements apply to charged particles with P_t above 0.4 GeV. Below this P_t threshold charged particles curl in the 1.5 Tesla magnetic field and never reach the calorimeter face. Their procedure involved summing the energy in a 3×3 block of towers (to include the effects of shower spreading) and making strict isolation requirements to

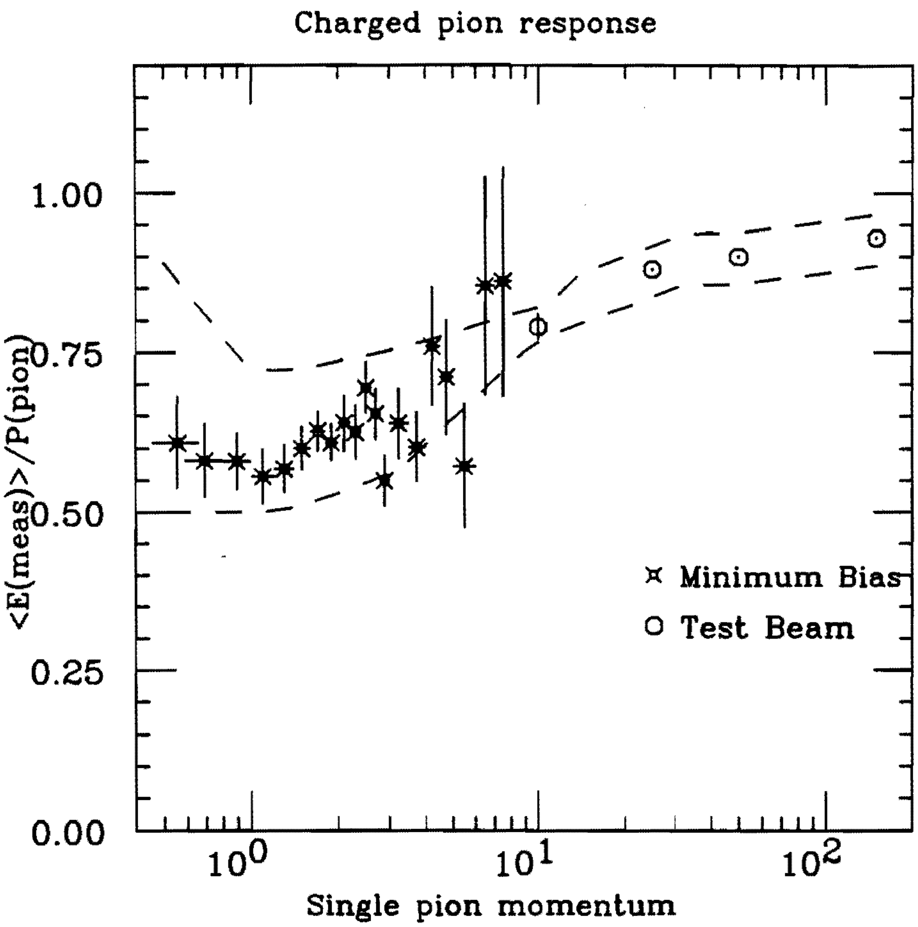

Figure 4.11: Average Response of the Central Calorimeter to Charged Particles. Below 10 GeV Minimum Bias isolated track data was used. Points above 10 GeV were derived from test beam studies. The curves represent the estimated size of the uncertainty in the determination of the average response.

minimize contributions from other particles. An estimate of the contribution from π^0's was made and was subtracted in the determination of the average response.

Figure 4.11 shows the average response of the central calorimeter to charged particles below 10 GeV together with test beam results for particles above 10 GeV. These results were used to make an average correction for the nonlinear calorimeter response. The calorimeter nonlinear correction was performed by looping over the tracks in each event, projecting the track through the magnetic field to the face of the calorimeter and then correcting the struck tower for the difference between the original track momentum and the average calorimeter response to a particle of that momentum.

4.4.2 Calorimeter Pedestal Corrections

As discussed in Chapter 3, the central calorimeters were monitored daily such that a contant calibration would be maintained. This was accomplished by adjusting the pedestal level of each calorimeter. It was later noticed that during the run a significant shift in the average energy density in the minimum bias events occurred. A small, but measurable difference in $< Q_t > /E_t$ was also observed. Investigation showed an overall scale change was not the problem[44], but rather an overall shift in the pedestals. In addition, recent comparisons of the 1987 data with data taken in 1989 indicate a difference in the pedestal level of the central calorimeters[45]. Although the energy density study of the minimum bias data suggested a sudden shift, no explaination for a sudden shift could be found. Rather, after the run it was determined that an asymmetric threshold circuit for the pedestal determination probably caused a gradual shift over the entire run. In principal, the calibration of the detectors was maintained by measuring the pedestal levels and correcting them if the level were off by more than a fixed value ($\approx$ 60 MeV). As it turned out, pedestals were corrected if they were too high by more that 60 MeV, but they could go low by roughly 240 Mev before they would be readjusted. During the course of the run, it is believed that all the pedestals gradually shifted low and were not corrected because of this asymmtery in the threshold circuit.

To study and correct for this effect the $SUM - ET - 30$ data was divided into two parts: data taken before the shift observed in the minimum bias data, and data taken after the shift. Figure 4.12a and b show the mean number of towers above a single tower threshold of 0.2 GeV before and after the pedestal shift occurred. The mean number of towers in the events before the shift is significantly higher. By comparing the tower energy spectra it was determined that a constant pedestal shift of 80 MeV on the electromagnetic and 30 Mev on the hadronic calorimeters had occurred. Since

Table 4.3: E_t Cuts on Track Corrected Data

E_t	Number of Events	Trigger Name
70 GeV	7093	SUM-ET-20
85 GeV	33168	SUM-ET-30
100 GeV	3222	SUM-ET-40
120 GeV	1707	SUM-ET-45

it was impossible to add energy to data taken after the shift, these constant amounts were subtracted from every tower that had energy (negative values are set to zero) for all events taken before the shift was observed. Figure 4.12c shows the data taken before the shift after the pedestal correction had been applied. The corrected mean number of towers is in much better agreement with the data taken after the shift (shown in Fig. 4.12b). In effect, this correction is moving the data further from where it is now believed the correct pedestal level to have been. This will be treated in the systematic uncertainty attributed to the knowledge of the pedestals as discussed below.

Performing tracking and pedestal corrections is analogous to changing the single tower threshold, in that events with mainly low energy particles are going to be affected more by these corrections. Figure 4.13 shows the 'track corrected' (this includes track and pedestal corrections) plots of $< Q_t > /E_t$ for the separate trigger samples. Again, based on the locations of the overlaps for the separate triggers, the cuts shown in Table 4.3 were derived for track corrected E_t . Note that for the $SUM-ET-20$ and $SUM-ET-30$ samples, the cuts on raw E_t were relaxed to 30 and 50 GeV respectively, to allow the track corrected E_t cut to be as low as possible. The $SUM-ET-40$ and $SUM-ET-45$ data which passed the track corrected E_t cuts are a subset of the data which passed the raw E_t cuts listed in Table 4.1.

Figure 4.14 shows the raw $< Q_t > /E_t$ curve compared to the 'track corrected' curve. The nonlinear and pedestal corrections have most of their effect on the low energy end of the curve; E_t in seen to increase by about 15 GeV and at 100 GeV E_t the $< Q_t > /E_t$ is raised by roughly 20%. The track corrected data are tabulated in Table 4.4.

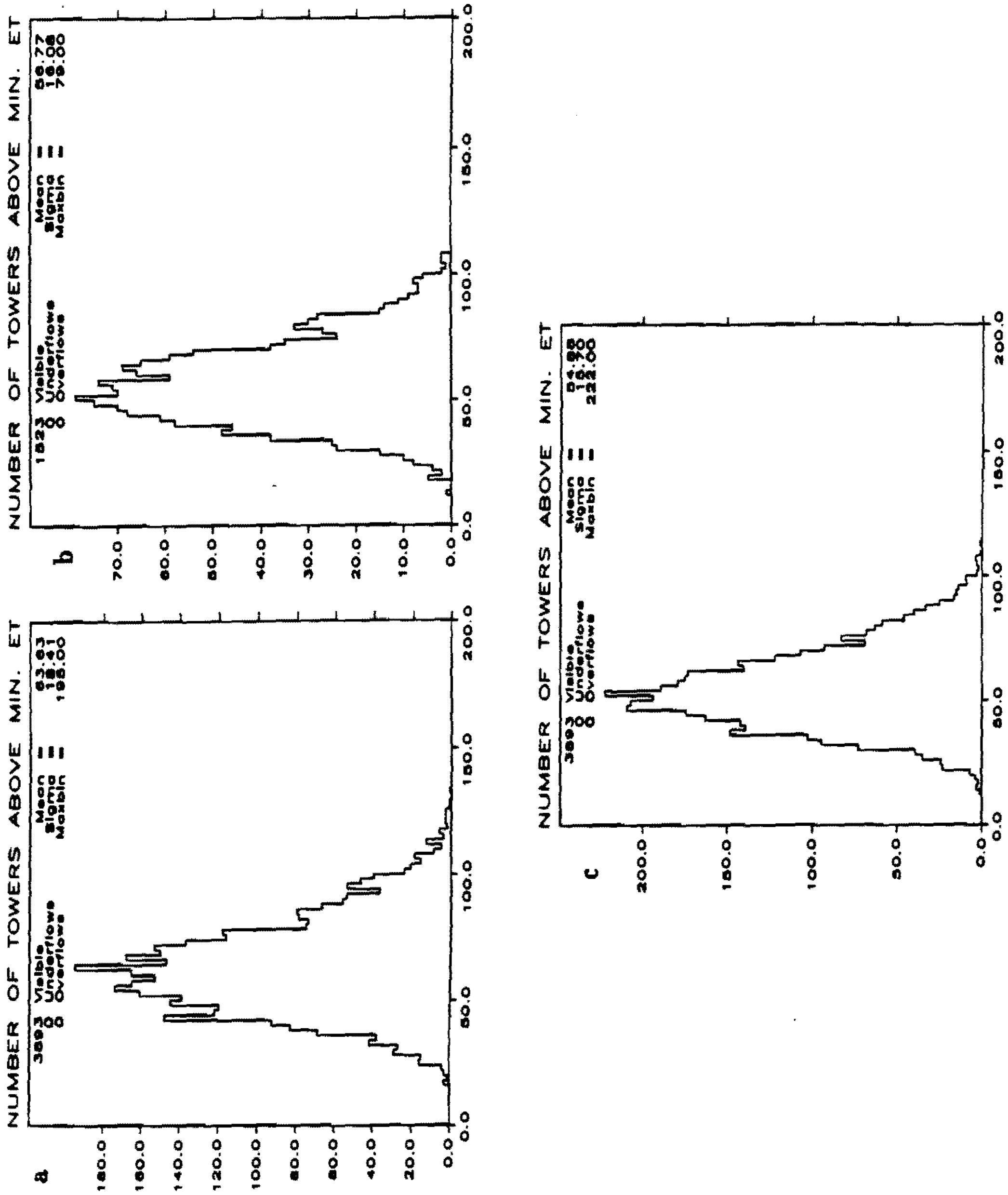

Figure 4.12: (a)Mean number of towers E^i_{tmin} of 0.2 GeV, pre-shift data; (b) Mean number of towers E^i_{tmin} of 0.2 GeV post-shift data; (c) Mean number of towers E^i_{tmin} of 0.2 GeV corrected pre-shift data.

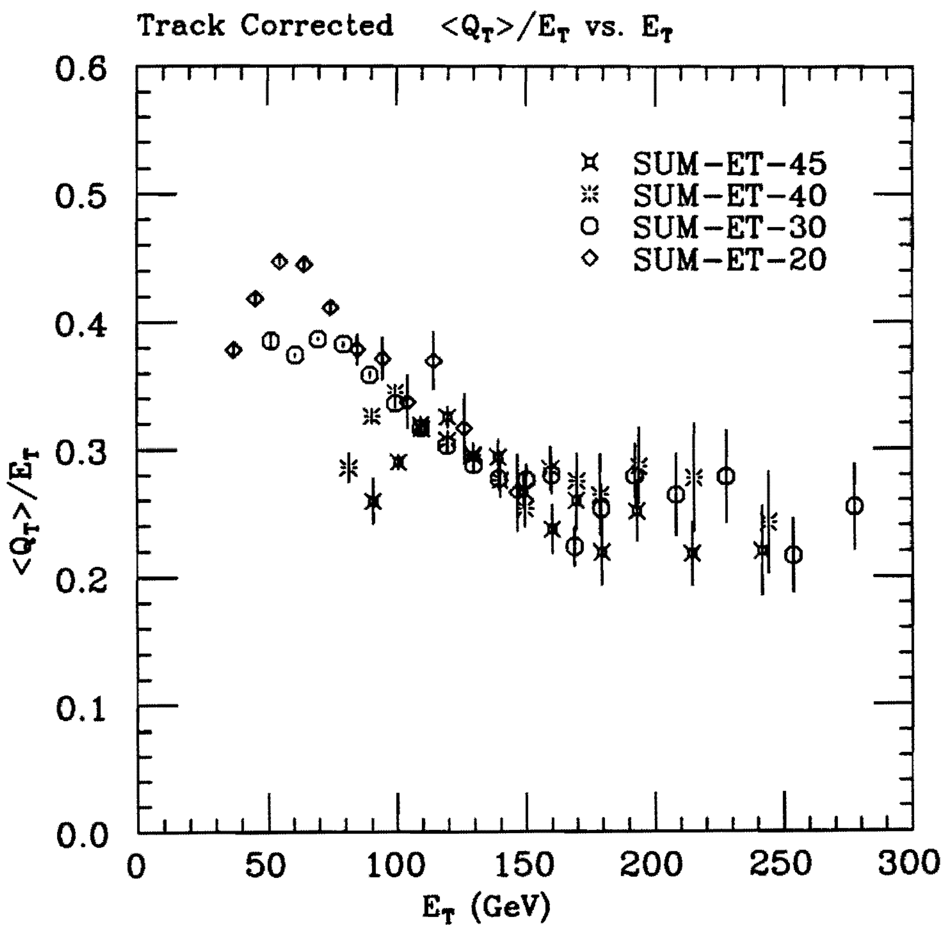

Figure 4.13: 'Track corrected' $< Q_t > / E_t$ for the separate trigger samples.

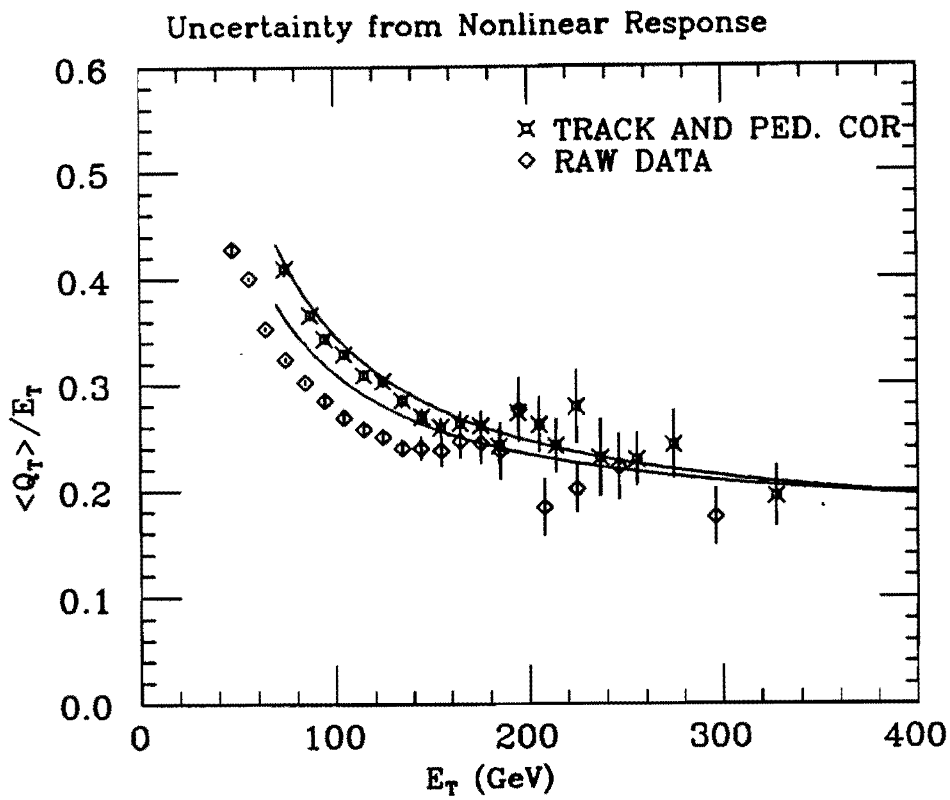

Figure 4.14: Raw $< Q_t > /E_t$ curve compared to the 'track corrected' curve; merged trigger samples. Solid lines indicate the range of uncertainty in $< Q_t > /E_t$ from the uncertainty in the nonlinear response.

Table 4.4: $< Q_t > /E_t$ vs. E_t Track Corrected Data

E_t [GeV]	$< Q_t > /E_t$	σ
74.474	0.4099	0.00654
87.266	0.3667	0.00325
94.532	0.3449	0.00292
104.644	0.3306	0.00322
114.838	0.3090	0.00429
124.737	0.3058	0.00459
134.707	0.2843	0.00565
144.709	0.2720	0.00688
154.538	0.2638	0.00847
164.643	0.2656	0.00953
175.188	0.2587	0.01274
184.821	0.2270	0.01611
194.815	0.2838	0.01744
205.167	0.2681	0.02596
213.534	0.2618	0.03103
224.231	0.2676	0.02882
236.750	0.2298	0.03101
255.833	0.2265	0.02370
274.167	0.2312	0.03455
321.731	0.2068	0.02508

To estimate the systematic uncertainty in the tracking correction, the nonlinear response was varied to the upper and lower limits of its uncertainty (indicated by the dashed lines in Fig. 4.11). The raw data were corrected using these low and high response curves. The range of track corrected $< Q_t > /E_t$ from the uncertainty in the nonlinear response is shown in Fig. 4.14.

In the case of the pedestal shifts, the difference between the $< Q_t > /E_t$ curve before and after the pedestal shift is taken as a measure of the effect of a roughly 100 MeV shift in the pedestals. Since the data had to be corrected away from what is believed to be the true distribution, the upper limit on the uncertainty in the $< Q_t > /E_t$ curve will be taken as twice the change. Note that pedestals which are too low correspond to measuring too little energy in the detector and result in a lower $< Q_t > /E_t$. If it were possible to add this missed energy to the events the $< Q_t > /E_t$ curve would rise. Since all evidence indicates that the pedestals were too low at the end of the run, the lower limit on $< Q_t > /E_t$ uncertainty from the pedestals will be taken as half the difference. The bands shown in Fig. 4.15 indicate the size of the systematic uncertainty in the 'track corrected' $< Q_t > /E_t$ curve from the uncertainty in the pedestals.

4.4.3 Residual Detector Corrections

The second category of detector corrections includes the effects of losses due to dead material, cracks between calorimeter modules, single tower threshold, curling particles, and neutrinos. The combination of these effects was measured through the use of a software detector simulation [46]. An event generator (ISAJET[26]) was used to provide jet events for input to the detector simulation program. A description of the event generation and simulation for the residual detector corrections is given in Appendix C.

Residual detector corrections were derived for both E_t and $< Q_t > /E_t$ since the detector properties can have different effects on these quantities (i.e. the low energy particles which dominate at wide angles from the jets may be influenced by the single tower threshold more than the particles along the jet axis). Correction factors for

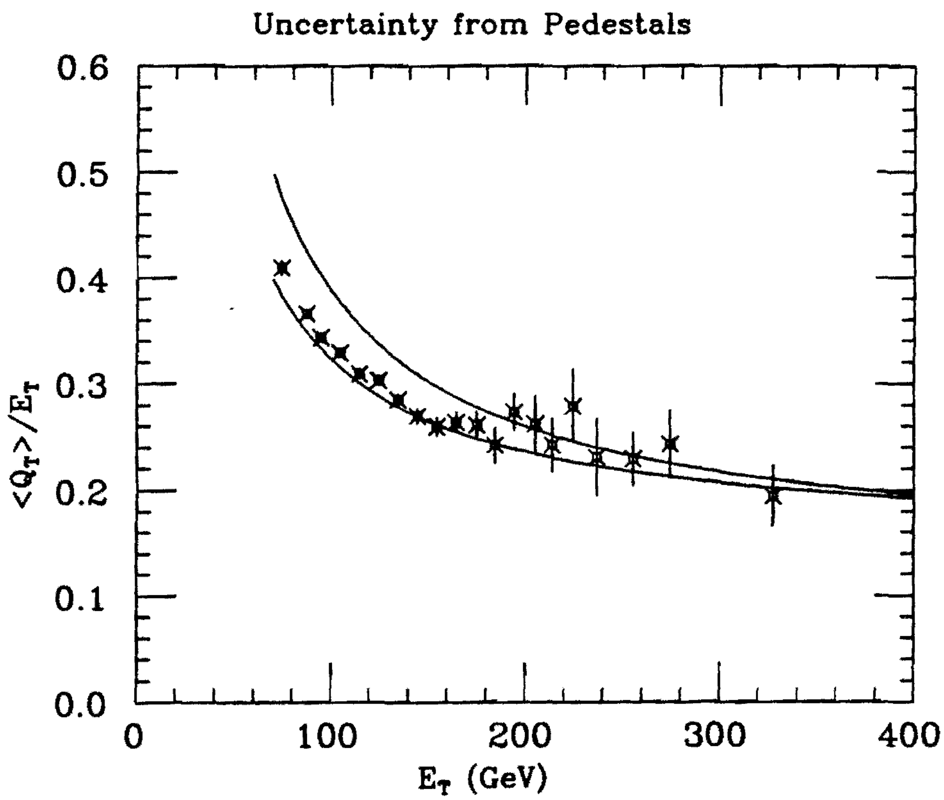

Figure 4.15: Track corrected $< Q_t > / E_t$. Solid lines indicate total uncertainty due to uncertainty in the pedestals.

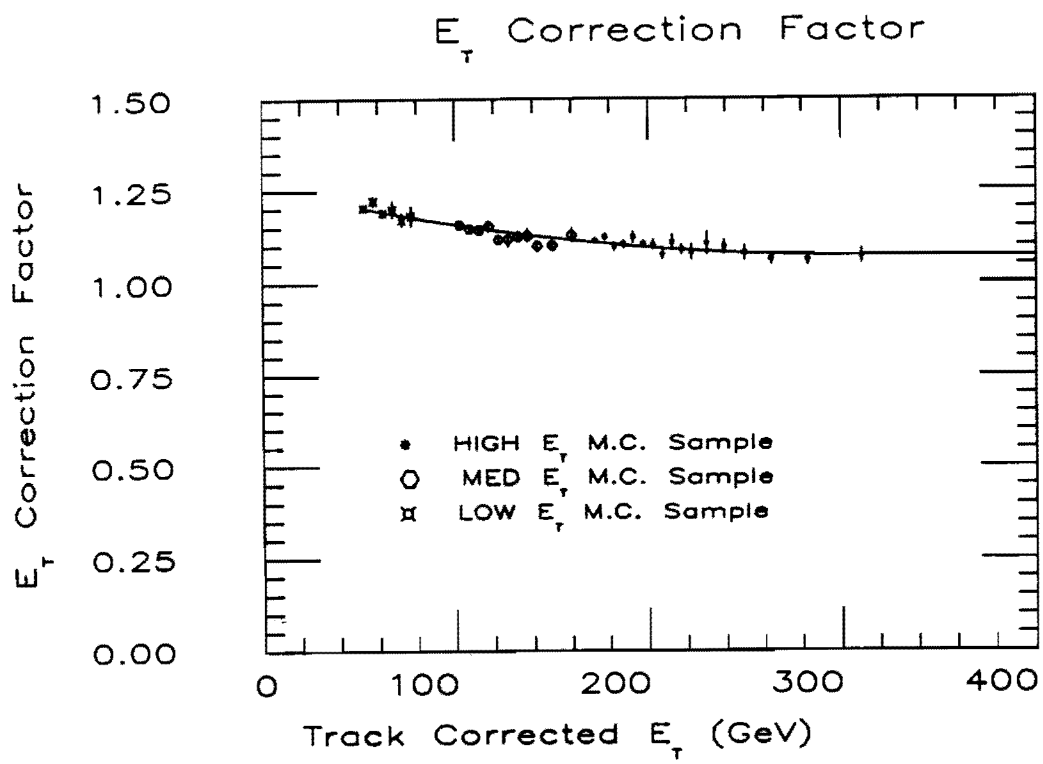

Figure 4.16: The mean E_t correction factor as a function of track corrected E_t .

E_t were derived by comparing the simulated and track corrected E_t to the 'particle-level'[3]E_t . The mean E_t correction factor as a function of track corrected E_t is shown in Fig. 4.16.

Corrections for $< Q_t > /E_t$ were derived in a similar manner. The energy dependence of the Q_t/E_t correction was accounted for by measuring the correction factors in three slices of track corrected E_t which spanned the range of the data. Figure 4.17 shows the Q_t/E_t correction factors for slices of track corrected E_t of 50-80 GeV, 100-140 GeV and 180-220 GeV. Fits to these points are indicated by the lines. Interpolation between the curves based on the track corrected E_t determined the Q_t/E_t correction factor at any intermediate E_t . The detector corrected $< Q_t > /E_t$ curve is formed

[3]As defined in Appendix C, 'particle level' refers to what would have been measured if the detector could correctly measure the energy from all the particles produced from the haronisation of the partons and from the underlying event.

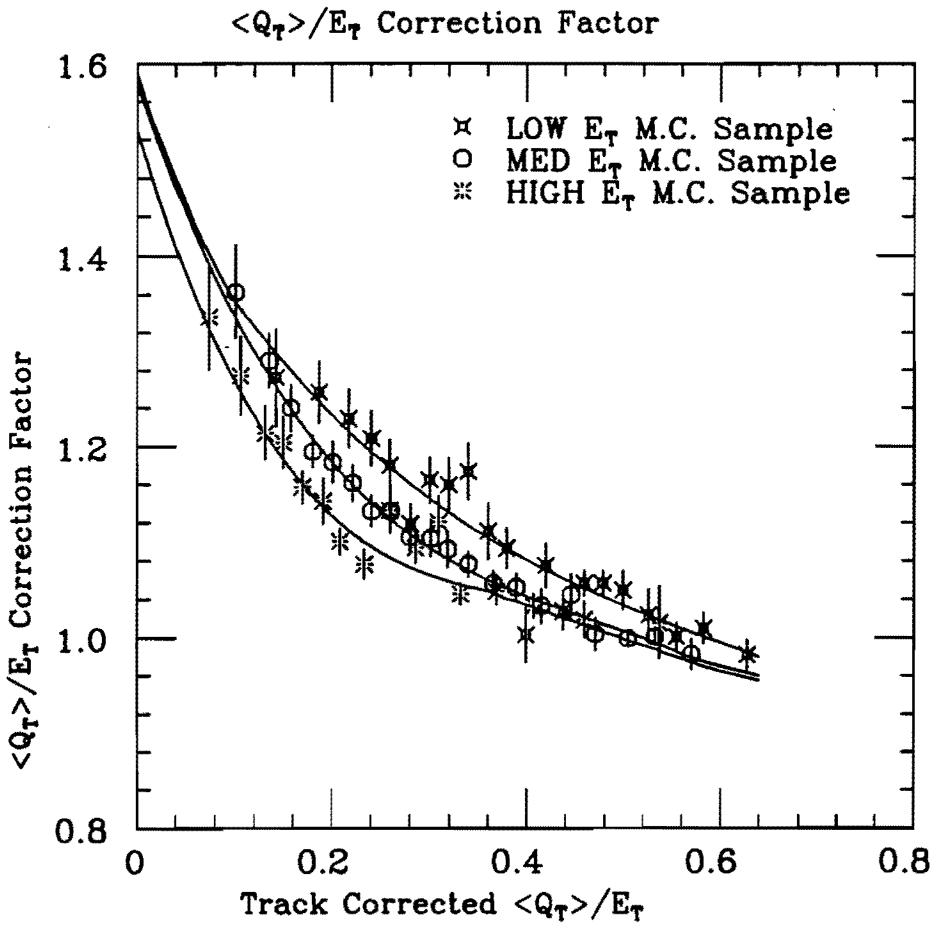

Figure 4.17: Q_t/E_t correction factors for slices of track corrected E_t of 50-80 GeV, 100-140 GeV and 180-220 GeV. Fits to these points are indicated by the lines.

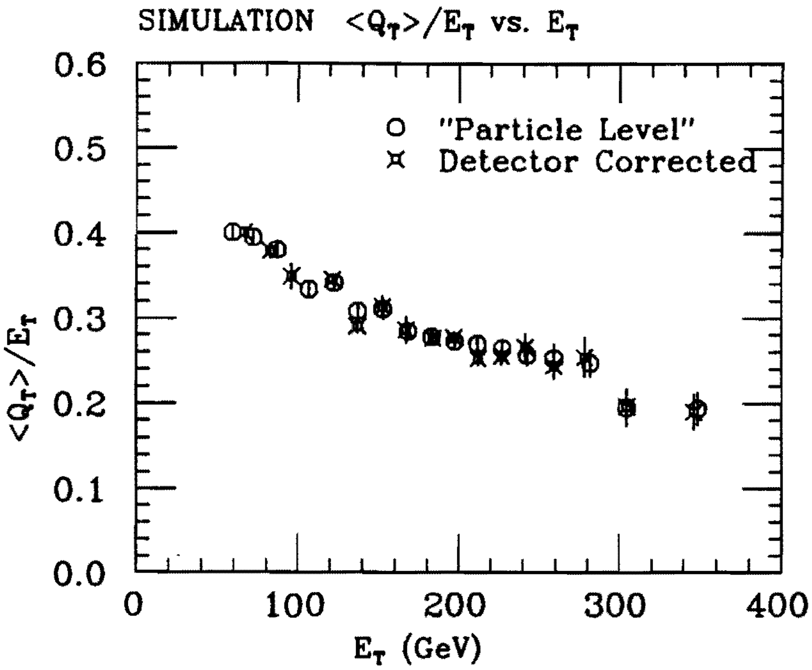

Figure 4.18: Fully detector corrected $< Q_t > /E_t$ and the $< Q_t > /E_t$ from the 'particle level' (hadronized partons + underlying event).

by applying the correction factors event by event based on the measured 'track corrected' E_t and Q_t/E_t in each event. As a check for self-consistency, the detector corrections were applied to the simulated, track corrected sample; Figure 4.18 shows that there is good agreement between the fully detector corrected $< Q_t > /E_t$ curve and the $< Q_t > /E_t$ curve from the 'particle level'.

Figure 4.19 shows the fully detector corrected result compared to the track corrected curve. As described in Chapter 2, there is a large theoretical uncertainty associated with the effects of hadronization. With the method described above, the detector corrections do not attempt to remove these effects and thus should be relativly insensitive differences to the specific fragmentation functions[4]. The extent to which different

[4]Traditionally, the term 'fragmentation function' is used to describe the parameterisation of the function which converts a single parton into hadrons, i.e. it describes the hadronisation of a parton. This usage will be continued here.

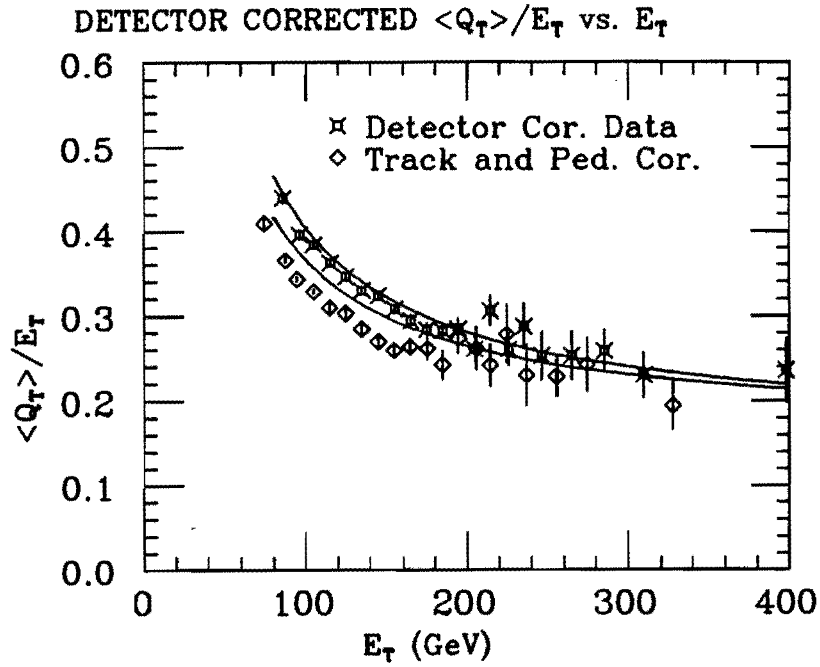

Figure 4.19: Detector corrected $< Q_t > /E_t$ vs E_t compared to track corrected result. Solid lines indicate uncertainty from nonlinear response.

fragmentation functions effect the detector corrections is included as a systematic uncertainty and is discussed below.

4.4.4 Systematic Uncertainty in Detector Corrections

Each detector correction has associated uncertainties. The propagation of these uncertainties to the detector corrected $< Q_t > /E_t$ curve is discussed here. The uncertainty in the tracking correction was found by varying the nonlinear response to its lower and upper limits. The corresponding shift in the detector corrected $< Q_t > /E_t$ versus E_t provided a direct measure of the lower and upper limits of the uncertainty from this correction. The solid lines in Fig. 4.19 show the range around the detector corrected $< Q_t > /E_t$ which results from uncertainty in the nonlinear response. Similarly, the detector corrected uncertainty from the pedestal shift was evaluated by measuring the

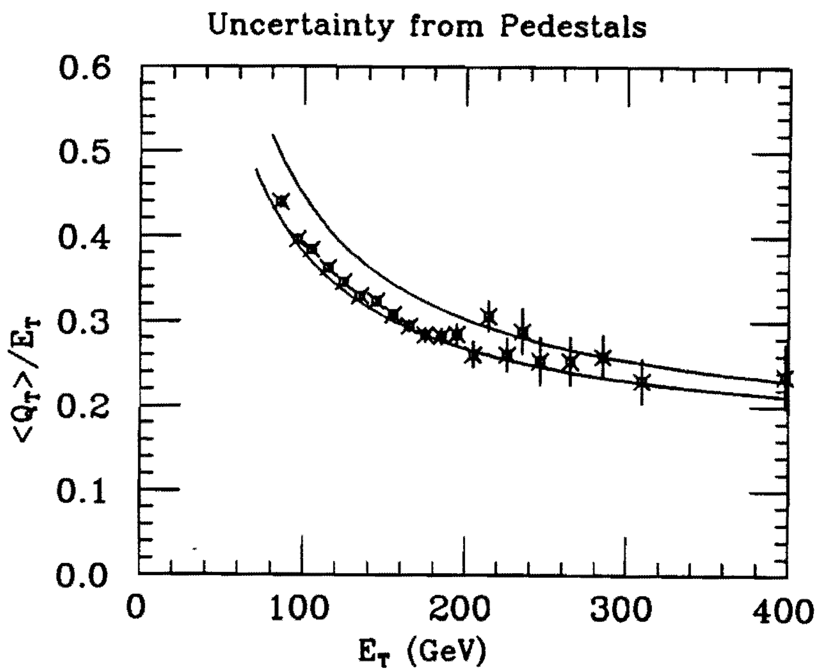

Figure 4.20: Detector corrected $< Q_t > /E_t$ vs E_t compared to track corrected result. Solid lines indicate uncertainty due to uncertainty in the pedestals.

difference the $< Q_t > /E_t$ curve with and without the residual pedestal shift correction. The curves in Fig. 4.20 show the range of uncertainty in the detector corrected $< Q_t > /E_t$ from the pedestal shift.

Since the residual detector corrections incorporate many effects, the estimate of the the uncertainty in the correction is separated into its main contributions: our knowledge of the calorimeter resolution, and possible effects of hadronization. Our knowledge of the detector energy resolution was derived in part from test beam measurements and in part from di-jet balancing studies. The best estimate of the calorimeter resolutions are used in the simulation, and these, combined with the falling E_t spectrum generated in the Monte Carlo sample, produced E_t distributions which include the effect of resolution smearing. Since the detector corrections were derived from these 'smeared' distributions, they include corrections for smearing. To determine the extent to which our knowledge of the calorimeter resolution affects the detector corrections, another set of detector correction factors for 'unsmeared' distributions were derived. This was achieved by plotting the correction factors as a function of the 'particle level' E_t , which had not been smeared by the detector resolution, instead of the track corrected E_t . The difference between the unsmeared and smeared correction factors varied from 2% to 4% over the E_t range of the data. The 'unsmeared' correction factors corresponded to having an energy resolution of $0\%/\sqrt{E}$ while the 'smeared' distrubutions correspond to the best estimate of the jet energy resolution[47], $120\%/\sqrt{E}$. Half of the difference between the 'smeared' and 'unsmeared' correction factors was taken as the uncertainty in the correction factors from the uncertainty in the resolution.

Although we have attempted to isolate the detector corrections from the specific details of the fragmentation function used in the Monte Carlo, the choice of fragmentation functions could affect such things as the amount of energy lost under the single tower threshold. The ISAJET fragmentation function has the form

$$f(z) = 1 - a + a(b+1)(1-z)^b,$$

where z is the fraction of the parton momentum parallel to the parton direction which is carried carried by the hadron. To estimate the size of the dependence on the Monte Carlo fragmentation functions, the parameters of the fragmentation function were varied. Table 4.5 shows the upper, lower, and best values of the fragmentation parameters as determined by fits to the jet data[47]. The shift in the Q_t/E_t correction factor was

Table 4.5: Fragmentation Parameters

a	b	
0.96	3.0	ISAJET default
0.88	2.0	Tuned to CDF Jet data
0.57	2.0	Tasso

measured in two slices of E_t , one centered at 105 GeV track-corrected E_t and one at 250 GeV track-corrected E_t in order to span the data. A 0.015 shift in the value of the correction factor was observed in the low E_t slice and a 0.010 shift was observed

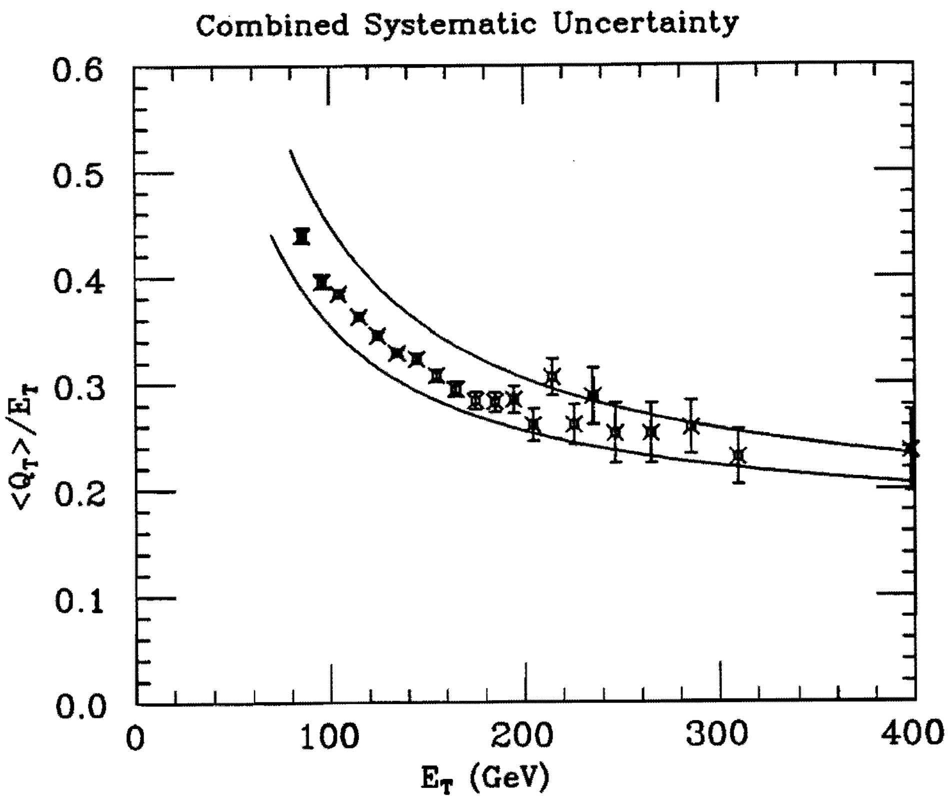

Figure 4.21: Detector corrected $< Q_t > /E_t$ vs. E_t . Solid lines indicate the size of the total systematic uncertainty in detector corrected result.

in the high E_t slice. A linear interpolation between these points is taken as the energy dependent uncertainty in the detector correction factors due to the fragmentation functions.

The uncertainty in the correction factors was combined with the uncertainty from the nonlinear response and with the uncertainty from the pedestals. Figure 4.21 shows the detector corrected data where the solid lines indicate size of these combined uncertainties.

4.5 Underlying Event

The typical model for high E_t QCD events is a hard collision plus an 'underlying event' associated with the spectator partons. The energy from the underlying event is taken to be uncorrelated with the hard process and thus will occur at wide angles to the thrust axis, as well as along the thrust axis. To make the Monte Carlo events as similar to the data as possible, an underlying event was generated and simulated along with the jet events. But rather than rely on the details of the Monte Carlo model of the underlying event, we chose to use an estimate of the underlying event energy from the data. Below, measurement of the average energy density of the underlying event is discussed, along with how it was used to perform an average subtraction for the effects of the underlying event in the determination of $< Q_t > /E_t$ and E_t .

The simplest model for the underlying event was an isotropic distribution of energy in $y-\phi$ space of the central detector. To study the energy density, events with two hard clusters ($E_t \geq 20$ GeV each) were selected and the energy perpendicular in azimuth to the jet axis was measured (for two jet events the jet axis corresponds to the transverse thrust axis). This procedure is described in detail in Ref. [48]. Figure 4.22 shows the E_t flow with respect to the thrust axis for di-jet events. For each event, the E_t deposited within the 20° bands perpendicular to the transverse thrust axis (indicated in Figure 4.22) was summed over the entire rapidity of the central detector ($-1.1 < y < 1.1$). The average E_t density of the 'underlying event' was then obtained by dividing the average E_t measured in the bands by the total area of the bands in $y - \phi$ space, 0.70 radians by 2.2 units rapidity.

In addition to requiring two hard clusters, other cuts for selecting di-jet events were investigated. Table 4.6 contains results for a variety of di-jet cuts. As mentioned earlier, all of the events were required to have at least two clusters each with more than 20 GeV E_t . In the table, Et_{3rd} refers to the maximum allowed E_t for any other cluster in the event, and $\Delta\phi$ refers a back-to-back requirement in ϕ , i.e. $\Delta\phi$ of 10 means the two highest energy clusters in the event were required to be back-to-back within 10° in ϕ .

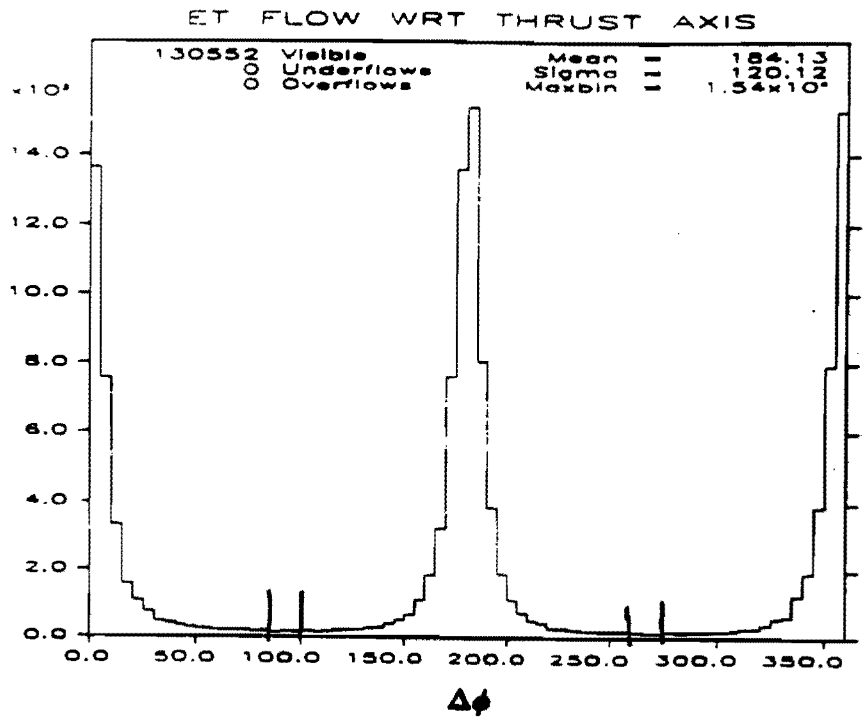

Figure 4.22: The E_t flow with respect to the thrust axis for di-jet events.

The specific cuts used for selecting clean di-jet events were strongly correlated with the the amount of energy measured in the 'off-axis' bands. The difficulty in defining the cuts comes from the inability to distinguish high fluctuations in the underlying event from clusters associated with the hard scattering (i.e. multijet events). After studying the effect of the cuts and comparing with the frequency of clusters in the Minimum Bias data, it was found that the optimum cuts required that the two leading clusters had at least 20 GeV each, that they were back to back in ϕ within 10°, and that any third cluster in the event had E_t less than 15 GeV. The off-axis E_t in this sample is shown in Fig. 4.23.

For the best set of cuts, the mean E_t in the off-axis bands was 1.11 GeV, corresponding to an E_t density in y-ϕ space of 0.72 GeV/radian-unit rapidity. By taking a systematic uncertainty of $\pm$ 0.2 GeV on the E_t density, the range of densities resulting from varying the cuts was covered. The statistical error on the determination of the

Table 4.6: Two Central Jet Sample

$\Delta\phi$	Et_{3rd}	Events	E_t [GeV] Band	E_t Density	E[GeV] Band	E Density
–	–	10046	1.43	0.93	1.91	1.24
10	–	4800	1.18	0.77	1.60	1.04
10	15	4641	1.11	0.72	1.52	0.99
10	5	3650	0.89	0.58	1.24	0.81
20	–	7197	1.23	0.80	1.66	1.08
20	15	6866	1.15	0.75	1.57	1.02
20	5	5153	0.90	0.59	1.25	0.81

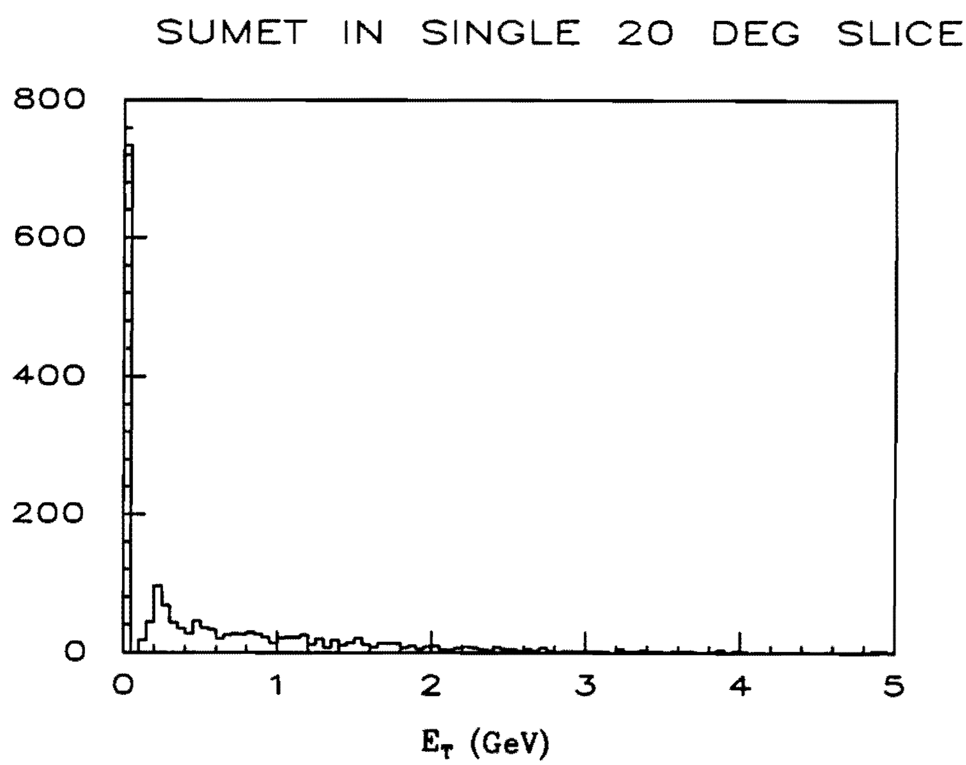

Figure 4.23: The off-axis E_t in the di-jet sample.

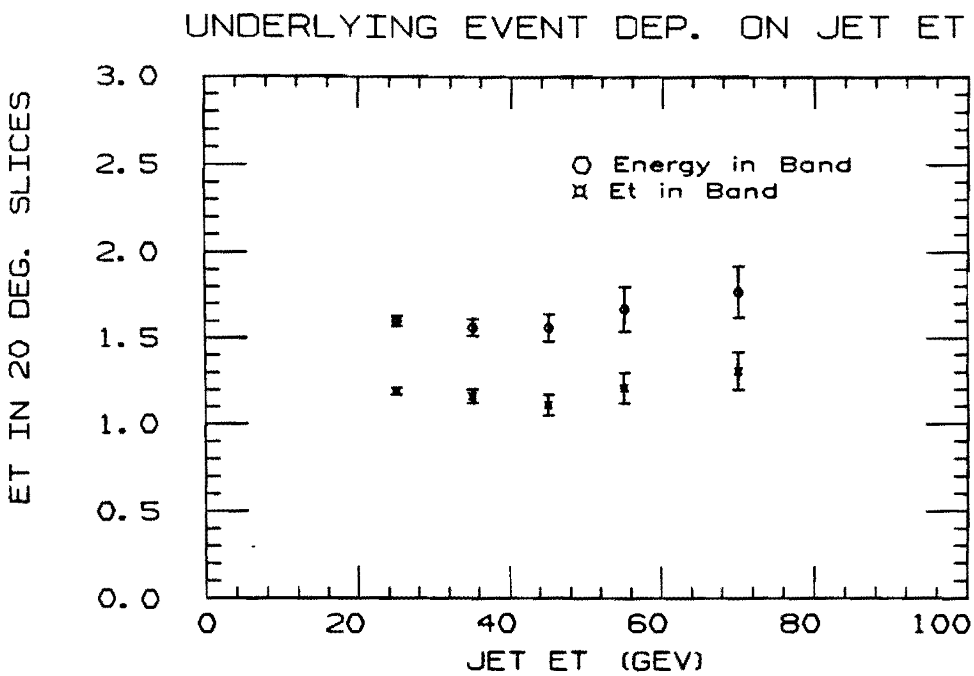

Figure 4.24: Underlying event E_t vs. average cluster E_t ; Di-jet cuts required two clusters of $E_t \geq 20$ GeV and that these clusters be back-to-back within 10° in ϕ .

Table 4.7: Central-Plug Sample

$\Delta\phi$	Et_{3rd}	Events	E_t [GeV] Band	E_t Density	E[GeV] Band	E Density
20	15	160	1.16±0.09	0.76±0.06	1.61±0.13	1.05±0.08
20	5	53	0.85±0.12	0.55±0.08	1.26±0.17	0.82±0.11

mean of the distribution shown in Figure 4.23 was less than 2%. In addition, as shown in Fig. 4.24, no dependence of underlying event E_t density on average cluster energy was observed.

In principal, some of the energy belonging to the jets may have contributed to the 'off-axis' energy bands. In order to estimate the size of this effect a second analysis was performed on a data sample that had one cluster in the central and one with $|y| \geq 2.0$. The 'central-central' sample had two jets which could contribute to the 'off-axis' band whereas the 'central-plug' sample had only one. As discussed in Ref. [48] and shown in

Table 4.7, the central-plug sample agreed within statistical uncertainty with the central-central sample. From this it was concluded that, to within the statistical uncertainty on the central-plug sample, the 'off-axis' bands did not have a contribution from the two leading jets.

Other systematic uncertainties associated with the determination of the E_t in the off-axis bands are discussed in Ref. [48]. When the uncertainties are combined they give 0.72 ± 0.23 GeV/radian-unit rapidity, for the average E_t density of the 'underlying event' in raw data.

Since the underlying event correction will be applied to the detector-corrected curve, an estimate of the detector corrected underlying event E_t was required. To find the detector-corrected estimate of the underlying event, tracking and pedestal corrections were applied to the di-jet data and the mean 'track-corrected' off-axis E_t was measured. From the Monte Carlo simulated data the 'track-corrected' and detector corrected off-axis E_t were also measured. Table 4.8 shows the track-corrected off-axis E_t density as measured in the data and the Monte Carlo sample. The Monte Carlo track corrected off-axis E_t density was 33% higher than that found in the data. To account for this, the Monte Carlo measurement of the detector corrected E_t density, also shown in Table 4.8, was scaled down by 77% which is the ratio of track corrected E_t in the Monte Carlo to the track corrected E_t in the data. The result was a detector corrected E_t density of 1.36 GeV/radian-unit rapidity. As discussed below, there was a large theoretical uncertainty in the estimate of the fraction of off-axis E_t that is due to the underlying event. Since this was the case, any additional systematic error in converting the track corrected off-axis E_t to detector corrected E_t was ignored, and the 34% uncertainty

Table 4.8: E_t Density [GeV/unit rapidity-radian]

	Data	Monte Carlo
Track Corrected	0.92	1.20
Detector Corrected	1.36	1.77

in the measurement from the raw data was taken as the uncertainty in the detector corrected off-axis E_t .

While the 'central-plug' study indicated that there was no discernable contribution from the two leading jets at 90° from the thrust axis, there was a large theoretical uncertainty about the contribution to the off-axis E_t from low energy gluons radiated from the partons. The amount of gluon radiation in off-axis bands for clean di-jet events is intrinsically based on the theoretical model and on higher order corrections. In particular, estimates using the HERWIG Monte Carlo indicated that 50% of the energy in the bands may come from the parton level scattering and shower evolution[25] . To cover the range of theoretical uncertainty for the underlying event, the $< Q_t > / E_t$ curve will be corrected assuming 75% of the energy in the bands is from the underlying event and an additional uncertainty of 25% will be included.

The average contribution of the 'underlying event' to E_t and Q_t was derived by assuming an isotropic distribution of energy in the central detector. The total average E_t added to an event by the underlying event was just the E_t density multiplied by the area of the detector, 2.2 units of rapidity by 2π radians. To find the contribution to Q_t , first the average energy deposited in a 15° slice, E_t^n, (corresponding to the ϕ segmentation of the calorimeter) is calculated from the energy density. Then the contribution to Q_t is calculated by summing over each calorimeter slice, and assuming that the energy of each slice is located at the center of the tower:

$$Q_t^{underlying\ event} = \sum_{n=0}^{23} |E_t^n sin(n * 15^\circ + \phi_{thrust})|.$$

A random number was used to determine the location of the thrust axis within a tower, ϕ_{thrust}, to account for the fact that the thrust axis may occur anywhere. By averaging over a large number of randomly generated thrust axes the angular piece of the underlying event Q_t can be expressed empirically as a linear function of the underlying event density,

$$Q_t^{underlying\ event} = 8.8 * E_{t\ density}.$$

Thus, the average detector corrected underlying event E_t density is 1.02 GeV/radian-unit rapidity $\pm$ 0.35 Gev/radian-rapidity measurement uncertainty $\pm$ 0.25 theoretical uncertainty. The average contribution to E_t is then 14.1 $\pm$ 8.3 GeV and the average contribution to Q_t is 9.0 $\pm$ 5.3 GeV. Finally, correcting the $< Q_t > /E_t$ curve involves subtracting the underlying event $< Q_t >$ and E_t separately from the detector corrected bins of $< Q_t >$ and E_t in the data, and then recalculating $< Q_t > /E_t$.

However, this average correction does not take into account the shape of the underlying event E_t spectrum and how this interacts with the steeply falling jet E_t spectrum. Since Q_t is plotted versus total E_t , which includes the underlying event E_t , and there are many more events in bins of parton E_t below a given bin than in that bin itself, a significant contribution to a given bin of total E_t comes from events with low parton E_t that have a high fluctuation in underlying event. This would cause the average underlying event E_t density measured in di-jet data to be systematically lower than the average underlying event E_t density in a given bin of total E_t .

As a test of whether an average underlying event correction is valid, an independent Monte Carlo analysis was performed, in which the parton E_t and Q_t distributions were 'smeared' by the underlying event spectrum. The smearing was accomplished by randomly selecting the underlying event E_t in 20° ϕ slices according to the off-axis E_t distribution shown in Fig. 4.23 and then calculating the corresponding contribution to Q_t assuming a thrust axis randomly oriented in ϕ . From the smeared distribution, the true underlying event contribution to Q_t and E_t was calculated, since the 'true' parton E_t and Q_t were known. It was found that the correction which would take the smeared Q_t and E_t distributions back to the parton Q_t and E_t , without the underlying event, were somewhat different from the average correction we would apply to the detector corrected $< Q_t > /E_t$ curve. Figure 4.25 shows the underlying event contribution to Q_t and E_t for the smeared and unsmeared techniques. As expected, without including the effect of the underlying event smearing of the E_t spectrum, the contribution of the underlying event was underestimated.

a

b

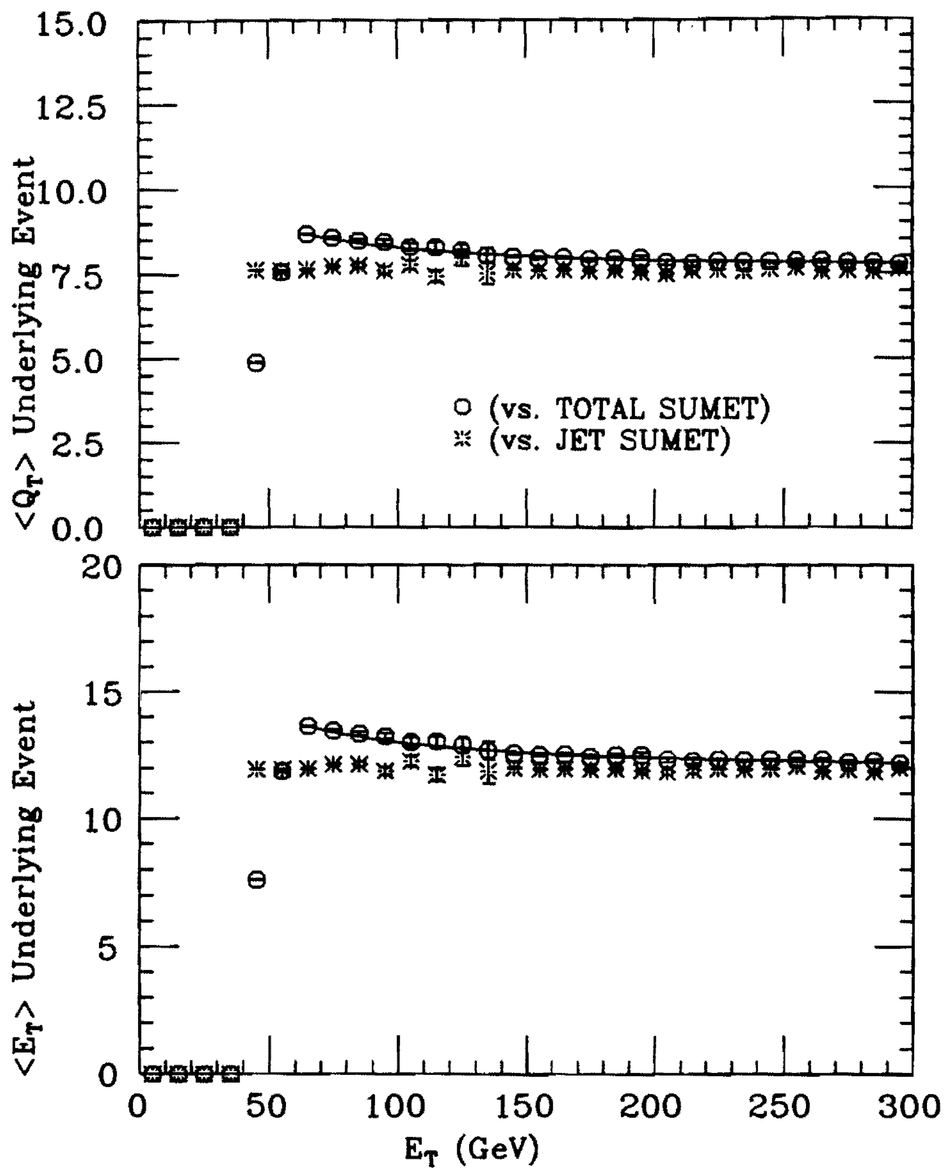

Figure 4.25: Underlying event contributions to a) E_t and b) $< Q_t >$, with and without underlying event smearing corrections.

Figure 4.26 shows the detector corrected $< Q_t > /E_t$ curve before and after the smeared underlying event correction was applied. The dashed bands indicate the range of uncertainty from the detector corrections, pedestals and the underlying event measurement, and thus represent the total uncertainty associated with the measurement of $< Q_t > /E_t$ from the data.

The theoretical uncertainty in the determination of the underlying event energy adds an additional uncertainty to this measurement. To include this, the data was corrected assuming A) 100% of the energy in the off-axis bands was from the underlying event and B) that 50% of the energy in the off-axis bands was from the underlying event. Figure 4.27 shows the underlying event subtracted data where the upper solid band represents the upper edge of the systematic uncertainty for the 50% subtraction and the lower solid line represents the lower edge of the systematic uncertainty for the 100% subtraction. As in the previous figure, the dashed bands indicate the size of the systematic uncertainty in the measurement of $< Q_t > /E_t$. Because the theoretical uncertainty from the underlying is a fundamental uncertainty, the solid bands are taken as the total uncertainty in the determination of $< Q_t > /E_t$.

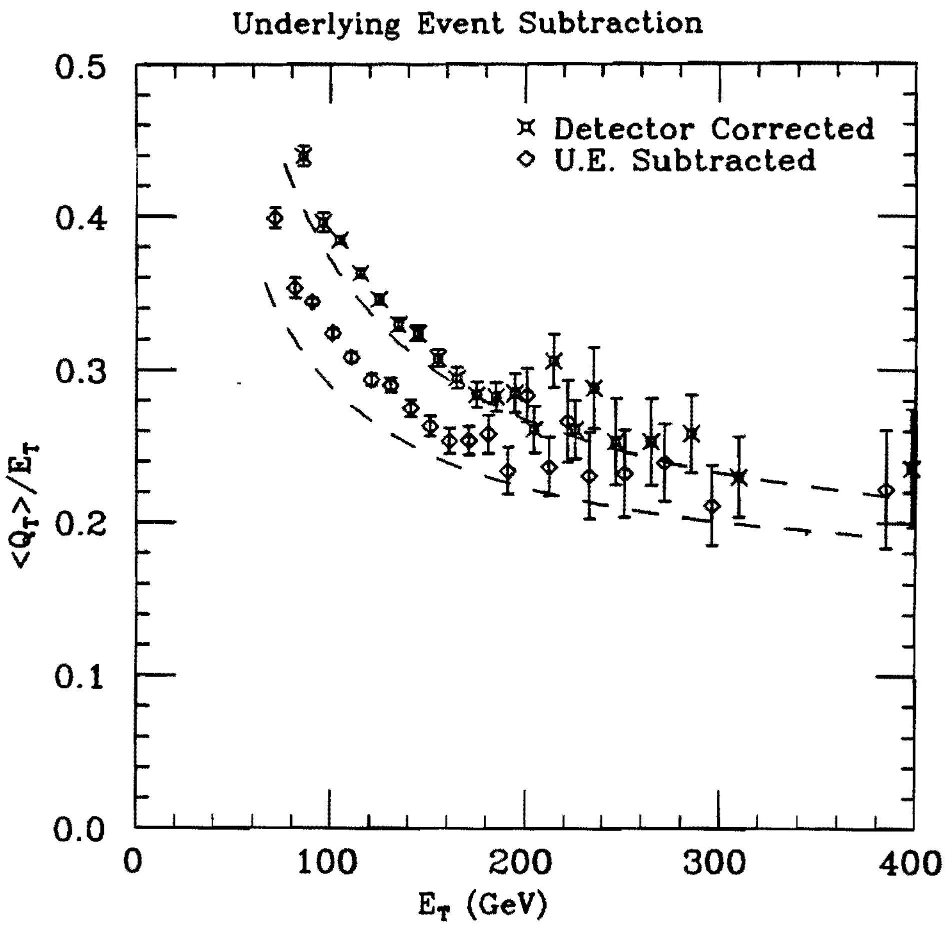

Figure 4.26: Detector corrected $< Q_t > / E_t$ vs. E_t before and after underlying event subtraction. Dashed lines indicate range of uncertainty from detector corrections, pedestals, and the underlying event measurement.

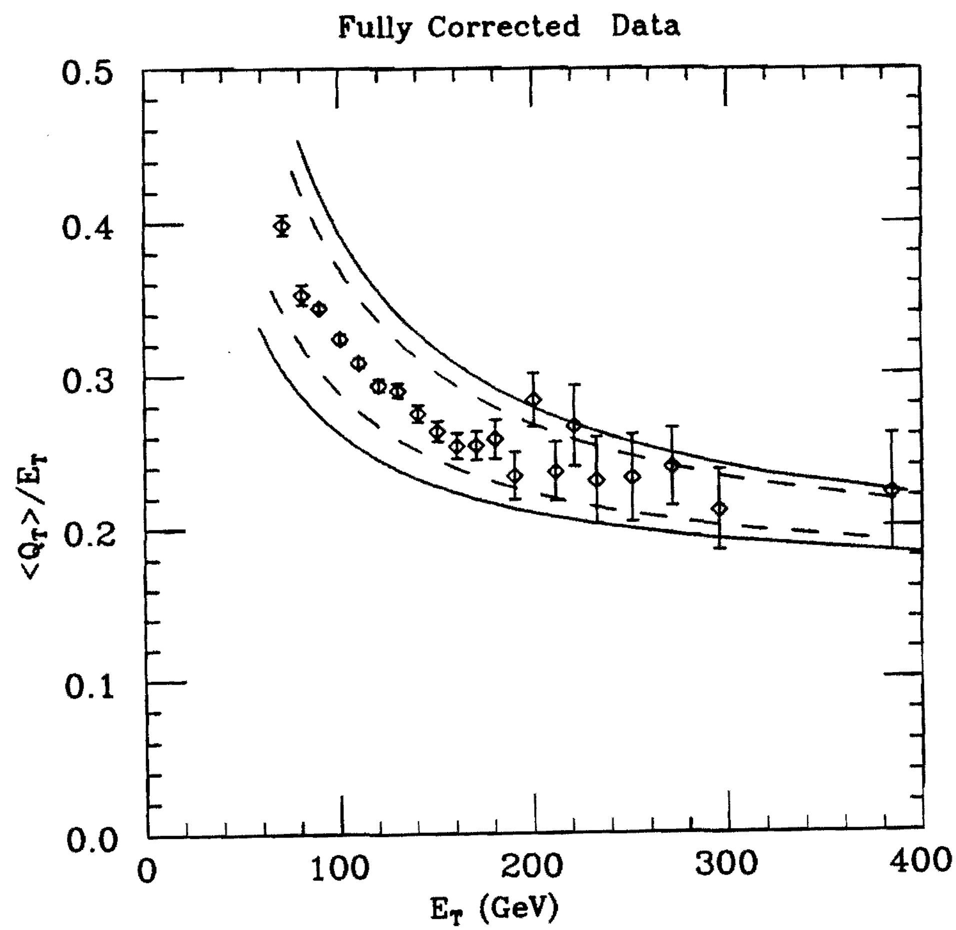

Figure 4.27: Underlying Event Subtracted $< Q_t > / E_t$ vs. E_t . Dashed lines indicate range of uncertainty from detector corrections, pedestals, and the underlying event measurement. Solid lines represent total systematic uncertainty.

Chapter 5

Summary and Conclusions

5.1 Comparisons to Theoretical Predictions

In the previous chapter the analysis of the data was described and performed. The result was a $< Q_t > /E_t$ versus E_t distribution which was corrected for the effects of the detector and the underlying event. The effect of hadronization is a fundamental theoretical uncertainty and thus the data was not corrected assuming any particular fragmentation-hadronization model. Rather, the data will be compared to theoretical predictions which include the appropriate hadronization model for the specific parton level prediction. Note that all of the theoretical plots presented below were generated without an underlying event, since the data has already been corrected for that effect.

The original prediction for $< Q_t > /E_t$ from Ellis and Webber was based on QCD parton level calculations of $2 \Rightarrow 2$ and $2 \Rightarrow 3$ processes. By making a slight modification to the PAPAGENO program, the Ellis and Webber calculation was reproduced. In addition, the effect of events which were not completely contained in the central detector region were included. Figure 5.1 shows the PAPAGENO parton level result compared to the data. Although this QCD prediction does not explicitly include the effects of hadronization, it shows a level and shape of $< Q_t > /E_t$ which is similar to the data.

The effect of hadronization is expected to be largest for events were one of the gluons has very low energy, i.e. energy comparable to the typical hadronization energy. To investigate the effects of hadronization on this type of event, output from the PAPAGENO $2 \Rightarrow 2$ process was passed through a hadronization program. The resulting $< Q_t > /E_t$ curve is shown in Fig. 5.2 compared to the data. If no hadronization were

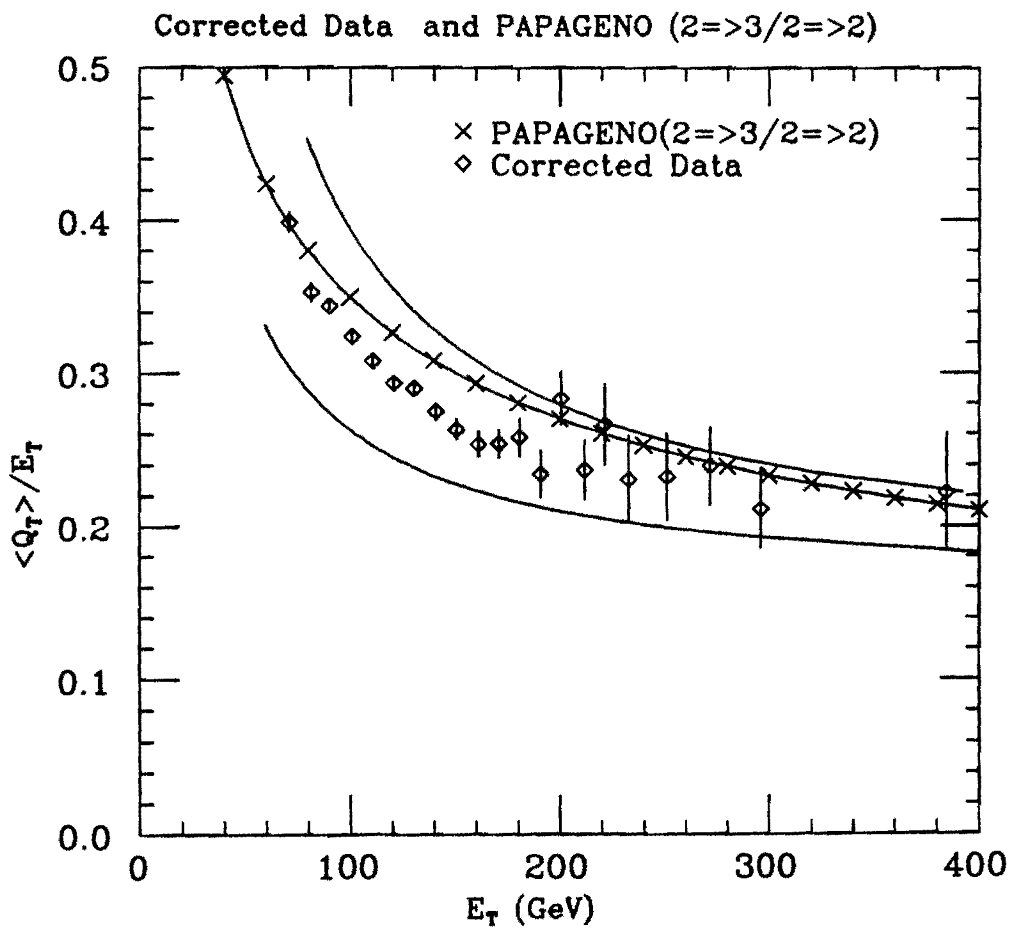

Figure 5.1: $< Q_t > / E_t$ vs. E_t for corrected data compared to PAPAGENO $< Q_t > / E_t$ parton level ($2 \Rightarrow 3$ / $2 \Rightarrow 2$) prediction. Solid lines indicate the total systematic uncertainty in the data.

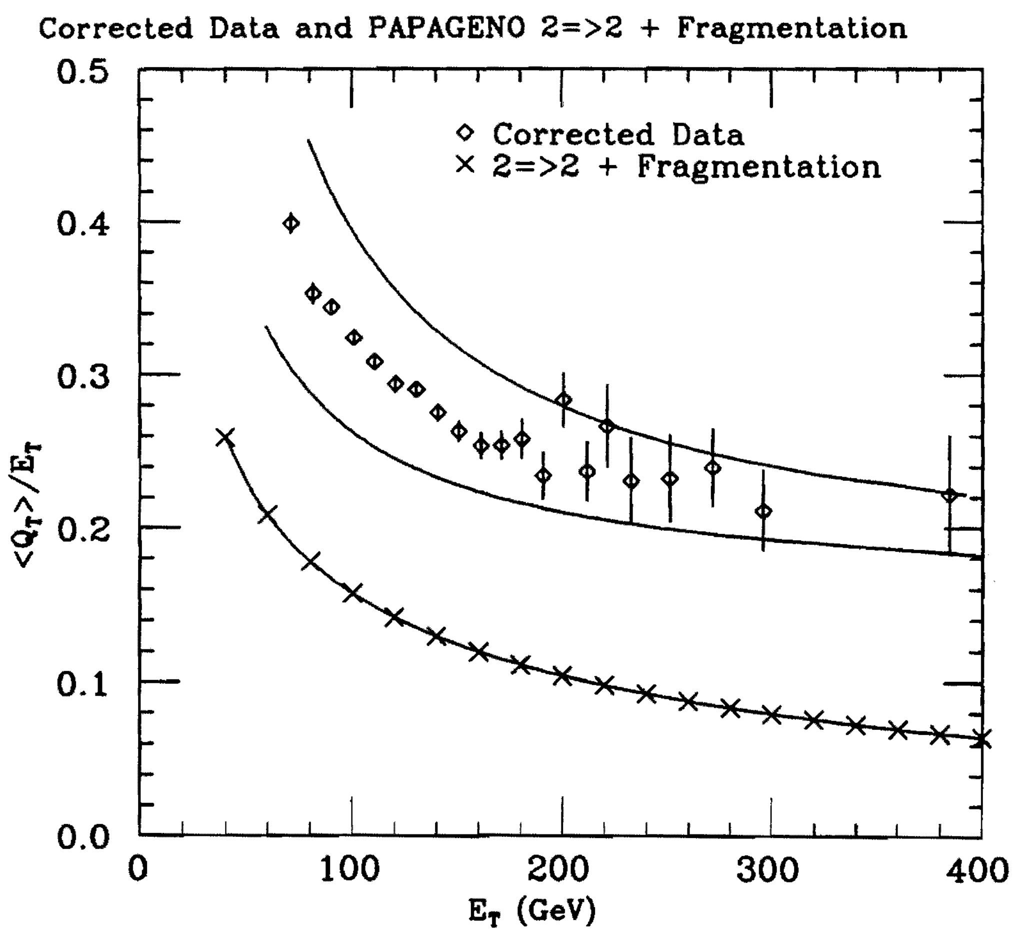

Figure 5.2: $< Q_t > / E_t$ vs. E_t for corrected data compared to PAPAGENO $2 \Rightarrow 2$ + hadronization. Solid lines indicate the total systematic uncertainty in the data.

performed, the $< Q_t > /E_t$ for the $2 \Rightarrow 2$ process would be identically zero. Clearly, this model of hadronization adds a significant amount of Q_t to the $2 \Rightarrow 2$ events, although it is not enough to bring the $2 \Rightarrow 2$ QCD prediction into agreement with the data. In other words, the $2 \Rightarrow 3$ QCD process must be included to achieve the level of $< Q_t > /E_t$ observed in the data.

As an alternative model to QCD, 3-body phase space for the final state partons was investigated. Figure 5.3 shows the parton level phase space prediction compared to the corrected data. This is the phase space $< Q_t > /E_t$ curve that is analogous to the QCD PAPAGENO prediction and it shows a distinct difference in shape from the data.

An attempt was also made to come up with an alternative $< Q_t > /E_t$ prediction based simply on the observation of distinct two and three-jet events. The PAPAGENO $2 \Rightarrow 2$ + hadronization $< Q_t > /E_t$ curve was combined with the curve from the separated phase space three-jet events assuming different mixtures of di-jet and tri-jet events. Figure 5.4 shows these curves compared to the corrected data. Clearly any reasonable combination of the di-jet curve with the separated tri-jet curve does not agree with the data.

Finally, a leading log Monte Carlo, HERWIG, was used to generate a 'state-of-the-art' QCD prediction. HERWIG includes the effects of gluon interference and coherence and performs the full QCD shower evolution (bremsstrahlung) to a low gluon mass cut-off (0.6 Gev). The hadronization technique employed by HERWIG indicates a small contribution to the $< Q_t > /E_t$ distribution. Figure 5.5 shows the data compared with the HERWIG result for hadronized partons. Good agreement is observed over the E_t range of the data.

5.2 Conclusions

The theoretical and experimental determination of the global event parameter Q_t has been described. Measurement of Q_t in the high E_t CDF jet data is an important test of

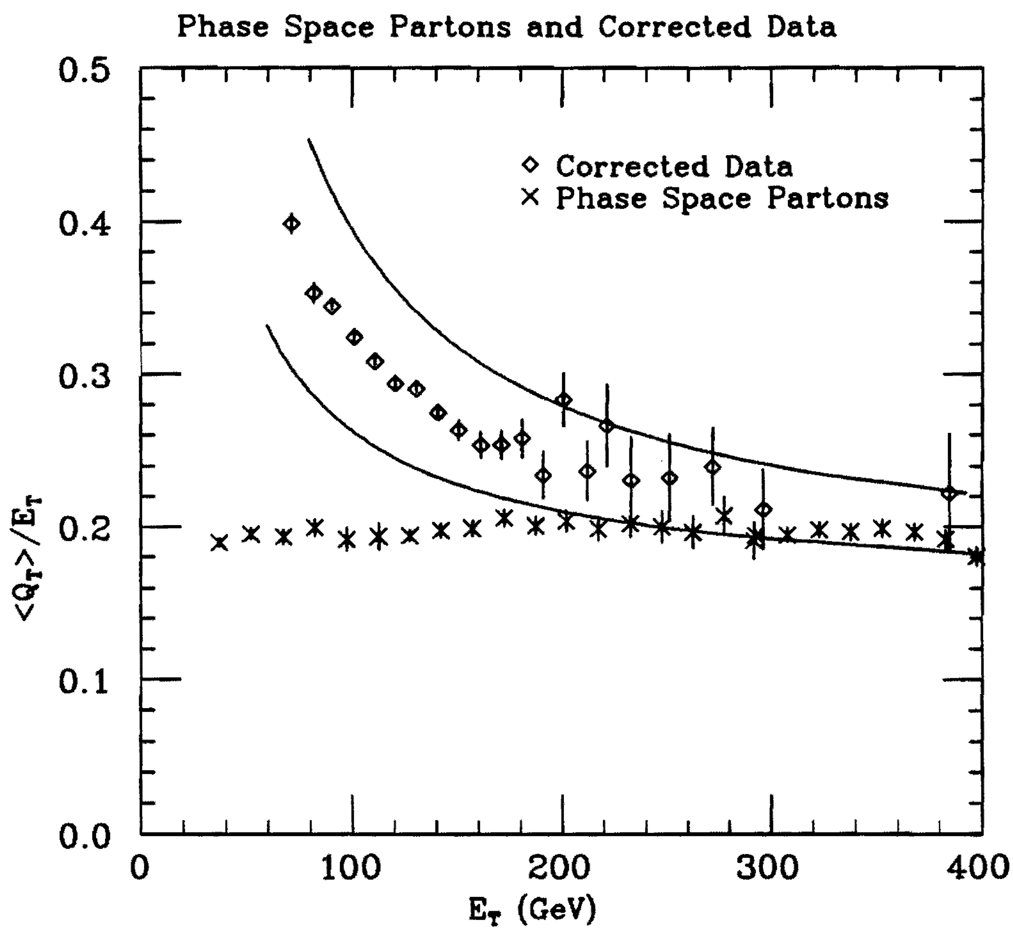

Figure 5.3: $< Q_t > / E_t$ vs. E_t for corrected data compared to parton level 3-body phase space calculation. Solid lines indicate the total systematic uncertainty in the data.

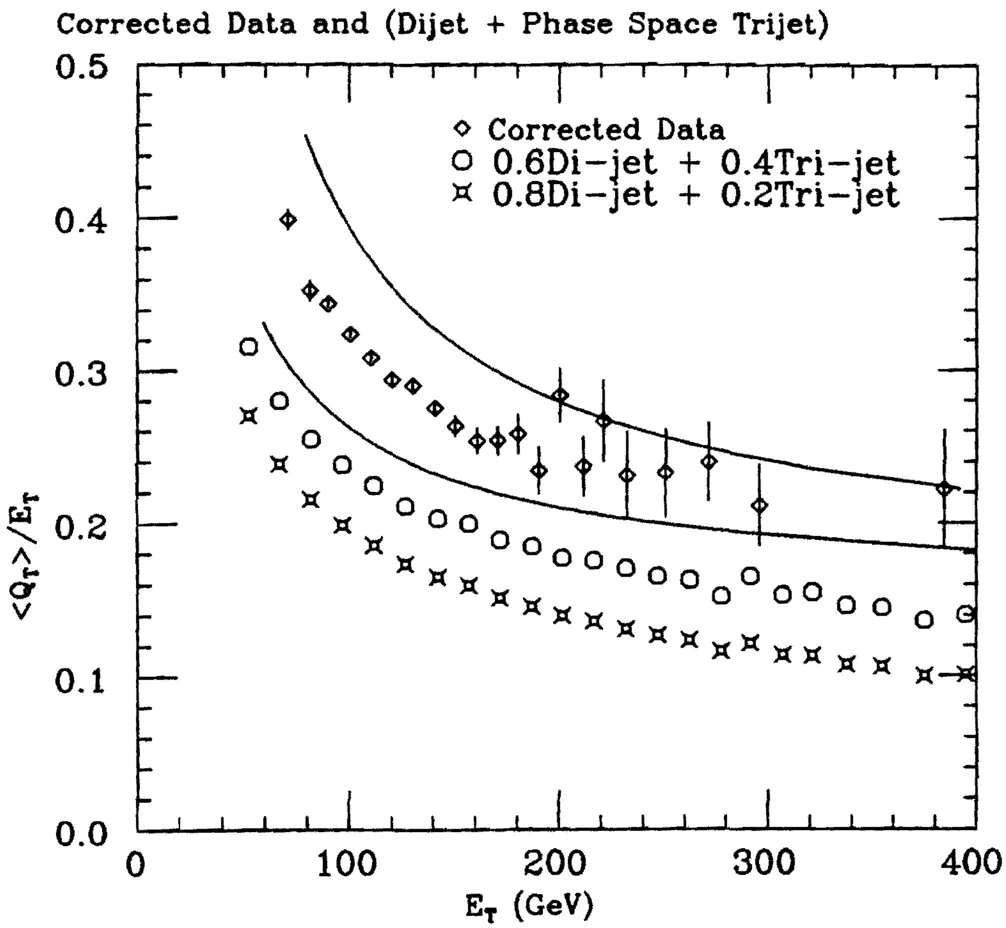

Figure 5.4: $< Q_t > / E_t$ vs. E_t for corrected data compared to combined two and three-jet curves. Solid lines indicate the total systematic uncertainty in the data.

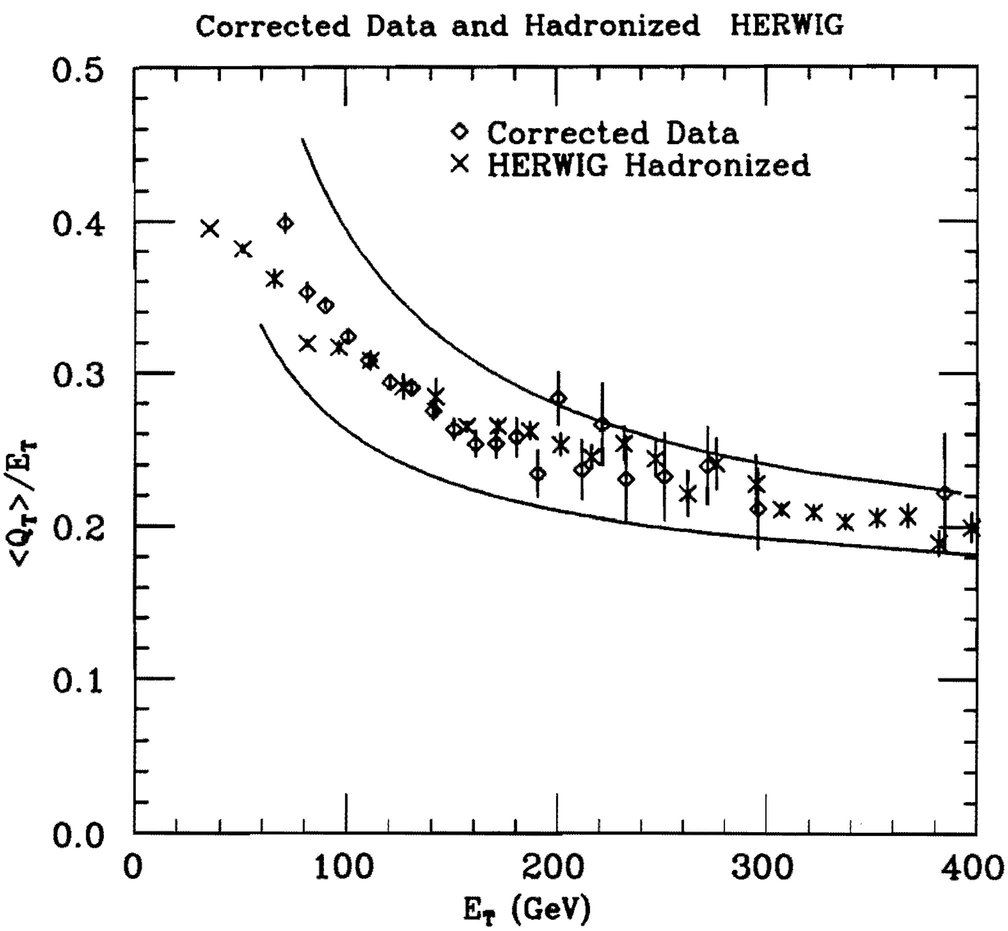

Figure 5.5: $< Q_t > / E_t$ vs. E_t for corrected data compared to HERWIG hadronized partons. Solid lines indicate the total systematic uncertainty in the data.

the low energy gluon region of QCD predictions which are generally excluded in clustering types of analysis. Although, in principle, Q_t is insensitive to soft hadronization effects, a sensitivity to the theoretical definition of the division between hadronization and gluon bremsstrahlung has been observed. Since the effect of hadronization is fundamentally a theoretical issue, the data has not been hadronization-corrected and comparisons are made to either parton level predictions or hadronized parton calculations where appropriate. The parton level calculation suggested a sensitivity to the running of the strong coupling constant, α_s , but there is a large uncertainty from the theoretical definition of hadronization and its effect on $< Q_t > /E_t$.

As a global parameter, Q_t is sensitive to energy depositions away from the jets and thus the underlying event introduces a large correction. The dominant uncertainty in the measurement of $< Q_t > /E_t$ came from the underlying event, although uncertainty from the calorimeter pedestals were not insignificant.

The data has been shown to be consistent with the QCD parton level calculation of $< Q_t > /E_t$, while being inconsistent with the analogous 3-body phase space calculation. The data is also inconsistent with a $2 \Rightarrow 2$ parton level calculation plus hadronization and is consistent with the full leading log Monte Carlo program, HERWIG, which includes the effect of a running coupling constant and hadronization. The main significance of the measurement of $< Q_t > /E_t$ is that it probes a region of QCD predictions which have historically been ignored for $p\bar{p}$ data: high energy collisions with sensitivity to low energy gluon emission.

Appendix A

Algorithm for Calculation of α_s

The parameterization of α_s in the one-loop Leading Log Approximation has the form:

$$\alpha_s(Q) = 1/(Bln(Q^2/\Lambda^2)),$$

where $B = (33 - 2f)/12\pi$ and f is the number of quark flavors. The number of flavors depends on the energy (Q scale) of the event. The value for f, was determined from the restriction that

$$Q^2 \geq 4M_q^2,$$

where M_q is the mass of a given quark. The quark masses that were used in these calculations were $M_{charm} = 1.5\ GeV, M_{bottom} = 4.5\ GeV$ and $M_{top} = 40\ GeV$. If Q was smaller than $4M_{charm}^2$ then $f = 3$ was used.

To make a smooth transition between the quark flavors, another term was included when the Q of an event did not exactly correspond to a quark flavor. For example, if Q was between $f = 3$ and $f = 4$ then

$$1/\alpha_s(Q) = B_3 ln(4M_{charm}^2/\Lambda^2) + B_4 ln(Q^2/4M_{charm}^2),$$

where B_3 refers to using $f = 3$ and B_4 refers to using $f = 4$.

This algorithm was used by the Ellis and Webber calculations and, for consistency, was also incorporated into the PAPAGENO programs.

Appendix B
The Level 3 Trigger

This appendix was adapted from Ref.[49] which was presented shortly after the end of the 1987 data run.

B.1 Introduction

The third level of the CDF trigger uses the Fermilab Advanced Computer Program system of parallel processors in VME crates which are managed by a MicroVAX II and are interfaced to the FASTBUS data acquisition system. The Level 3 trigger decision was made by FORTRAN filter algorithms executing in a system of 32-bit parallel processors which resided in VME[50]. CDF and the Advanced Computer Program at Fermilab (ACP) have developed a system of fast interfaces for transporting event data from the FASTBUS detector read-out to VME. Tests with a small seven processor system were conducted during the Spring, 1987, run of CDF and this is the main subject considered below. By the start of the 1988-89 run, the Level 3 system was operating with an on-line processing capacity roughly equivalent to 35-40 VAX 11/780's.

B.2 Level 3 Components

The interface between the CDF FASTBUS network and the Level 3 processor farm consists of a FASTBUS Branch Bus Controller (FBBC)[51], a 32-bit data and control signal path called Branch Bus[52], and a Branch Bus to VME interface (BVI)[52]. A schematic representation of this system is shown in Fig. B.1. The Branch Bus and BVI were designed by ACP and the FBBC was developed by CDF. Branch Bus is

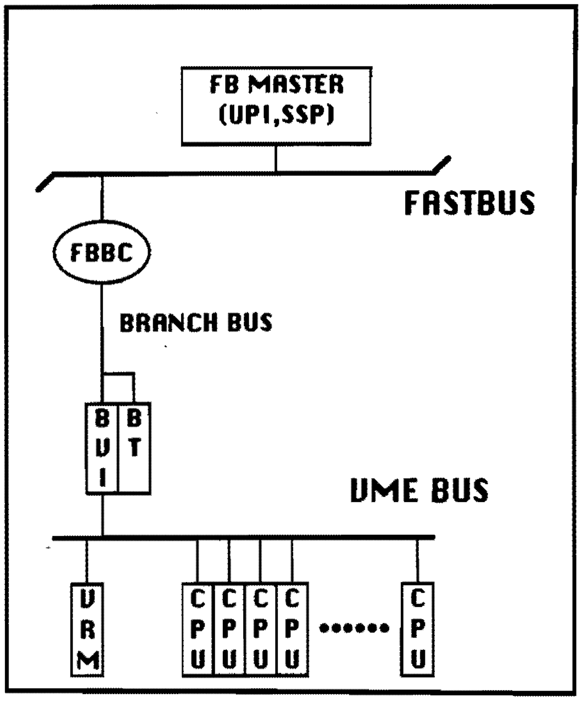

Figure B.1: FASTBUS to VME Interface System

implemented in two 50-wire twisted pair flat cables with a maximum length of about 50 ft. Multiple VME crates can be daisy-chained together on Branch Bus. All Branch Bus transfers use a non-handshake pipelined protocol with a maximum tested transfer rate of 20 Mbytes/sec. Level 3 needs this high transfer rate for writing events into the processor farm.

B.2.1 The FASTBUS to Branch Bus Controller

The FASTBUS to Branch Bus Controller (FBBC) is a FASTBUS slave which can transfer 32-bit data words from FASTBUS to Branch Bus with transparent management of the differences in bus protocol. The FBBC has the following features: i) Geographical and Segment extended addressing, ii) random single word read/write to VME, iii) handshake block transfers, iv) pipelined block transfers with a minimum FASTBUS cycle time of 200 nsec/32-bit word and v) options for byte or word swapping on each

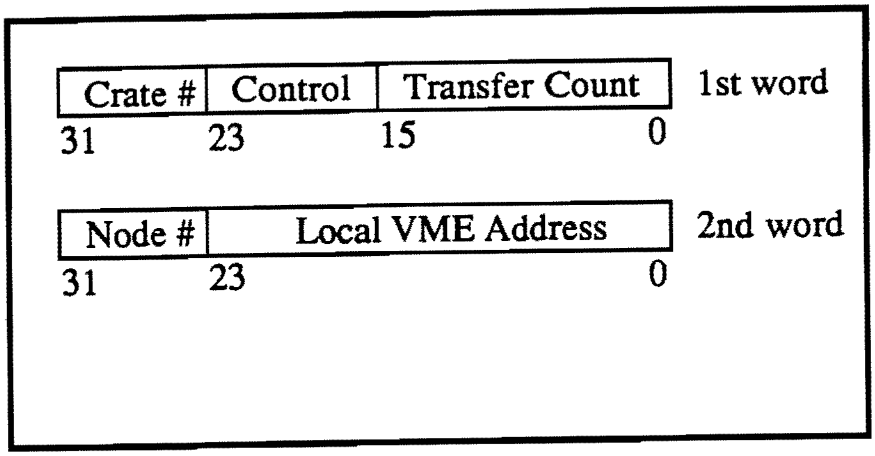

Figure B.2: FBBC Control Words

32-bit word transfer.

When the FBBC receives a FASTBUS primary address cycle, it initiates two control cycles which precede all Branch Bus transfers. For geographical addressing, the first control word is taken from FBBC CSR 10 and the FASTBUS secondary address is output as the second control word. The bit assignments of these words are shown in Fig. B.2. During event transfer to a Level 3 processor the most significant byte of the first control word contains the VME crate number of the processor. In the second control word bits 31-25 contain the node number and the lower 24 bits give the byte address in node memory.

Compatability with VAX and MicroVAX interfaces required the FBBC design to use a FASTBUS secondary address defined in words rather that bytes for locations in processor memory. During large block transfers the VAX or MicroVAX interface calculates the address of sub-blocks, assuming that the slave module is defined with word addressing. Consequently, the FBBC must shift the FASTBUS secondary address up by two bits to provide a byte address in the second Branch Bus control word (see Fig. B.2).

The FBBC can also be addressed using Segment extended addressing where the

Group Address (GA) field in the FASTBUS primary address specifies the VME crate. The FBBC will respond to addresses greater than 31 (decimal) and the offset from 32 is the VME crate number, e.g., GA = 33 would select VME crate 1. When Segment extended addressing is used, the decoded VME crate number from the FASTBUS primary address cycle is put in the upper eight bits of the first Branch control word and the VME crate number in CSR 10 is ignored. Segment extended addressing allows the FASTBUS master to change VME crates without performing an intermediate write of FBBC CSR 10.

The FBBC uses a 32 word FIFO to provide internal buffering on all read and write operations. For correct operation a FASTBUS master must respond correctly to the FASTBUS WAIT cycles (WT). The FBBC raises WT whenever its FIFO becomes half full. Even if the FASTBUS master is slower than the Branch Bus to VME interface, a FASTBUS wait could be generated during a VME bus arbitration or a memory refresh cycle in the processor. When the FASTBUS master terminates a single word or block read, the FBBC generates a Branch Bus reset cycle which clears the Branch Bus to VME interface and releases the VME crate. The FBBC has logic for byte and 16-bit half-word swapping in the 32-bit data path to allow transformation from DEC to IBM/Motorola byte ordering on each read or write transfer. These swap options are controlled by bits 22-23 in FBBC CSR 10. Errors on Branch Bus are latched by the FBBC and stored in CSR 0. An LED on the front panel of the FBBC indicates if an error has occurred.

B.2.2 Branch Bus to VME Interface

Each Level 3 VME crate will have a Branch Bus to VME Interface (BVI) module[52]. During event transfers to a Level 3 processor the BVI uses a FIFO for internal buffering and asserts the Branch Bus WAIT signal to inhibit transfer if the FIFO becomes half full. If the Branch Bus transfer rate is slower than the VME transfer rate, WAIT may still be necessary during a VME arbitration cycle or a CPU memory refresh cycle. Bits

17-16 in the first control word (see Fig. B.2) provide options for VME single word or sequential addressing by the BVI. The least significant 16 bits in this first control word contain a count of the number of 32-bit words to be read from processor memory. This transfer count is not used in a write to processor memory. When the FASTBUS master requests a read from processor memory, the BVI reads from VME and transmits over Branch Bus the number of 32-bit words specified by this transfer count. There is no internal buffering in the BVI for read operations. A FASTBUS module reading an accepted event from a Level 3 node can set the transfer count to an arbitrary large value and automatically terminate the transfer with a Branch Bus reset cycle when the FASTBUS block length has been received.

B.2.3 Level 3 Processors

The Level 3 microprocessor farm system was developed by the Fermilab Advanced Computer Program (ACP)[52]. The processors are based on the Motorola 68020 CPU with the 68881 floating point coprocessor. The CPU is installed on a standard single width double height VME card together with 2 Mbytes DRAM and a VME bus master/slave interface. It operates with a clock cycle of 16.6 MHz and uses interleaved memory. Sequential memory read cycles execute in 240 ns (one wait state) and sequential write cycles in 120 ns (0 wait states). A 2 microsec memory refresh cycle is performed every 125 microsec. The slave interface supports sequential/block transfers with 240 ns per 32-bit longword for read operations and 120 ns for writes into memory.

B.2.4 Installation and VME Arbitration

The Level 3 processors are installed in a VME crate with bus control and interface modules. A maximum of 17 (18) processors can be installed in one crate with (without) a Branch Bus terminator module. A VME Resource Module (VRM) is normally the VME crate controller[52]. It must be located in slot 1 on the left side of the crate. During sequential transfers to and from VME it provides bus arbitration. A new arbitration cycle occurs every 64 longwords. The VRM can be set for priority arbitration, in which the highest priority master will be given control of the bus at the next arbitration cycle, or it can be set to arbitrate in round robin mode, in which each master must complete its transfer (maybe more than 64 longwords) before the next master is given control. The VRM contains a 32-bit "attention register" and each processor can write to it at a specific VME address. The Level 3 system uses this register as a flag for nodes that have completed execution of an algorithm or that require any other service. The VRM also has a 32-bit "bus error address" latch which stores the address of the current VME cycle. The VME crates currently use a 5 volt, 150 amp power supply and are installed with ACP designed air cooling. CDF is developing an air cooling and temperature monitoring system that will be interfaced with the existing detector alarms system.

B.3 Hardware Tests and Results

To test the integrity of the FASTBUS to VME interface system a diagnostic program called L3EDIT[53] was developed. The main function of this program was to write blocks of data from FASTBUS to the processors on VME, read the data back and compare what was read to what was written. L3EDIT is a FORTRAN program which resides on a VAX or MicroVAX. The initial test setup used a dedicated FASTBUS and VME crate as shown in Fig. B.1. The tests can be executed by a VAX with a UNIBUS Processor Interface (UPI) to FASTBUS, by a MicroVAX with a Q-Bus Processor Interface (QPI) to FASTBUS or by a SLAC Scanner Processor (SSP) FASTBUS module[54]. Other test parameters that can be defined with L3EDIT include the data pattern, the size of the data block, the node memory range, byte and/or word swapping in the FBBC, and the use of pipelined, block or single word mode. Tests can be setup to loop over the node memory one or more times and results can be logged on disk. In the case of an SSP test, L3EDIT downloads the memory test program to the SSP, writes the test definition parameters to an SSP common block and then starts the SSP. L3EDIT reads the results of the SSP test from fixed locations in SSP memory and displays them in exactly the same way as for a VAX or MicroVAX test.

The SSP program was modified to run on a Level 3 processor. With this program one node could be used as a master to test the memory of another set of nodes. All node to node transfers are done in single word mode on VME and thus the SSP tests actually executed in shorter times. This test could be run at the same time as an L3EDIT test on a different node and was used for independent checks of the processor VME interfaces and to test for arbitration problems between the possible VME masters.

Most of the problems encountered were caused by differences in timing between the FBBC and BVI. The CDF test system provided the first opportunity to test the ACP Branch Bus at speeds above 2000 ns per 32-bit word. Together with the ACP engineers, the FBBC and BVI high rate transfers were debugged. As we learned more about the interface system and gained experience diagnosing problems, a series of tests were developed which we chose as the definition of a working system. A description of these tests can be found in Ref.[53].

TableB.1 shows some statistics for tests run over the entire 2 Mbyte address range of two nodes. These tests were performed in late October, 1986, after the final FBBC modifications were made. Each pass through memory in both nodes is referred to as a test. These tests all used incrementing patterns which were written, read and verified. The execution times shown include the time for test pattern generation and verification and are not a measure of interface transfer rate. All of these tests had 12,000 32-bit words per block transfer. These tests were terminated normally and no errors were found. The main goal of the tests was to prove that the system was stable at any speed for periods on the order of 15 hours.

The variety of possible FASTBUS masters allowed the interface system to be tested at different speeds. With the typical SSP clock crystal (50 MHz), the SSP can execute transfers to VME in block mode at 240 ns/32-bit word or pipelined mode at 120 ns/32-bit word. The SSP reads from VME only in block mode. To test the interface system at its design goal of 200 ns/32-bit word a 30 MHz crystal was used in the SSP. This

Table B.1: Hardware Tests and Results

FB Master	Tests	Blocks	Execution Time
SSP/Pipelined	8748	384,871	21 hr. 33 min.
SSP/Block	7178	315,801	17 hr. 51 min.
MicroVAX/QPI	916	58,622	15 hr. 4 min.
VAX/QPI	64	1,130	2 hr. 36 min.

produced a block mode speed of 400 ns/32-bit word and a pipelined speed of 200 ns/32-bit word. The UPI and QPI operate only in block mode at speeds of 400 ns/32-bit word. The ability to use different speed masters was essential to uncovering timing problems in the FBBC and BVI.

B.4 Level 3 Operation

CDF device initialization, detector read-out and other tasks are directed by the experimenters through a menu driven program called Run Control which executes on a VAX 785. While a run is in progress, data acquisition can be directed by FASTBUS masters and the host VAX need only access FASTBUS to read events which pass the final trigger. Accepted events are read into a global event buffer on the host VAX where they can be accessed by multiple consumer processes. Consumer processes perform functions such as logging events to tape, monitoring the run in progress and accumulating calibration data. For the run starting in Fall, 1988, event data which passed Levels 1 and 2 was read from the scanners by a FASTBUS module called an Event Builder[55]. A process, called the Buffer Manager, ran on a MicroVAX II and directed the flow of event data into and out of Level 3. The set of Level 3 processors, or farm, was managed by a process running on another MicroVAX II that we referred to as the Farm Steward. To access the LEVEL 3 farm, the Farm Steward used a Q-Bus Branch Bus Controller (BBC) which was designed by ACP. Communication between the Event Builder, Buffer Manager and the Farm Steward was via FASTBUS messages while communication with Run Control was via DECNET. If an event passed the Level 3 trigger it was read into the global event buffer on the host VAX.

B.4.1 Online Tests and Results

The four month run in the Spring of 1987 provided a test for part of the final Level 3 system. In this setup Level 3 was not in the data stream but could access events from the global event buffer after they had been accepted. We created a program called L3RUN that could run as a consumer process on the host VAX. L3RUN was a menu-driven program that simulates the Run Control and Buffer Manager parts of the final Level 3 setup that were necessary for preliminary testing. L3RUN read events from the global event buffer, sent them to a node, read them out when the node was finished and stored them on disk. To simulate the final system, the Farm Steward and L3RUN coordinate event input and read-out via FASTBUS and DECNET messages. The L3RUN program allowed us to test and develop the Farm Steward and filter algorithm code in an online environment with minimal interference with normal data taking. A flowchart of this setup is shown in Fig.B.3.

At the start of a run a DECNET link was established between the Farm Steward and L3RUN processes. Synchronous and asynchronous DECNET messages can be sent and received by both processes. To send and receive FASTBUS messages the Farm Steward uses a QPI. An interrupt receiver process, part of the Farm Steward, reads each 16 word FASTBUS interrupt message as soon as it is received and stores the message in a separate location until the Farm Steward can service it. This allows the Farm Steward to deal with the messages asynchronously and protects against the loss of messages if the Farm Steward cannot service an interrupt message immediately. In the 1988-1989 Level 3 setup, the Buffer Manager and the Farm Steward communicated via FASTBUS interrupt messages using this kind of interrupt receiver process.

After the DECNET link had been established, L3RUN sent a FASTBUS message to the Farm Steward instructing it to initialize the processor farm. The Farm Steward sent back lists of the nodes that were successfully initialized via FASTBUS and DECNET.

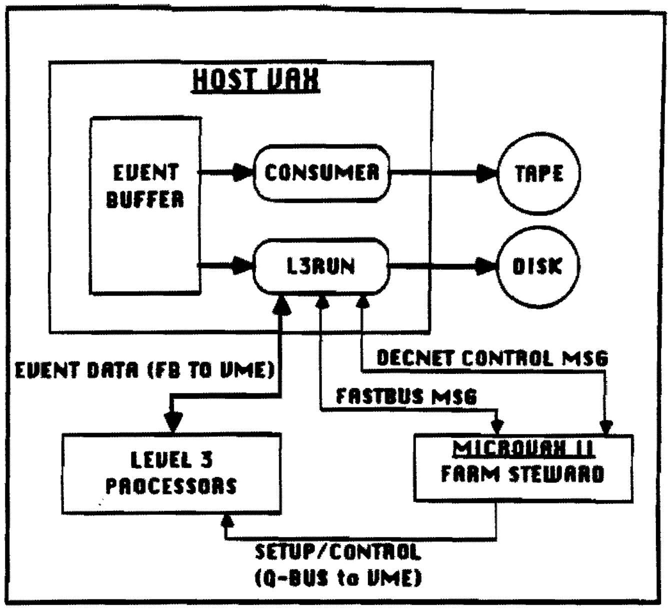

Figure B.3: Level 3 Test Setup with L3RUN Consumer Process.

L3RUN could then write events to the Level 3 processors. While a run was in progress the Farm Steward monitored the Level 3 processor status by reading the VRM attention register in each VME crate. When a bit was set in this register the Farm Steward read the trigger results from the corresponding node and sent them along with the address of the node to L3RUN in a FASTBUS message. L3RUN would read the event and could store it on disk. In the 1988-1989 system the trigger results were compared to the requested triggers, and events were only read if that trigger was requested.

We successfully ran this Level 3 system online with a processor farm of seven nodes during the 1987 CDF run. A filter algorithm that simulated the Level 1 and 2 trigger was used for this study. The processing rate was limited to approximately 1 Hz by the rate at which L3RUN received events from the global event buffer and the requirement that tests not interfere with the normal data taking on FASTBUS. (Event data sent to Level 3 accessed the same FASTBUS network as the detector read-out.) At this rate the Level 3 processor farm could keep up with the data flow. Node execution time for each event was approximately 2.1 seconds. The code was developed for the VAX where the execution time was about 1.25 seconds/event (VAX 11/780). These times are not strictly comparable since non-standard FORTRAN-77 intrinsic functions available on the VAX were emulated by subroutines in the nodes. Separate studies with comparable code found that each Level 3 processor has the processing power of approximately 67% of a VAX 780. During the 1988-1989 run a Level 3 system consisting of 55 nodes provided the online processing and third level trigger for the CDF data and is described in Ref. [56].

Appendix C

Event Generation and Simulation for Residual Corrections

The simulation program [46] reflects the detector geometry; the tower segmentation of the central detector is modeled with 0.1 segments in rapidity and 15° segments in ϕ . Energy deposited in a tower is shared between the two phototubes by the same method that is used to reconstruct the tower energy and ϕ centroid in raw data[40]. The ϕ cracks between modules are simulated with correction factors based on the impact point of the particle at the face of the calorimeter. The resolution for each type of calorimeter is discussed in Ref. [46] and reflects the resolutions described in Chapter 3.

Partons produced by the generator (ISAJET) are fragmented independently (Field-Feynman approach) and then the short-lived particles decay. (Note that 'fragmentation' here means the conversion of the fully evolved ISAJET partons into hadrons.) The parameters used in the fragmentation functions were tuned to give good agreement with the CDF jet data[47]. In addition to the hard parton collision, an underlying event was generated by ISAJET and simulated along with the hard collision products. The resulting hadrons, electrons, neutrinos, and other particles are projected through the magnetic field to the face of the calorimeter. From the locations, momenta, and directions of these particles after they have passed through the magnetic field, 'particle level' event parameters are determined. Particles that never reach the calorimeter (charged particles of P_t below 0.4 GeV curl in the magnetic field), and particles, such as neutrinos, that deposit no energy in the detector are also included. These 'particle level' event parameters represent the goal of the detector corrections, since they are what would be measured if the detector were 'perfect', i.e. could detect the energy of all particles emitted from the collision.

A large sample of events, jet plus underlying event, was generated and simulated with the standard falling E_t spectrum to allow effects caused by 'resolution smearing'. The resolution of the detector, combined with the steeply falling E_t spectrum, determines that a number of events will fluctuate up to higher E_t bins from low E_t ; this is called resolution smearing. After the generated events were passed through the detector simulation, the same type of tracking corrections were performed as was done in the data. The residual detector corrections were derived by comparing the fully simulated 'track corrected' event parameters to the 'particle level' event parameters described above.

Appendix D

The CDF Collaboration Lists

CDF Collaboration for the 1987 run

F. Abe,[16] D. Amidei,[3] G. Apollinari,[11] G. Ascoli,[7] M. Atac,[4] P. Auchincloss,[14] A. R. Baden,[6] A. Barbaro-Galtieri,[9] V. E. Barnes,[12] F. Bedeschi,[11] S. Belforte,[11] G. Bellettini,[11] J. Bellinger,[17] J. Bensinger,[2] A. Beretvas,[14] P. Berge,[4] S. Bertolucci,[5] S. Bhadra,[7] M. Binkley,[4] R. Blair,[1] C. Blocker,[2] J. Bofill,[4] A. W. Booth,[4] G. Brandenburg,[6] D. Brown,[6] A. Byon,[12] K. L. Byrum,[17] M. Campbell,[3] R. Carey,[6] W. Carithers,[9] D. Carlsmith,[17] J. T. Carroll,[4] R. Cashmore,[4] F. Cervelli,[11] K. Chadwick[4,12] T. Chapin,[13] G. Chiarelli,[11] W. Chinowsky,[9] S. Cihangir,[15] D. Cline,[17] D. Connor,[10] M. Contreras,[2] J. Cooper,[4] M. Cordelli,[5] M. Curatolo,[5] C. Day,[4] R. DelFabbro,[11] M. Dell'Orso,[11] L. DeMortier,[2] T. Devlin,[14] D. DiBitonto,[15] R. Diebold,[1] F. Dittus,[4] A. DiVirgilio,[11] J. E. Elias,[4] R. Ely,[9] S. Errede,[7] B. Esposito,[5] B. Flaugher,[14] E. Focardi,[11] G. W. Foster,[4] M. Franklin[6,7] J. Freeman,[4] H. Frisch,[3] Y. Fukui,[8] A. F. Garfinkel,[12] P. Giannetti,[11] N. Giokaris,[13] P. Giromini,[5] L. Gladney,[10] M. Gold,[9] K. Goulianos,[13] C. Grosso-Pilcher,[3] C. Haber,[9] S. R. Hahn,[10] R. Handler,[17] R. M. Harris,[9] J. Hauser,[3] T. Hessing,[15] R. Hollebeek,[10] L. Holloway,[7] P. Hu,[14] B. Hubbard,[9] P. Hurst,[7] J. Huth,[4] H. Jensen,[4] R. P. Johnson,[4] U. Joshi,[14] R. W. Kadel,[4] T. Kamon,[15] S. Kanda,[16] D. A. Kardelis,[7] I. Karliner,[7] E. Kearns,[6] R. Kephart,[4] P. Kesten,[2] H. Keutelian,[7] S. Kim,[16] L. Kirsch,[2] K. Kondo,[16] U. Kruse,[7] S. E. Kuhlmann,[12] A. T. Laasanen,[12] W. Li,[1] T. Liss,[3] N. Lockyer,[10] F. Marchetto,[15] R. Markeloff,[17] L. A. Markosky,[17] P. McIntyre,[15] A. Menzione,[11] T. Meyer,[15] S. Mikamo,[8] M. Miller,[10] T. Mimashi,[16] S. Miscetti,[5] M. Mishina,[8] S. Miyashita,[16] N. Mondal,[17] S. Mori,[16] Y. Morita,[16] A. Mukherjee,[4] C. Newman-Holmes,[4] L. Nodulman,[1] R. Paoletti,[11] A. Para,[4] J. Patrick,[4] T. J. Phillips,[6] H. Piekarz,[2] R. Plunkett,[13] L. Pondrom,[17] J. Proudfoot,[1] G. Punzi,[11] D. Quarrie,[4] K. Ragan,[10] G. Redlinger,[3] J. Rhoades,[17] F. Rimondi,[4] L. Ristori,[11] T. Rohaly,[10] A. Roodman,[3] A. Sansoni,[5] R. Sard,[7] V. Scarpine,[7] P. Schlabach,[7] E. E. Schmidt,[4] P. Schoessow,[1] M. H. Schub,[12] R. Schwitters,[6] A. Scribano,[11] S. Segler,[4] M. Sekiguchi,[16] P. Sestini,[11] M. Shapiro,[6] M. Sheaff,[17] M. Shibata,[16] M. Shochet,[3] J. Siegrist,[9] P. Sinervo,[10] J. Skarha,[17] D. A. Smith,[7] F. D. Snider,[3] R. St. Denis,[6] A. Stefanini,[11] Y. Takaiwa,[16] K. Takikawa,[16] S. Tarem,[2] D. Theriot,[4] A. Tollestrup,[4] G. Tonelli,[11] Y. Tsay,[3] F. Ukegawa,[16] D. Underwood,[1] R. Vidal,[4] R. G. Wagner,[1] R. L. Wagner,[4] J. Walsh,[10] T. Watts,[14] R. Webb,[15] T. Westhusing,[7] S. White,[13] A. Wicklund,[1] H. H. Williams,[10] T. Yamanouchi,[4] A. Yamashita,[15] K. Yasuoka,[16] G. P. Yeh,[4] J. Yoh,[4] F. Zetti,[11]

[1] *Argonne National Laboratory, Argonne, Illinois 60439*
[2] *Brandeis University, Waltham, Massachusetts 02254*
[3] *University of Chicago, Chicago, Illinois 60637*
[4] *Fermi National Accelerator Laboratory, Batavia, Illinois 60510*
[5] *Laboratori Nazionali di Frascati, Istituto Nazionale di Fisica Nuclear, Frascati, Italy*
[6] *Harvard University, Cambridge, Massachusetts 02138*
[7] *University of Illinois, Urbana, Illinois 61801*
[8] *National Laboratory for High Energy Physics (KEK), Tsukuba, Ibaraki 305, Japan*
[9] *Lawrence Berkeley Laboratory, Berkeley, California 94720*
[10] *University of Pennsylvania, Philadelphia, Pennsylvania 19104*
[11] *Istituto Nazionale di Fisica Nucleare, University and Scuola Normale Superiore of Pisa, Pisa, Italy*
[12] *Purdue University, West Lafayette, Indiana 47907*
[13] *Rockefeller University, New York, New York 10021*
[14] *Rutgers University, Piscataway, New Jersey 08854*
[15] *Texas A&M University, College Station, Texas 77843*
[16] *University of Tsukuba, Tsukuba, Ibaraki 305, Japan*
[17] *University of Wisconsin, Madison, Wisconsin 53706*

Figure D.1: Collaboration list for 1987 Run

CDF Collaboration for the 1988–1989 run

F. Abe,[8] D. Amidei,[4] G. Apollinari,[11] M. Atac,[4] P. Auchincloss,[14] A. R. Baden,[6] A. Bamberger,[4] A. Barbaro-Galtieri,[9] V. E. Barnes,[12] F. Bedeschi,[11] S. Behrends,[12] S. Belforte,[11] G. Bellettini,[11] J. Bellinger,[17] J. Bensinger,[2] A. Beretvas,[4] J. P. Berge,[4] S. Bertolucci,[5] S. Bhadra,[7] M. Binkley,[4] R. Blair,[1] C. Blocker,[2] G. Brandenburg,[6] D. Brown,[6] E. Buckley,[14] A. Byon,[12] K. L. Byrum,[17] C. Campagnari,[3] M. Campbell,[3] R. Carey,[6] W. Carithers,[9] D. Carlsmith,[17] J. T. Carroll,[4] R. Cashmore,[4] F. Cervelli,[11] K. Chadwick,[4] G. Chiarelli,[5] W. Chinowsky,[9] S. Cihangir,[4] A. G. Clark,[4] D. Connor,[10] M. Contreras,[2] J. Cooper,[4] M. Cordelli,[5] D. Crane,[4] M. Curatolo,[5] C. Day,[4] S. Dell'Agnello,[11] M. Dell'Orso,[11] L. DeMortier,[2] P. F. Derwent,[3] T. Devlin,[14] D. DiBitonto,[15] R. B. Drucker,[9] J. E. Elias,[4] R. Ely,[9] S. Errede,[7] B. Esposito,[5] B. Flaugher,[14] E. Focardi,[11] G. W. Foster,[4] M. Franklin,[6] J. Freeman,[4] H. Frisch,[3] Y. Fukui,[8] Y. Funayama,[16] A. F. Garfinkel,[12] A. Gauthier,[7] S. Geer,[6] P. Giannetti,[11] N. Giokaris,[13] P. Giromini,[5] L. Gladney,[10] M. Gold,[9] K. Goulianos,[13] H. Grassman,[11] C. Grosso-Pilcher,[3] J. Grunhaus,[13] C. Haber,[9] S. R. Hahn,[4] R. Handler,[17] K. Hara,[16] R. M. Harris,[9] J. Hauser,[3] T. Hessing,[15] R. Hollebeek,[10] L. Holloway,[7] P. Hu,[14] B. Hubbard,[9] T. Huffman,[12] R. Hughes,[10] P. Hurst,[7] J. Huth,[4] M. Incagli,[11] T. Ino,[16] H. Iso,[16] H. Jensen,[4] C. P. Jessup,[6] R. P. Johnson,[4] U. Joshi,[4] D. Jovanovic,[4] R. W. Kadel,[4] T. Kamon,[15] S. Kanda,[16] D. A. Kardelis,[7] I. Karliner,[7] E. Kearns,[6] R. Kephart,[4] P. Kesten,[2] R. M. Keup,[7] H. Keutelian,[7] S. Kim,[16] L. Kirsch,[2] K. Kondo,[16] S. E. Kuhlmann,[1] E. Kuns,[14] A. T. Laasanen,[12] J. I. Lamoureux,[17] M. E. Levi,[9] W. Li,[1] T. Liss,[7] N. Lockyer,[10] C. B. Luchini,[7] P. Maas,[4] M. Mangano[11] J. P. Marriner,[4] R. Markeloff,[17] L. A. Markosky,[17] R. Mattingly,[2] P. McIntyre,[15] A. Mensione,[11] T. Meyer,[15] S. Mikamo,[8] R. Mikawa,[3] M. Miller,[3] T. Mimashi,[16] S. Miscetti,[5] M. Mishina,[8] S. Miyashita,[16] Y. Morita,[16] S. Moulding,[2] A. Mukherjee,[4] L. Nakae,[2] I. Nakano,[16] C. Newman-Holmes,[4] J. S. T. Ng,[6] M. Ninomiya,[16] L. Nodulman,[1] S. Ogawa,[16] R. Paoletti,[11] A. Para,[4] E. Pare,[6] J. Patrick,[4] T. J. Phillips,[6] R. Plunkett,[4] L. Pondrom,[17] J. Proudfoot,[1] G. Punzi,[11] D. Quarrie,[4] K. Ragan,[10] G. Redlinger,[3] J. Rhoades,[17] F. Rimondi,[11] L. Ristori,[11] T. Rohaly,[10] A. Roodman,[3] A. Sansoni,[5] A. Savoy-Navarro,[4] V. Scarpine,[7] P. Schlabach,[7] E. E. Schmidt,[4] M. H. Schub,[12] R. Schwitters,[6] A. Scribano,[11] S. Segler,[4] Y. Seiya,[16] M. Sekiguchi,[16] P. Sestini,[11] M. Shapiro,[6] M. Sheaff,[17] M. Shochet,[3] J. Siegrist,[9] P. Sinervo,[10] J. Skarha,[17] K. Sliwa,[4] D. A. Smith,[11] F. D. Snider.[3] R. St. Denis,[6] A. Stefanini,[11] R. L. Swartz, Jr.,[7] M. Takano,[16] K. Takikawa,[16] S. Tarem,[2] D. Theriot,[4] M. Timko,[15] P. Tipton,[9] S. Tkaczyk,[4] A. Tollestrup,[4] G. Tonelli,[11] W. Trischuk,[6] Y. Tsay,[3] F. Ukegawa,[16] D. Underwood,[1] R. Vidal,[4] R. G. Wagner,[1] R. L. Wagner,[4] J. Walsh,[10] T. Watts,[14] R. Webb,[15] C. Wendt,[17] W. C. Wester, III,[9] T. Westhusing,[11] S. White,[13] A. Wicklund,[1] H. H. Williams,[10] B. Winer,[9] A. Yagil,[4] A. Yamashita,[16] K. Yasuoka,[16] G. P. Yeh,[4] J. Yoh,[4] M. Yokoyama,[16] J. C. Yun,[4] F. Zetti[11]

[1] *Argonne National Laboratory, Argonne, Illinois 60439*
[2] *Brandeis University, Waltham, Massachusetts 02254*
[3] *University of Chicago, Chicago, Illinois 60637*
[4] *Fermi National Accelerator Laboratory, Batavia, Illinois 60510*
[5] *Laboratori Nazionali di Frascati, Istituto Nazionale di Fisica Nucleare, Frascati, Italy*
[6] *Harvard University, Cambridge, Massachusetts 02138*
[7] *University of Illinois, Urbana, Illinois 61801*
[8] *National Laboratory for High Energy Physics (KEK), Tsukuba-gun, Ibaraki-ken 305, Japan*
[9] *Lawrence Berkeley Laboratory, Berkeley, California 94720*
[10] *University of Pennsylvania, Philadelphia, Pennsylvania 19104*
[11] *Istituto Nazionale di Fisica Nucleare, University and Scuola Normale Superiore of Pisa, I-56100 Pisa, Italy*
[12] *Purdue University, West Lafayette, Indiana 47907*
[13] *Rockefeller University, New York, New York 10021*
[14] *Rutgers University, Piscataway, New Jersey 08854*
[15] *Texas A&M University, College Station, Texas 77843*
[16] *University of Tsukuba, Ibaraki 305, Japan*
[17] *University of Wisconsin, Madison, Wisconsin 53706*

Figure D.2: Collaboration list for 1988-1989 Run

References

[1] W. Braunschweig et al. (TASSO Collaboration), DESY 89-069, (1989).

[2] I.H. Park et al. (AMY Collaboration), Phys. Rev. Lett. 62, (1989).

[3] W. De Boer, SLAC-PUB-4428, Sept. (1987).

[4] J. Dorfan, Proceedings of the International Lepton/Photon Symposium-Cornell University p. 686 (1983).

[5] B. Naroska, Phys. Rep. 148C 63 (1987).

[6] A. De Rújula, J. Ellis, E.G. Floratos, and M.K. Gaillard, Nuc. Phys. B138 387 (1978).

[7] F. Abe et al. (CDF Collaboration), Phys. Rev. Lett. 62, 613 (1989).

[8] F. Abe et al. (CDF Collaboration), Phys. Rev. Lett. 62, 3020 (1989).

[9] G. Arnison et al. (UA1 Collaboration), Phys. Lett. 158B, 494 (1985).

[10] R.K. Ellis and B.R. Webber, "Procceedings of the 1986 Summer Study on the Physics of the Superconducting Supercollider" p. 74, Snowmass (1986).

[11] Ch. Berger et al. (PLUTO Collaboration), Z. Phys. C - Particles and Fields 22, 103 (1984).

[12] V. Barger and R. Phillips, "COLLIDER PHYSICS", Addison-Wesley Pub. Co. (1987), p. 300.

[13] Ibid., p. 198.

[14] Ibid., p. 200.

[15] Ibid., p. 215.

[16] E. Eichten,I.Hinchliffe,K.Lane and C. Quigg, Rev. of Mod. Phys. 56, No. 4, Oct. (1984).

[17] V. Barger and R. Phillips, p. 226.

[18] Ibid., p. 306.

[19] Ibid., p. 312.

[20] Ibid., p. 211.

[21] F. Halzen and A.D. Martin, John Wiley and Sons Inc., (1984).

[22] Dokshitzer et al., Phys. Rep. 58C, 269 (1980).

[23] Ian Hincliffe, Monte Carlo Program PAPAGENO, in preparation, (1989).

[24] Michelangelo Mangano, private communication.

[25] G. Marchesini and B.R. Webber, Cavendish-HEP-87/8, UPRF-87-212, Dec. (1987).

[26] Monte Carlo Event Generator for pp and $p\bar{p}$ Reactions: Version 5.38, written by Frank E. Paige and Serban D. Protopopescu, Brookhaven National Laboratory, BNL 29777 (1981).

[27] D.Brown and Sheila Kannappan, CDF Note 873, Feb. 1989.

[28] F. Abe et al. (CDF Collaboration), Nucl. Inst. and Meth. A271 387-403 (1988).

[29] H. Minemura et al., Nucl. Inst. and Meth. A238 18 (1985).

[30] J.L Crawford and D.A. Finley, Fermilab Report, May/June (1987).

[31] F. Snider et al., Nucl. Inst. and Meth. A268 75-91 (1988).

[32] F. Bedeschi et al., Nucl. Inst. and Meth. A268 50-74 (1988).

[33] L. Balka et al., Nucl. Inst. and Meth. A267 272-279 (1988).

[34] S. Bertolucci et al., Nucl. Inst. and Meth. A267 301-314 (1988).

[35] S.R. Hahn et al., Nucl. Inst. and Meth. A267 351-366 (1988).

[36] G. Drake et al., Nucl. Inst. and Meth. A269 68-81 (1988).

[37] E. Barsotti et al., Nucl. Inst. and Meth. A269 82-92 (1988).

[38] D. Amidei et al., Nucl. Inst. and Meth. A269 51-62 (1988).

[39] F. Abe et al. (CDF Collaboration), Phys. Rev. Lett. 61, 1819 (1988).

[40] A.Baden, CDF Note 569, Oct. (1987).

[41] VECSUB from MARC II, VECSUB AYP Oct. (1985).

[42] S. Kuhlmann, CDF Note 521, Sept. (1987).

[43] S. Behrends et al., CDF Note 583, Dec. 1987.

[44] D.Brown and R. Carey, CDF Note 754, Jan. 1989.

[45] S. Kuhlmann, private communication.

[46] D. Brown, S. Kannappan and M.D.Shapiro, CDF Note 753, Oct. 1988.

[47] S. Kuhlmann et al., CDF Note 686, July. (1988).

[48] B. Flaugher and S. Kuhlmann, CDF Note 685, May. (1988).

[49] B. Flaugher et al., IEEE Transactions on Nuclear Science, Vol. NS-34, No.4, p. 865, Aug.(1987).

[50] J.T. Carroll et al., CDF Note 338, and Presented at the 3rd Pisa Meeting on Advanced Detectors, Italy, June (1986).

[51] M. Larwill, CDF Note 453, Mar. (1986).

[52] H. Areti et al., Proceedings of the XXIII International Conf. on High Energy Physics, Berkeley, California, July (1986).

[53] J.T. Carroll, T. Devlin and B. Flaugher, CDF Note 481, Nov. (1986).

[54] F. Kirsten et al., CDF Note 312, Apr. (1985).

[55] A.W. Booth et al., IEEE Transactions on Nuclear Science, Vol. NS-34, No.4, Aug.(1987).

[56] T. Watts, CDF Note 886 and J.T. Carroll et al, CDF Note 895 (1989).

Vita

Brenna Lynn Flaugher

[redacted]

1979-83	Physics major, Bates College, Lewiston, Maine.
1983	B.S., Bates College.
1983-89	Graduate work in Physics, Rutgers, The State University of New Jersey, New Brunswick, New Jersey.
1983-84	Teaching Assistant, Department of Physics, Rutgers, The State University of New Jersey, New Brunswick, New Jersey.
1984-89	Research Assistant, Department of Physics, Rutgers, The State University of New Jersey, New Brunswick, New Jersey.
1986	M.S. in Physics, Rutgers, The State University of New Jersey.
1987	B. Flaugher et al., Integration of the ACP Multiprocessor Farm with the CDF FASTBUS Data Acquisition System. IEEE Transactions on Nuclear Science, Vol. NS-34, No. 4, p.865, (Aug.1987).
1988	F. Abe et al. (CDF Collaboration), The CDF Detector: An Overview. Nuclear Instruments and Methods, A271, 387 (1988).
1988	J. T. Carroll et al., Level 3 System at CDF. Nuclear Instruments and Methods, A263, 199 (1988).
1989	F. Abe et al. (CDF Collaboration), Measurement of the Inclusive Jet Cross Section in $p\bar{p}$ Collisions at $\sqrt{s} = 1.8$ TeV. Phys. Rev. Lett. 62, 613 (1989).
1989	F. Abe et al. (CDF Collaboration), Dijet Angular Distributions from $p\bar{p}$ Collisions at $\sqrt{s} = 1.8$ TeV. Phys. Rev. Lett. 62, 3020 (1989).
1989	F. Abe et al. (CDF Collaboration), Measurement of the Mass and Width of the Z^o Boson at the Fermilab Collider. Phys. Rev. Lett. 63, 720 (1989).
1989	Ph.D. in Physics.